Investigations of the electronic, magnetic and crystalline structure of perovskite oxides and an oxide-oxide interface

Dissertation
der Mathematisch-Naturwissenschaftlichen Fakultät
der Eberhard Karls Universität Tübingen
zur Erlangung des Grades eines
Doktors der Naturwissenschaften
(Dr. rer. nat.)

vorgelegt von
Christoph Werner Raisch
aus Reutlingen

Tübingen
2012

Tag der mündlichen Qualifikation: 14.02.2013
Dekan: Prof. Dr. Wolfgang Rosenstiel
1. Berichterstatter: Prof. Dr. Thomas Chassé
2. Berichterstatter: Prof. Dr. Hans-Jürgen Meyer

Für Catharina und Jonas

Kurzzusammenfassung in deutscher Sprache

Die vorliegende Arbeit beschäftigt sich mit der Untersuchung der elektronischen, magnetischen und kristallinen Struktur von Perowskit-Oxiden, Strontiumtitanat $SrTiO_3$ (STO), dotierte Lanthanmanganate $La_{0.7}X_{0.3}MnO_3$ (X = Ca, Sr, Ce) und Yttriumbariumcuprat $YBa_2Cu_3O_7$. Aufgrund der elektronischen Korrelation in diesen Materialien wirken sich Einflüsse wie Verspannungen und Schichtdicke, Größe und Ladung von Dotieratomen oder der Sauerstoffgehalt von dünnen Filmen stark auf die physikalischen Eigenschaften aus. Diese Struktur-Wirkungsbeziehungen wurden mit Hilfe von röntgenbasierten Methoden wie Röntgenabsorptionsspektroskopie (x-ray absorption spectroscopy, XAS), Röntgenphotoelektronenspektroskopie (x-ray photoelectron spectroscopy, XPS) und Röntgenphotoelektronenbeugung (x-ray photoelectron diffraction, XPD) untersucht.

Die Untersuchung der Oberflächenterminierung von $SrTiO_3$ durch XPD in Kapitel 5 eröffnet die Arbeit. Es konnte durch die Kombination von Experiment und Theorie gezeigt werden, dass, in Abhängigkeit von den Präparationsbedingungen, sowohl SrO- als auch TiO_2-terminiertes STO hergestellt werden kann. Die außerordentlich gute Übereinstimmung zwischen gemessenen und simulierten Daten erlaubt die Unterscheidung mit Hilfe von XPD und lässt darauf schließen, dass chemisch geätzte Proben nicht zwangsläufig vollständig TiO_2-terminiert sind.

Die besetzte (XPS) und unbesetzte (XAS) Zustandsdichte von $La_{0.7}Ce_{0.3}MnO_3$ (LCeMO) wird in Kapitel 5 ebenso untersucht wie die magnetische Struktur und mit Transporteigenschaften verknüpft. Nur durch diesen multidisziplinären Ansatz lassen sich die physikalischen Eigenschaften mit der Art der Dotierung korrelieren. Es ergibt sich ein konsistentes Bild dieses formal elektronendotierten Materials, in dem sich die gewünschten Valenzen, $Mn^{2+/3+}$ - Ce^{4+}, und die gewünschten Eigenschaften, CMR-

Effekt und Metall-Isolator-Übergang, nicht in Einklang bringen lassen. Die formal korrekten Valenzen und eine Elektronendotierung führen zu einem rein halbleitenden Verhalten der Probe, während die erwünschten Eigenschaften nur in Proben gefunden werden die löcherdotiert sind. Der Widerspruch zwischen der Beobachtung von tetravalentem Cer und Löcherdotierung lässt sich durch Selbstdotierung erklären: Dabei sorgen Kationenvakanzen durch CeO_2-Ausscheidungen zu einer gemischten $Mn^{3+/4+}$-Valenz trotz der Detektion von Ce^{4+} (und Ce^{3+}).

Diese Kationenvakanzen werden auch in Kapitel 7 noch einmal thematisiert, in dem die XPD-Daten von undotiertem Lanthanmanganat $LaMnO_3$ (LMO) mit dotierten Manganaten $La_{0.7}X_{0.3}MnO_3$ (LXMO) verglichen werden. Es zeigen sich, neben starken Hinweisen für eine MnO_2-Terminierung aller untersuchten Proben, nur geringe Unterschiede in den Beugungsdaten von Mangan und Sauerstoff der verschiedenen Materialien. Das Grundgerüst der Manganate, eckenverknüpfte MnO_6-Oktaeder, scheint gegen chemischen Druck relativ stabil zu sein. Auf der anderen Seite werden Unterschiede in den Beugungsmustern der Dotieratome zwischen diesen Oktaedern gefunden. Man findet eine kubische Umgebung für Ca und Sr in $La_{0.7}Sr_{0.3}MnO_3$ (LCMO) und $La_{0.7}Sr_{0.3}MnO_3$ (LSMO) während Cer in LCeMO ein diffuses Beugungsbild ohne Struktur liefert. Zusammen mit den Ergebnissen aus Kapitel 5 erhärtet sich damit der Verdacht, dass sich das Dotieratom Ce nicht ausschließlich zwischen den Oktaedern befindet sondern Kationenvakanzen durch Phasenseparation bildet.

Das achte Kapitel präsentiert Ergebnisse von Doppellagen bestehend aus dem Ferromagneten LCMO und dem Hochtemperatursupraleiter $YBa_2Cu_3O_7$ (YBCO) in direktem Kontakt. Erneut wird die elektronische und magnetische Struktur durch die Kombination von Transporteigenschaften und spektroskopischen Ergebnissen studiert. Während die magnetischen Eigenschaften dieser Grenzfläche zwischen den beiden widerstreitenden Phänomenen, Ferromagnetismus und Cooper-Paar-Bildung, im Einklang mit anderen Veröffentlichungen ist, ergeben sich Diskrepanzen bei der orbitalen Besetzung zu früheren Ergebnissen. Eine alternative Erklärung wird in Form einer Entkopplung zwischen Magnetismus und Supraleitung durch eine isolierende Schicht nahe der Grenzfläche gegeben. Die bisher diskutierten Mechanismen konnten nicht reproduziert werden, da die atomare Struktur der Grenzflächen nicht direkt vergleichbar ist. Es zeigt sich, dass auch hier der Einfluss der kristallinen Struktur in Zukunft genauer untersucht werden muss.

Zusammenfassend lässt sich sagen, dass durch multidisziplinäre Ansätze in jedem experimentellen Kapitel der vorliegenden Arbeit interessante Erkenntnisse über die Struktur-Wirkungsbeziehungen von elektronischer, magnetischer und kristalliner Struktur in den Perowskit-Oxiden erzielt werden konnten. Es zeigt sich, dass die komplexe Natur der hier untersuchten Materialien sowohl viele interessante Fragen aufwirft als auch spannende Möglichkeiten bietet. Der Weg zu ihrem Verständnis ist geebnet, der Weg bis zur Kontrolle der korrelierten Elektronen ist noch weit. Die Ergebnisse dieser Arbeit stellen einen Mosaikstein auf diesem Weg dar.

We used to think if we knew one, we knew two, because one and one are two. We are finding that we must learn a great deal more about ‘and’.

Sir Arthur Eddington

1 INTRODUCTION

The mineral perovskite ($CaTiO_3$) was discovered and named by Gustav Rose, a German mineralogist, in 1839 from samples found in Achmatowsk in the Ural Mountains. It is named after a Russian nobleman, politician and mineralogist, Count Lev Aleksevich von Perovski. It also lends its name to the class of compounds with composition ABX_3, which have the same type of crystal structure known as the perovskite structure. Here, A and B are cations while X is typically a halogen or oxygen anion. The bigger cation A and the X anions form a cubic close packing AX_3 with the smaller B cation occupying one quarter of the octahedral sites. The wide variety of suitable elements for A, B and X lead to an almost infinite amount of compounds with highly interesting properties.

The underlying work deals with three classes of perovskite oxides, the “titanates”, the “cuprates” and the “manganites”, where the B cations are Ti, Cu and Mn respectively, each class with very characteristic properties.

Strontium titanate, $SrTiO_3$ (STO), like so many oxides is an insulator, yet paraelectric and diamagnetic. It gained special interest as a commercially available, high quality substrate for the growth of high-temperature superconductors and other oxide thin films. The huge class of perovskite cuprates is most famous for members like $YBa_2Cu_3O_7$ (YBCO), the well-known high-temperature superconductor. It was the first material with a superconducting transition temperature T_C above 77 K, the boiling point of liquid nitrogen.

Finally, the doped, mixed-valent perovskite manganites $La_{0.7}X_{0.3}MnO_3$ (here X = Sr, Ca, Ce) have to be mentioned. They appeared on the screen of experimental and theoretical physicists in the 1950s when ferromagnetism and magnetoresistance were discovered in these compounds, leading to the theory of double exchange. In the mid-1990s they further increased their importance, following the description of the Jahn-Teller polaron and the discovery of the colossal magnetoresistance phenomenom.

They may be derived from an insulator, $LaMnO_3$, but the doping allows the control of electric and magnetic properties over a wide range, i.e. from insulating behavior to metallic conductivity or from diamagnet to ferromagnet. Further notable effects are found when electric or magnetic fields are applied, including spin polarization and the related effect of colossal magnetoresistance.

These substances may be approximated as consisting of manganese atoms and their surrounding oxygen octahedra while the rather passive lanthanum (or strontium in STO) mainly donates it´s three electrons to MnO_6 (or TiO_6). These corner-shared units are not only the building blocks of a tightly bound 3D network; they are also responsible for the transport and magnetic properties. It is thus easy to see, how perturbations like doping, strain, cation size mismatch, anion vacancies or the Jahn-Teller effect can affect the properties of these samples.

Another way to look at the perovskites is to think of a stack of alternating layers. Both concepts are used in this work, whenever they fit. In $SrTiO_3$ for example, charge neutral $(\mathrm{Sr}^{2+}\mathrm{O}^{2-})$ and $(\mathrm{Ti}^{4+}\mathrm{O}_2^{2-})$ layers follow upon each other when viewed along the [001] direction. In this picture $LaMnO_3$ consists of an array of charged $(\mathrm{La}^{3+}\mathrm{O}^{2-})^+$ and $(\mathrm{Mn}^{3+}\mathrm{O}_2^{2-})^-$ layers. When these two materials meet at an interface (even with vacuum), a polar discontinuity is created which must lead to some form of structural or electronic reconstruction. For an interface between for instance $LaAlO_3$ and $SrTiO_3$ it is important to know which layers meet there, since the SrO-AlO_2 interface is insulating while the TiO_2-LaO interface is conducting.

The first set of experiments (chapter 5) described in the underlying work deals with the termination of STO and the changes found on the surface for different preparation conditions. The knowledge and control of the exact termination of the substrate is of importance for the overlayers. Atomic control of the arrangement at the surface is the key for obtaining high-quality overlayers with the desired properties.

The second and third part of the experiments was performed on doped manganites, overlayers on STO. The electronic, magnetic and crystal structure is in detail examined for the Cerium doped lanthanum manganite $La_{0.7}Ce_{0.3}MnO_3$ (LCeMO) in chapter 6. With this knowledge in mind, the electronic and crystalline structures of Strontium doped $La_{0.7}Sr_{0.3}MnO_3$ (LSMO), Calcium doped $La_{0.7}Ca_{0.3}MnO_3$ (LCMO) and undoped $LaMnO_3$ (LMO) are discussed in chapter 7. The focus lies on a multi-technique approach to correlate changes of one parameter to its effects on others. The characterization of a YBCO / LCMO heterostructure on STO concludes this work (chapter 8). Again it is the electronic, magnetic and crystalline structure at the interface that proves crucial for the properties of this unusual system which artificially combines a superconductor (SC) and a ferromagnet (FM). This structure makes two antagonistic effects meet, the tendency of a superconductor to pair two electrons with different spin into Cooper pairs and the tendency of a ferromagnet to align all spin moments. This fascinating competition shows the wide range of properties that the perovskite oxides offer when they are used accordingly and combined usefully. The above mentioned polar discontinuity at the interface between a manganite and a cuprate is examined. The thesis is completed by a summary and an outlook.

In an article titled “Interplay between spin, charge and orbital degrees of freedom in magnetic oxides”, the authors Daniel Khomskii and George Sawatzky presented why the connection between (magnetic) ordering and transport is among the “most difficult but also most challenging and very actively studied problems nowadays”. This is eloquently expressed by the introductory quote by Sir Arthur Eddington (1882 - 1944), a British astrophysicist who was among the first to prove Einstein´s theory of general relativity. We may have understood that complex or composite systems do not behave simply as linear combinations of the properties of the parent materials but we have only just begun to tap into the almost infinite possibilities that this insight offers. It is the aim of this thesis to add a little mosaic to the large task of understanding and controlling the behavior of the perovskite oxides and their interfaces.

2 TABLE OF CONTENTS

Parts of this thesis have been published in these articles:

Chapter 5 – STO:

C.Raisch, A. Chassé, Ch. Langheinrich, T. Chassé, Preparation and investigation of the A-site and B-site terminated $SrTiO_3(001)$ surface: A combined experimental and theoretical x-ray photoelectron diffraction study, *J. Appl. Phys.* **112** (2012) 073505.

Chapter 6 – LCeMO:

R. Werner, C. Raisch, C. Leca, V. Ion, S. Bals, G. van Tendeloo, T. Chassé, R. Kleiner, D. Koelle - Transport, magnetic, and structural properties of $La_{0.7}Ce_{0.3}MnO_3$ thin films: Evidence for hole-doping, *Phys. Rev. B* **79** (2009) 054416.

Chapter 7 – LXMO:

C. Raisch, Ch. Langheinrich, R. Werner, R. Kleiner, D. Koelle, M. Glaser, T. Chassé, A. Chassé, – X-ray Photoelectron Diffraction Study of Dopand Effects in $La_{0.7}X_{0.3}MnO_3$ (X = La, Sr, Ca, Ce) thin films, *J. Appl. Phys.* **113** (2013) 063511.

Chapter 8 – YBCO / LCMO:

R. Werner, C. Raisch, A. Ruosi, B.A. Davidson, P. Nagel, M. Merz, S. Schuppler, M. Glaser, J. Fujii, T. Chassé, R. Kleiner, D. Koelle, YBa2Cu3O7 / La0.7Ca0.3MnO3 bilayers: Interface coupling and electric transport properties, *Phys. Rev. B* **82** (2010) 224509.

Further publications in peer-reviewed journals:

A. Ruosi, C. Raisch, A. Verna, R. Werner, J. Fujii, R. Kleiner, D. Koelle, T. Chassé, B.A. Davidson, Electron sampling depth and saturation effects in perovskite films investigated by soft x-ray absorption spectroscopy, in preparation.

M.B. Casu, S.-A. Savu, B.-E. Schuster, I. Biswas, C. Raisch, H. Marchetto, Th. Schmidt, T. Chassé – Island shape and segregation steered by the geometry of the substrate lattice, *ChemComm* **48** (2012) 6957.

I. Dreiling, C. Raisch, J. Glaser, T. Chassé, D. Stiens - Temperature dependent tribooxidation of Ti-B-N coatings studied by Raman spectroscopy, *WEAR* **288** (2012) 62.

J. Tomaschko, C. Raisch, V. Leca, T. Chassé, R. Kleiner, D. Koelle - Electric transport across $Sr_{1-x}La_xCuO_2$/Au/Nb planar tunnel junctions and x-ray photoelectron and Auger-electron spectroscopy on $Sr_{1-x}La_xCuO_2$ thin films, *Phys. Rev. B* **84** (2011) 064521.

I. Dreiling, C. Raisch, J. Glaser, D. Stiens, T. Chassé - Characterization and oxidation behavior of MTCVD Ti-B-N coatings, Surf. Coat. Technol. **206** (2011) 479-486.

M.B. Casu, B.-E. Schuster, I. Biswas, C. Raisch, H. Marchetto, Th. Schmidt, T. Chassé - Locally resolved core-hole screening, molecular orientation, and morphology in thin films of diindenoperylene deposited on Au(111) single crystals, Adv. Mater. **22** (2010) 3740–3744.

H. Zhang, V. Presser, C. Berthold, K. G. Nickel, X. Wang, C. Raisch, T. Chassé, L. He, Y. Zhou - Mechanisms and Kinetics of the Hydrothermal Oxidation of Bulk Titanium Silicon Carbide, J. Am. Ceram. Soc. **93** (2010) 1148.

11 <TABLE OF CONTENTS

V. Presser, O. Krummhauer, K.G. Nickel, A. Kailer, C. Berthold, C. Raisch - Tribological and hydrothermal behaviour of silicon carbide under water lubrication, WEAR **266** (2009) 771.

M.M. Blideran, M. Häffner, B.-E. Schuster, C. Raisch, H. Weigand, M. Fleischer, H. Peisert, T. Chassé, D.P. Kern - Improving etch selectivity and stability of novolak based negative resists by fluorine plasma treatment, Microelectronic Engineering **86** (2008) 769.

3 THEORETICAL BACKGROUND OF METHODS AND MATERIALS

This chapter deals with the theoretical requirements of the techniques used in the work, namely the x-ray based methods XPS, XPD, XAS and XMCD. X-ray Photoelectron Spectroscopy (XPS) [**1**] and Diffraction (XPD) [**2**] are usually performed at a home laboratory spectrometer equipped with a commercial x-ray anode, while X-ray Absorption Spectroscopy (XAS) [**3**] and X-ray Magnetic Circular Dichroism (XMCD) [**4**] require a tunable x-ray light source in the form of a synchrotron facility.

The electronic, magnetic and crystalline structure of three classes of perovskite oxides (titanates, cuprates and manganites) is also introduced in this section. It is shown that they are intimately linked in these substances, yielding a very rich phase diagram for the manganites.

It further describes the theory of thin film growth by means of pulsed laser deposition (PLD) and the influences of various preparation parameters on the properties of the samples. Special focus is paid to the effects of film thickness and oxygen content on the electronic structure of the films.

3.1 Methods: XPS

The history of X-ray Photoelectron Spectroscopy (XPS) includes the discovery of the photoelectric effect by Hertz and Hallwachs [**5**], [**6**], its correct description by Einstein [**7**] and the development of high-resolution electron energy analyzers by Siegbahn [**8**]. Soft x-rays have typical energies of a few hundred eV with resulting wavelengths on the order of a few nanometers and are thus ideally suited for the study of (crystalline) solids.

The outer photoelectric effect describes the emission of photoelectrons from a sample following its irradiation with (monoenergetic soft x-ray) light. The emitted electrons have kinetic energies E_{kin} that are determined by the energy of the incident light $h\nu$ and the forces E_b that bind electrons to atomic nuclei. Einsteins nobel prize winning formula states that

$$E_{kin} = h\nu - E_b \ (- \Phi)$$

The energy of the incident radiation in the case of XPS is typically 1253.6 eV or 1486.6 eV, which are the Mg K_α and Al K_α lines of commercial home laboratory x-ray tubes. The binding energies correspond to the ionization energies of the different orbitals of an atom with respect to the Fermi level E_F. The resulting kinetic energies of the photoelectrons limit their inelastic mean free paths in a solid to a few Å, making XPS a very surface sensitive analysis method. The term Φ in brackets is the work function, an additional barrier that the photoelectron has to overcome as well in order to leave the sample, i.e. the difference between E_F and the vacuum level E_{vac}. It is comprised of the energy (chemical potential) needed to remove a negatively charged electron from the bulk of the sample and the energy needed to cross the surface dipole. It thus determines the minimal energy of the incoming light required to initiate emission.

Only after the development of high resolution electron energy analyzers by Siegbahn was it possible to study the emitted electrons in more detail. Sorting the electrons by their kinetic energy and plotting their number as a function of this energy, one obtains spectra showing unique peaks for each element. In mixed samples, the peaks (and their backgrounds) simply add up. This readily yields the chemical composition of a sample. The intensity, exact peak position and shape of a given peak allow obtaining further information on the electronic structure (bonds to other atoms or oxidation state).

A typical overview spectrum is found in figure 6-1, showing (from right to left) valence band related structures near zero binding energy, followed by emission lines from the core levels of all constituting elements of $La_{0.7}Ce_{0.3}MnO_3$ as well as the O KVV Auger line at approximately 770 eV on an ever increasing background.

The intensity of an XPS peak is proportional to the number of emitters (for given values of the illuminated area, the photon flux, the apparative function, the inelastic mean free path and sensitivity factors). The shape of an XPS peak is further determined by the spin-orbit splitting which arises from the fact that there are two possible ways to combine orbital (l) and spin (s) magnetic moments. For $l \geq 1$ and $s = \pm½$ there are two possible values of $j = l + s$ with different energies (less than 0.5 eV apart for light elements, more than 100 eV apart for heavy elements). The spin-orbit splitting is exemplified in the top half of figure 6-2, showing the Mn $2p_{3/2}$ and the Mn $2p_{1/2}$ lines at 642 eV and 654 eV, respectively. They have an intensity ratio of roughly 2j+1, which for 2p electrons amounts to 2:1.

The exact peak position is a measure of the so called chemical shift, the Madelung potential and a relaxation term. In chemical bonds, despite the fact that only valence band electrons are involved, the core level energies are different from the elemental values. This is due to the fact that positive partial Pauling charges make it harder for an electron to escape the solid because of the additional attractive force from the positive charge. Siegbahn found an almost linear correlation between binding energy and partial Pauling charge (closely related to the difference in electronegativity between the emitter and its neighbors). Apart from this electronic reconstruction, other effects like surface reconstructions or doping change the binding energy as well.

The analysis of the chemical shift gives valuable information about the bonds to nearest neighbors and the oxidation state of an emitter. The Madelung term takes into account the effects of non-nearest neighbors and is relevant mainly for the description of binding energies in ionic crystals.

Contrary to the chemical shift, which is a combined initial and final state effect, the relaxation term depends on the final state only, including effects like screening of the core hole by a metal surface or the polarization of the environment. This part of the peak shift is thus sensitive to the surrounding of an emitter.

A core hole represents a non-equilibrium state, which can decay in several ways, including such secondary processes as shake-up, shake-off (energy transfer from photoelectron to valence electron) and plasmon resonances (energy transfer to the electron gas) as well as the emission of x-rays and Auger electrons. These well-defined energy losses may be used for the interpretation of the electronic structure as well. Of these, the Auger process is most likely and will be discussed in more detail.

When a valence electron fills the inner orbital vacancy created by the x-ray, its excess energy can be transferred to another electron. If this electron has enough kinetic energy to overcome the work function it will be emitted from the sample as well, leading to additional peaks in the photoemission spectrum. The kinetic energy of an Auger electron is the difference between the initially formed ion and the doubly charged final state, which often makes the Auger lines more sensitive to chemical shifts. The O KVV Auger electron in is the result of primary photoemission from the K shell (O1s) and a final double vacancy in the valence band V. For more information the reader is referred to [**1**].

3.2 Methods: XPD

The primary photoelectron created in the x-ray absorption process may be treated as a spherical wave, travelling through the solid. On its way into the vacuum, this wave experiences scattering at the potentials of atoms in its path. This typically leads to enhanced intensities along internuclear axes, which can be detected as a diffraction pattern modulating the photoelectron intensity above the sample. This X-ray Photoelectron Diffraction (XPD) technique has been successfully employed for the study of the relaxation / reconstruction of single crystals, adsorbed atoms or molecules, epitaxial growth, Fermi surface mapping, surface magnetism and photoelectron holography [**9**], [**10**], [**11**], [**12**]. In this work it is used for the investigation of the surface termination of $SrTiO_3$ in dependence of preparation and to examine doped lanthanum manganites in dependence of the dopant atom. The high surface sensitivity of photoelectrons makes this technique a highly valuable tool for a surface scientist. More bulk sensitive experiments like XRD are not suited to determine the surface structure of solids. One other highlight of XPD is the chemical sensitivity of the probe. By selecting a photoemission line and recording the intensity modulation above the sample, one can obtain information about the structure around individual elements of a sample.

A photon creates a photoelectron inside a solid which may be emitted directly and without scattering as the so called primary wave. Alternatively the electron wave can suffer scattering processes at neighboring atomic nuclei and still leave the sample. If this scattered wave and the primary wave interfere with each other due to the different path lengths travelled, the intensity of photoelectrons is modulated.

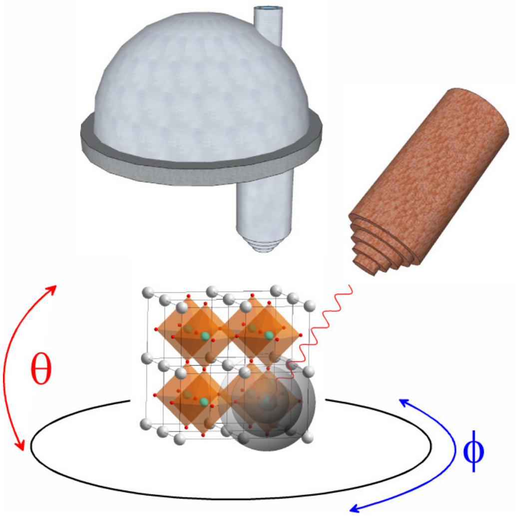

Figure 3-1: Scheme of a XPD setup where a crystalline sample is irradiated by an x-ray source from the right hand side. The outgoing electrons scatter at the environment of the emitter and create a site- and element-specific diffraction pattern that is recorded by the electron energy analyzer (top) in dependence of the azimuthal ϕ and polar angle θ.

A typical XPD setup is shown in figure 3-1 showing the x-ray source on the right, the rotatable sample and the electron energy analyzer. Because the experiment is performed in an UHV chamber, the positions of the analyzer and the x-ray source are fixed (unlike in XRD). The sample is rotated along ϕ and / or tilted along θ with respect to the analyzer to detect azimuthal or polar scan angular distribution curves. If the intensity is recorded in the entire half sphere above the sample, the result is called a 2π-plot (pizza plot) and is shown in figure 3-2.

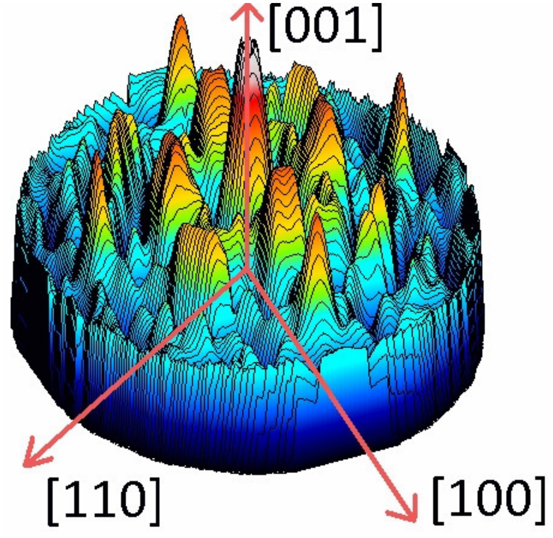

Figure 3-2: Full hemispherical scan of the photoelectron intensity of the Ag3d core level of a Ag(001) single crystal showing the fourfold symmetry of the cubic lattice. The extraction of intensities for instance along the [100] azimuth yields a polar scan. The extraction of intensities for a fixed polar angle gives an azimuthal scan.

From such a plot, all possible azimuthal angle scans and all possible polar angle scans can be extracted. This is thus the appropriate scan if the sample structure is unknown. Since the detection time is in the range of 15 to 25 hours, this experiment is very demanding for the x-ray source and the electron energy analyzer.

If the crystal structure is known, it is more convenient to measure azimuthal and polar scans directly. Detecting the interference pattern along the face diagonal for instance, readily yields the [100] polar scan. Recording the diffraction pattern along the space diagonal gives the [110] polar scan as shown in figure 3-3.

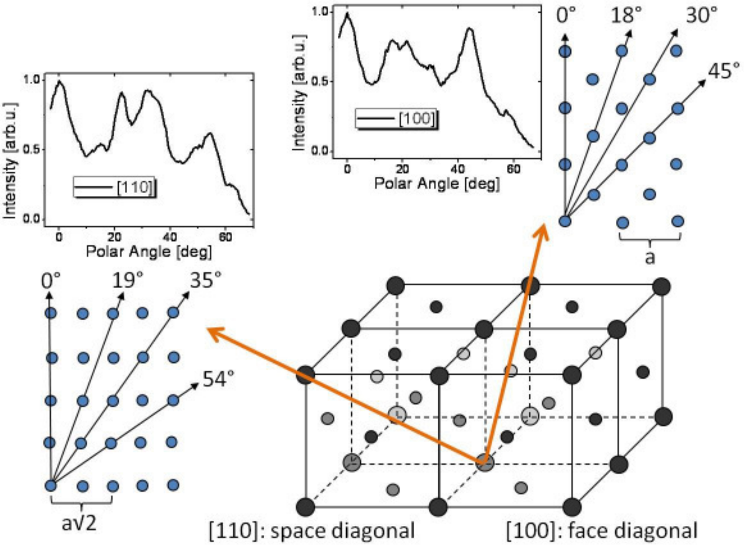

Figure 3-3: Example of polar scans in a face centered cubic crystal system. Measuring the photoemission intensity in dependence of the tilt angle along the face diagonal ([100] direction) or the space diagonal ([110] direction) gives a unique set of expected scattering angles and characteristic polar scans.

There is typically higher intensity in directions where many scatterers are present if one uses photoelectrons with kinetic energies above 500 eV. This regime is determined by strong forward scattering (c.f. chapter 5.3), while lower electron kinetic energies lead to a more isotropic scattering amplitude with significant backscattering. The measured intensities must be compared to simulations that include multiple scattering effects. This is described in more detail in chapter 3.5.

3.3 Methods: XAS and NEXAFS

If, instead of analyzing the kinetic energy or the travelling direction of a photoelectron, one chooses to study the absorption process of x-rays in matter in more detail, a tunable light source is needed. For x-rays this is a nontrivial task which requires synchrotron radiation, the radiation emitted by accelerated charged particles in an electron storage ring. Like in all other kinds of spectroscopy there exists the possibility to deduce information about the structure of a sample from the study of the absorption cross section µ for soft x-rays. The technique of x-ray absorption spectroscopy (XAS) is based on the fact that this radiation can induce transitions of core level electrons into higher states.

If the energy of the incident light is tuned to an absorption edge, the sample strongly absorbs x-rays and electrons are transferred from core levels into unoccupied states above the Fermi edge. In the dipole approximation (single electron transfer, electron spin neglected), the following selection rules are valid for the x-ray absorption process: $\Delta l = \pm 1$, $\Delta m = 0, \pm 1$, where l and m are the orbital and magnetic quantum numbers, respectively. This makes it possible to study element compositions and oxidation states, making this a complementary technique to XPS. However, it is again the fine structure of the measured absorption edges that contains most information. This so called near-edge x-ray absorption fine structure (NEXAFS) is due to the large variety of possible final states for the photoelectron between the Fermi level and the continuum region at the vacuum level. The orbital occupation in this range is crucial for the chemistry and the physics of matter, explaining the huge success of NEXAFS spectroscopy in the field of surface science.

In comparison to classical Lambert-Beer-type rotational, vibrational or UV/Vis spectroscopies, in the soft x-ray regime the photon penetration depth is limited to nm or few µm. This makes it difficult to work in a transmission geometry and requires alternative ways of correlating secondary processes to the absorption cross section. The starting point is the absorption of a soft x-ray photon and the resulting creation of a photoelectron. The subsequent filling of the core hole by a shallow core electron or a valence electron creates energy which is partially emitted in the form of x-rays. If this radiation leaves the sample we speak of fluorescence decay. Detecting this radiation gives bulk-sensitive information about the sample because the information depth of x-ray photons is large, several 10 to 100 nm. The measured signal is called Fluorescence Yield (FY).

This process, however, competes with another decay channel, the excitation of above-mentioned Auger electrons [**13**]. This of course leads to new core holes, which decay as well. The ensuing cascade ends in a large number of (primary) photoelelectrons and Auger electrons and (low kinetic energy) secondary electrons which partially leave the sample. This electron drain may be measured by a picoamperemeter and gives the total electron yield (TEY) signal commonly used in x-ray absorption spectroscopy as a measure of the amount of excited electrons. Proportionality between the photoabsorption cross section μ and the intensity of this current must be ensured in order to be able to make assumptions about the unoccupied band structure, the valence state or the ground state symmetry of the element under investigation. The TEY signal in comparison to the FY signal is a lot more surface-sensitive because the information depth in this case depends on the electron inelastic mean free path which is in the range of few nm only. At most synchrotron beamlines both signals can be detected simultaneously, giving valuable information about the surface and bulk electronic structure and the differences between them. A more detailed review about the (N)EXAFS process is found in [**3**].

3.4 Methods: XLD and XMCD

As briefly mentioned in the previous chapter, the chemical and the physical properties of a sample are mainly determined by its valence electrons. Not only are they responsible for attributes like color or resistivity, they are also responsible for such phenomena as reactivity or magnetism.

The following techniques, x-ray linear dichroism (XLD) and x-ray magnetic circular dichroism (XMCD) will be explained using manganese, and especially Mn^{3+}, as an example. Here the valence electrons are the 3d electrons occupying the d-orbitals. For this d^4 system, there are several ways to occupy the ten available spots in the five d-orbitals. The energetically degenerate levels (O_3) are split by a crystal field of cubic symmetry (O_h) into three t_{2g} orbitals and two e_g orbitals. These triply degenerate t_{2g} states (d_{xy}, d_{xz}, d_{yz}) and the doubly degenerate e_g states ($d_{3z^2-r^2}$, $d_{x^2-y^2}$) may be split further by other perturbations like Jahn-Teller distortion, an external magnetic field or lattice strain. Figure 3-4 shows the splitting of the degenerate d-orbitals by two common crystal fields, cubic O_h symmetry and tetragonal D_{4h} symmetry found in elongated octahedra. The so-called high spin configuration of Mn^{3+} features one electron per orbital which gives a net spin of ${}^{4}/_{2}$ with all spins being aligned. In the low spin case two orbitals are doubly occupied and the resulting net spin is 0, because paired spins have opposite sign and cancel each other.

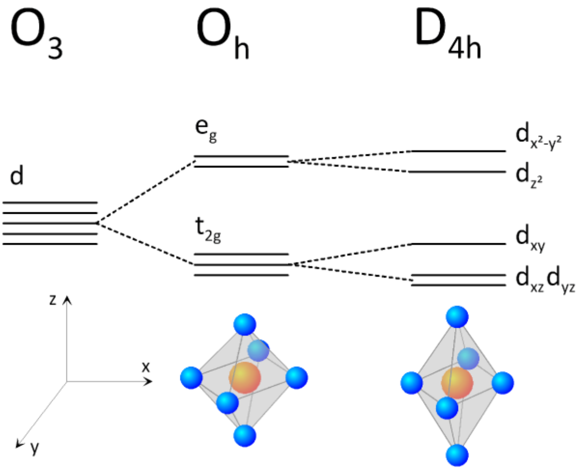

Figure 3-4: The influence of the crystal field on the five 3d orbitals. In a cubic environment (middle), as found in the perovskites, the degeneracy of these levels is lifted and two subsets t_{2g} and e_g are created. Elongation (along z), as found in Jahn-Teller-distorted systems, further splits these subsets (right).

If we look at the t_{2g} orbitals as forming a valence band then the e_g orbitals are like the conduction band in classical semiconductor theory. Only for the high-spin case there is an electron in one of the e_g orbitals available for transport and interaction with other electrons, i.e. magnetism. Some properties associated with this concept will be discussed later. Knowledge of the orbital occupation is however key to all of them.

To investigate this particular detail, several XAS related methods have been established. By using linearly or circularly polarized light it is possibly to select or to suppress some transitions, making it possible to deduce the geometry of the empty states. As seen in the indices in figure 3-4, all d states have different geometries, depending on their orientation with respect to the crystal field. The t_{2g} states have no electron density along the crystal axes (node lines) while the e_g states have localized electron density along the z direction ($d_{3z^2-r^2}$) or along the x and y directions ($d_{x^2-y^2}$). Looking at the dipole selection rules, it is possible to determine the angular resolved unoccupied electronic structure of crystalline samples by changing the direction of the incident linearly polarized light.

In the dipole approximation, transitions into in-plane or out of plane orbitals are only allowed if the electric field vector points in this direction. Figure 3-5 shows the experimental setup used for x-ray linear dichroism measurements. To probe the transition into unoccupied $d_{3z^2-r^2}$ states, the sample must be irradiated with light which is linearly polarized in a way that the electric field vector is parallel to the sample normal. For a bending magnet setup this is achieved by tilting the sample to grazing incidence, for an undulator setup one has to change gap and phase values between the two halves of the undulator. The right part of figure 3-5 shows the case of normal incidence with the electric field vector perpendicular to the sample normal which selects transitions into in-plane $3d_{x^2-y^2}$ orbitals. The difference in x-ray absorption intensity between these two extremes is called the x-ray linear dichroism XLD.

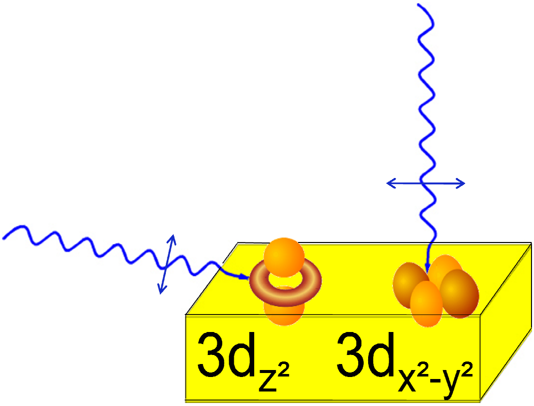

Figure 3-5: Schematic XLD setup with incident light in a grazing incidence (left) and a normal incidence (right) geometry. The two 3d e_g orbitals with electron density pointing out-of-plane ($d_{3z^2-r^2}$, left) and in-plane ($d_{x^2-y^2}$, right) are also shown.

For magnetic samples in a magnetic field another way of lifting the degeneracy is possible. The applied field along +z favors a parallel alignment of magnetic moments, yet the density of states (DOS) with parallel spins has higher energy (minority carriers). The electron spin magnetic moment is antiparallel to the electron spin angular momentum. This yields different numbers of unoccupied states for the spin-up and spin-down configuration, i.e. more spin up holes are available. In order to probe the spin-dependent unoccupied density of states, however, another prerequisite is necessary. Using left or right circularly polarized light, it is possible to transfer angular momentum from the photon to the photoelectron, changing its spin via spin-orbit coupling. Since the number of spin up holes is bigger than the number of spin down holes, there is different intensity for x-ray absorption performed with light of two different helicities for ferromagnetic samples in an applied magnetic field. The difference between the two spectra is called x-ray magnetic circular dichroism XMCD and it is described in figure 3-6.

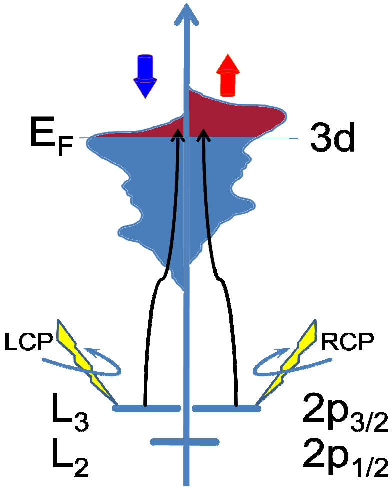

Figure 3-6 (after [4]): Split density of states (DOS) for a magnetic material in an applied field along +z and transitions from a L shell core level (Mn2p) to valence band states (Mn3d) above the Fermi level E_F. In this configuration, left-circularly polarized light excites "spin down" electrons (left) and right circularly polarized light excites "spin up" electrons into the respective unoccupied DOS.

Left- (right-) circularly polarized light (LCP/RCP) excites 2p electrons into empty 3d states, which are spin-polarized in ferromagnets. This yields a different density of states for spin up / down electrons. The resulting deviations of absorption intensity for the two light helicities (or magnetization directions) thus probes the magnetic structure of individual elements. The excellent article [**4**] and references therein are recommended for further reading.

3.5 Methods: EDAC

To simulate multiple scattering effects, we use the cluster model approach of the electron diffraction in atomic clusters EDAC code [**14**] based on the muffin-tin potential approximation. The atomic positions in the cluster are bulk-like, i.e. alternating slabs of SrO and TiO_2 form cubic unit cells with lattice parameters a = b = c = 3.905 Å. The solid is described by centrosymmetric potentials located at the atom sites. Between these point scatterers the potential takes the value of the muffin-tin constant. The program calculates radial matrix elements and scattering phase shifts that represent the atomic properties. The electron wave function is expressed in terms of multipole curved (outgoing) waves that are scattered at one or more atoms of the cluster. The coefficients of this expansion are refined iteratively using the recursion method by Haydock [**15**]. After including all scattering processes, the photoelectron intensity above the cluster is displayed as a function of polar and azimuthal angles and can be compared to measured intensities. Further information on multiple scattering cluster calculations are found in chapter 3.6.

The maximum angular momentum for which the scattering phase shift takes non-zero values is approximated as $l_{max} \approx k\ r_{MT}$. Here, the muffin-tin radius r_{MT} is approximated by the ionic radius and k is the wave vector of the electron. It must be noted that the computation time of EDAC scales with $N^2(l_{max}+1)^3$, so the two parameters, cluster size N and l_{max}, should be chosen carefully to minimize the duration of multiple scattering cluster calculations.

3.6 Methods: Halle PED MSC code

The Photoelectron Diffraction (PED) multiple scattering cluster (MSC) code used at the University of Halle-Wittenberg is described in detail in [**16**]. A brief summary is given here:

The multiple scattering process starts with a core electron with quantum numbers $(l_c, m_c) = L_C$ localized at R_0 and an incoming photon of energy hν and polarization vector

u. The final state may be separated into the absorption and the scattering process. The final state after absorption is characterized by the transition matrix element M (dipole approximation), the final state after scattering depends on the scattering path operator B.

The photoelectron intensity in the direction K is then given as the product of this scattering path operator B and the transition matrix element M integrated over the solid angle Ω and the energy E:

$$I_{l_c}(K,E,u) \propto \int_{\Delta\Omega} d\Omega \int_{\Delta E} dE \sum_{R_0} \sum_{m_c} \left| \sum_{L} B_L(K,R_0,E) \times M_{LL_c}(E,u) \right|^2 \delta(E - h\nu - E_c)$$

The scattering of the direct wave at surrounding scattering centres in the muffin-tin potential creates an outgoing wave that may be scattered at further atoms and so on. The scattering path operator contains information about the path that the electron travels and can be described as:

$$\begin{aligned} B_L^{R_0}(k) = {} & e^{-ikR_0}(-i)^l Y_L(\hat{k}) + \sum_{R_1 \neq R_0} e^{-ikR_1} \sum_{L'} (-i)^{l'} Y_{L'}(\hat{k})\, t_{l'}^{R_1} G_{L'L}(R_{10}) \\ & + \sum_{R_2 \neq R_1 \neq R_0} e^{-ikR_2} \sum_{L''L'} (-i)^{l''} Y_{L''}(\hat{k})\, t_{l''}^{R_2} G_{L''L'}(R_{21}) \\ & \times t_{l'}^{R_1} G_{L'L}(R_{10}) + \cdots \end{aligned}$$

The first term is the direct wave, written in spherical harmonics (“orbitals”) Y_L. The second term describes single scattering at an atom localized at R_1 with a phase shift t after the electron wavefunction G has travelled from R_0 to R_1. The third term describes multiple scattering at an additional atom R_2 and so on.

3.7 Methods: Pulsed Laser Deposition

The growth process in the pulsed laser deposition (PLD) [**17**] process is a non-equilibrium process. It works by ablating a stoichiometric target (ground, mixed and sintered powders of, for instance, La_2O_3 and Mn_2O_3 for $LaMnO_3$) by a KrF excimer laser ($\lambda = 248$ nm). The high local power density of up to 6 J/cm^2 evaporates even high melting point oxides and generates a plasma plume above the target. The high energy also allows the evaporation of complex materials because the different evaporation rates (of lanthanum and manganese oxide in this case) become negligible. The heated substrate is placed directly in this plume and the film is deposited. Partial pressures of oxygen or other reactive or inert gases can be varied in a wide range of compositions.

Despite the high initial energy, collisions of particles inside the plume lower their energy so strongly that the substrate has to be heated to ensure enough surface mobility for optimal, typically layer-by-layer, growth. The high degree of supersaturation at the growth front leads to a high density of nuclei with small sizes, typically one unit cell.

3.8 Materials: Perovskites

All elements form oxides, binary oxides like MnO, ternary oxides like $SrTiO_3$, quarternary oxides like $YBa_2Cu_3O_7$ and many more. Most metal oxides consist of M-O-M units, often the oxygen anions form polyhedra like MO_6 around the metal cations. The materials investigated in this thesis all belong to the large subgroup of the perovskite oxides ABO_3, where A and B are a large and a small metal cation, respectively. They differ mainly in the central B atom and will be presented this way in the following section. Titanates and Cuprates are only briefly introduced and the main focus lies on the manganites. The structures of a prototypical perovskite, $SrTiO_3$, and the high-temperature superconductor $YBa_2Cu_3O_7$ are presented and compared in figure 3-7. For further information, the reader is referred to chapter 3.9.5 and inorganic textbooks [**18**].

The upper left corner shows a schematic perovskite unit cell, consisting of a central BO_6 octahedron and grey A site atoms on the corners of a cube. Below is a more realistic picture of the perovskite structure with a cubic close packing of similar sized A and O atoms (A = Sr). The octahedral interstice in the center of the cube is occupied by the smaller B-site ion (B = Ti). The ionic radii in the legend are drawn to scale. The right hand side of figure 3-7 shows the YBCO unit cell. The corrugated superconducting copper oxide planes are separated by a Y ion.

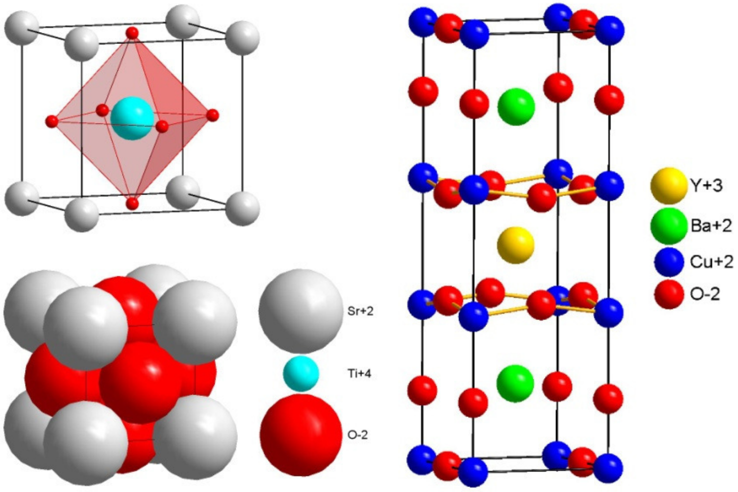

Figure 3-7: Schematic (top left) and realistic (bottom left) representation of a typical perovskite $SrTiO_3$. The $YBa_2Cu_3O_7$ unit cell is displayed on the right with the superconducting copper oxide planes highlighted.

3.8.1 Titanates

Strontium titanate, $SrTiO_3$, has a (room temperature) cubic unit cell with a lattice constant of 3.905 Å. The central units here are TiO_6 octahedra which are linked to each other via shared oxygen atoms. The perfect crystal is an insulator, owing to the (formal) d^0 configuration of the titanium ion but lattice defects like oxygen vacancies transform the material into a wide gap semiconductor. More information on STO and its surface preparation are given in chapter 4.3.1.

3.8.2 Cuprates

The crystal structure of the high-temperature superconductor $YBa_2Cu_3O_{7-\delta}$ may also be derived from the mineral perovskite by stacking three oxygen-deficient unit cells with different compositions on top of each other. Then, one $YCuO_2$ cell is sandwiched between two $BaCuO_{2.5}$ cells. Oxygen atoms are missing in the central Y layer and in the top and bottom layers in figure 3-7. For reason of charge neutrality, the two inequivalent copper sites, copper chains and copper planes, have formal valences of Cu^{3+} and Cu^{2+}. Divalent copper is a $3d^9$ system and should thus be metallic. The strong electron-electron interaction, however, localizes the ninth electron on the copper site and makes YBCO an insulator.

The copper chains, together with the BaO layers, form a charge reservoir for the copper planes which results in the absence of Cu^{3+}. Despite their weak coupling the chains provide charge carriers for the planes and thus enable superconductivity by means of doping. The oxygen atoms in the top (and bottom) layers are only weakly bound and may be removed by annealing. This creates vacancies, interrupts the chains, reduces the coordination of Cu and varies the charge carrier concentration in the copper oxide planes.

Superconductivity is the vanishing electrical resistivity in a material at low temperatures. The underlying phenomenon in the metallic as well as the cuprate or pnictide based superconductors is that two conduction electrons form a Cooper pair and move through the material together. The pairing mechanism in the high-temperature superconductors (HTSC) is, however, still controversely discussed. Breaking the Cooper pairs by means of heating (above the critical temperature T_C) or applying a magnetic field (above the critical field $B_{C,2}$) destroys superconductivity.

3.8.3 Manganites

The perovskite oxide $LaMnO_3$ in its undoped form (Mn^{3+} ions only) is a paramagnetic insulator at room temperature. It turns into an A-type antiferromagnet below $T_{Néel}$ = 140 K [**19**] and into a dynamic Jahn-Teller [**20**] distorted system above T_{JT} = 750 K [**21**]. (An A-type antiferromagnet consists of ferromagnetically coupled atoms in layers which are in turn antiferromagnetically coupled to other layers [**22**]).

This already highly fascinating material attracts even more interest when it is doped with divalent (Ca, Sr, Ba, …) or tetravalent (Ce, Sn, Te, …) ions on the trivalent La lattice sites [**23**], [**24**]. These doped manganites ($La_{1-y}X_yMnO_3$, LXMO) exhibit a paramagnetic to ferromagnetic phase transition (at T_{Curie}) accompanied by an insulator to metal transition (at $T_{MI} = T_{Curie}$). Both phenomena, as well as colossal magnetoresistance, will be discussed in the following sections. Several studies have developed phase diagrams of the lanthanum manganites, showing that T_{MI} and magnetoresistance are optimized when 30% of the Mn^{3+} is converted to Mn^{4+} (by substituting divalent ions for La^{3+}) (e.g. [**25**], [**26**], [**27**], [**28**] and [**29**]. Thus, only $X_{0.3}$ samples, $La_{0.7}X_{0.3}MnO_3$ (X = La, Ca, Ce, Sr), will be treated in this work.

Figure 3-8 is taken from [**29**] and shows the phase diagram of $La_{1-x}Ca_xMnO_3$ with respect to temperature and composition (x-value). The phases are canted antiferromagnetic insulating (CAF), charge-ordered insulating (CO), ferromagnetic insulating (FI), ferromagnetic metallic (FM) and antiferromagnetic insulating (AF). Further notable phases include paramagnetic insulating (PI), unlabelled region in figure 3-8, and paramagnetic metallic (PM), found in LSMO.

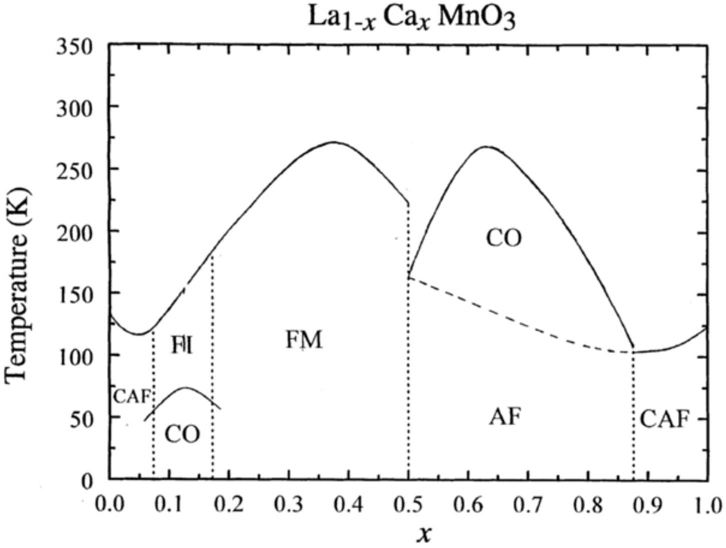

Figure 3-8 (taken from [29]): The horizontal axis shows the value of x in the formula. Phases include charge-ordered (CO), antiferromagnetic (AF), canted antiferromagnetic (CAF), ferromagnetic metallic (FM), ferromagnetic insulating (FI). The unlabelled region corresponds to the paramagnetic, insulating (semiconducting) phase.

The corresponding end members like $CaMnO_3$ or $SrMnO_3$ (Mn^{4+} ions only) are G-type antiferromagnets. (A G-type antiferromagnet features antiferromagnetic coupling between spins in all three directions [**22**]). It is easy to see that doping leads to a wide mixture of possible phases when the two magnetic orders mix. Also, for every dopant atom one charge carrier is created, because a Ca^{2+} ion on a La^{3+} lattice site leads to a Mn^{3+} ion becoming a Mn^{4+} ion to preserve charge neutrality. Divalent dopants thus create additional holes while tetravalent dopants create excess electrons. The exact stoichiometries may then be written as $\mathrm{La}^{3+}_{0.7}\mathrm{X}^{2+}_{0.3}\mathrm{Mn}^{3+}_{0.7}\mathrm{Mn}^{4+}_{0.3}\mathrm{O}^{2-}_{3}$ and $\mathrm{La}^{3+}_{0.7}\mathrm{X}^{4+}_{0.3}\mathrm{Mn}^{3+}_{0.7}\mathrm{Mn}^{2+}_{0.3}\mathrm{O}^{2-}_{3}$, respectively.

In Mn^{3+}, the four d electrons occupy four different d orbitals. The crystal field lifts the fivefold degeneracy of the d orbitals and creates the doubly degenerate e_g ($d_{3z^2-r^2}$ and $d_{x^2-y^2}$) and the triply degenerate t_{2g} (d_{xy}, d_{xz}, d_{yz}) set (c.f. figure 3-4). Coulomb repulsion between the 3d orbitals and 2p orbitals of surrounding oxygen atoms leads to energetically higher lying e_g orbitals, about 1 - 2 eV above the t_{2g} set. Consequently, these are occupied first with three electrons, one in each orbital. Because the Hund coupling is between 2 and 3 eV in the manganites, the fourth electron will be placed in an orbital of the e_g set, leading to parallel alignment of all spins (high spin state).

The two energetically higher d-orbitals, $d_{3z^2-r^2}$ and $d_{x^2-y^2}$, are split further by the so-called Jahn-Teller (JT) distortion which minimizes the energy of such systems as d^4 (high-spin), d^7 (low spin) or d^9. If the oxygen octahedron around Mn is slightly elongated in the z-direction, the Coulomb repulsion between O2p and $Mn3d_{3z^2-r^2}$ increases while it decreases between O2p and $Mn3d_{x^2-y^2}$. This lowering leads to the fourth electron occupying the latter orbital. Note that Mn^{2+} ($3d^5$) and Mn^{4+} ($3d^3$) do not show Jahn-Teller distortion.

The cooperative JT effect mentioned earlier is a direct result of the lattice distortion arising from elongated or compressed octahedral. A single distorted site locally creates huge stress while many distorted octahedra typically rearrange in order to compensate this. Common arrangements are to find alternating long and short axes in rows (antiferrodistortive) or to have all long axes aligned parallel (ferrodistortive).

Introducing doping, i.e. shifting manganese valence from Mn^{3+} to Mn^{2+} or Mn^{4+}, accordingly distorts the entire lattice because now elongated and regular oxygen octahedra are found in the structure. The cooperative and static JT effect in $LaMnO_3$ changes towards a dynamic JT distortion upon doping because the system can gain additional energy if the newly created charge carrier is delocalized over the entire crystal. The resulting fluctuation of a given lattice site between Mn^{3+} and Mn^{4+} and thus between JT distorted and undistorted oxygen octahedra means that a charge carrier and a lattice distortion move through the sample together as a polaron.

3.9 Materials: Properties

3.9.1 SE and DE, SE vs. DE

As mentioned above, the doped manganites LXMO (X = Ca^{2+}, Sr^{2+}, Ba^{2+}, …) have an additional hole on the manganese Mn^{4+} atom which is free to move. For instance, doping LMO with 10% of Ca^{2+} decreases the resistivity by two orders of magnitude and magnetism is observed. As a first approximation, Zener [**30**] described the effects of temperature and external magnetic field on the resistivity of these compounds in the framework of the so-called double exchange mechanism between Mn^{3+} ($3d^4$) and Mn^{4+} ($3d^3$) ions. More precisely, the competition between super exchange (SE) [**31**], [**32**] and double exchange (DE) [**30**], [**33**], [**34**] must be studied.

From a look at the macroscopic properties of the doped manganites, ferromagnetism and metallic conductivity, it is evident that there must be an exchange mechanism at work between the manganese spins although they are separated by oxygen ions. Because La^{3+} and O^{2-} have closed valence shells, it is the Mn ions that are responsible for these properties. A more detailed look at the position of the charge carriers reveals that strong Mn3d-O2p hybridization is found and that the holes in the transition metal oxides (TMOs) are often found in these hybrid orbitals.

Due to the large distance (about 4 Å) between two Mn spins, direct exchange will be neglected here and two indirect exchange mechanisms SE and DE will be discussed. The first mechanism is effective between two ions with the same valence, the latter is important for two ions with different valences, hence both are found in the doped manganites.

Superexchange is best explained using a linear chain with two Mn^{3+} and an O^{2-} ion, but is also valid for other configurations. The different possibilities were described by Goodenough, Kanamori and Anderson [**35**], [**36**], [**32**], [**37**]. The GKA rules give an overview over the possible weak and strong ferromagnetic and antiferromagnetic ordering in dependence of orbital geometry.

For two Mn^{3+} ions having 3d (e_g) orbitals overlapping with a suitable oxygen 2p orbital, the situation is described by figure 3-9. In this case, the Mn $3d_{3z^2-r^2}$ and O $2p_z$ orbitals are shown.

The small covalent contribution to the Mn-O bond results in direct exchange between Mn 3d and O 2p, in which case an antiparallel alignment of the spin moments is energetically favored. The Pauli Exclusion Principle guarantees that the two electrons in the O $2p_z$ orbital are aligned antiparallel as well which in turn leads to antiparallel alignment with the Mn ion´s spin on the left. The overall result is antiferromagnetic order between neighboring manganese ions. Although no actual movement of an electron takes place, this virtual hopping scenario is a means of delocalization for the electron. Virtual hopping is a perturbation that is admixed to the ground state and lowers its energy.

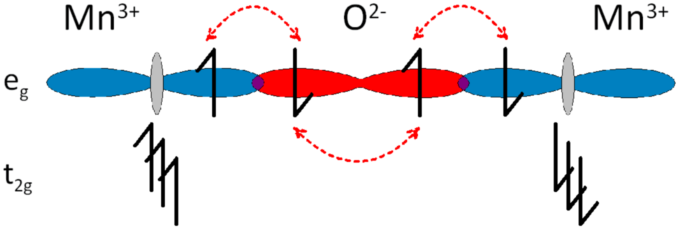

Figure 3-9: Sketch of super exchange between two Mn^{3+} ions via a central O^{2-} ion. The three black arrows symbolize the localized electrons in Mn 3d t_{2g} orbitals, while the single arrows represent itinerant electron spins in Mn 3d e_g and O2p orbitals.

For empty or filled orbitals that are aligned in a row, the exchange mechanism favors strong antiferromagnetism (AFM), 180° interaction between a filled and an empty orbital leads to weak ferromagnetism (FM). Finally, a 90° exchange path between filled orbitals also gives a weak and ferromagnetic order.

The second important exchange mechanism that is responsible for the intriguing physics of the manganites is the double exchange mechanism. It differs from SE in a way that two different valences are needed on the two associated lattice sites and that a charge carrier is actually moving.

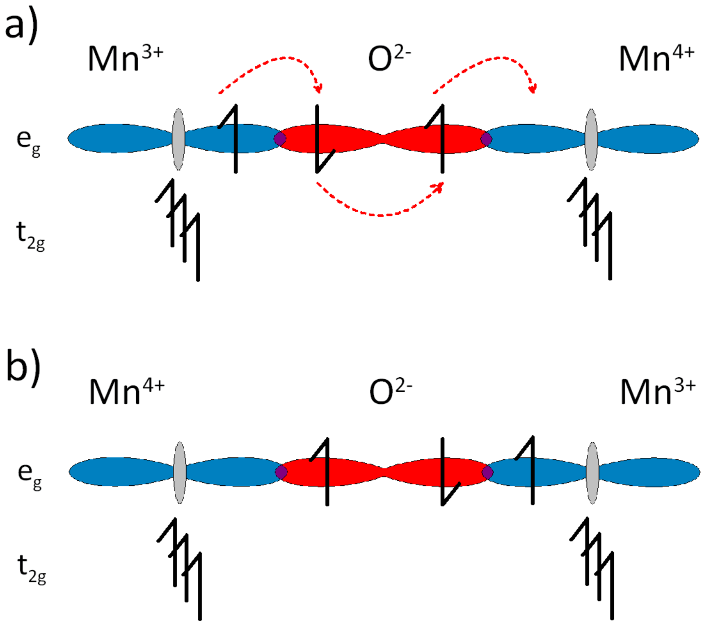

Figure 3-10: **Sketch of double exchange between a Mn^{3+} and a Mn^{4+} ion via a central O^{2-} ion. The three black arrows symbolize the localized electrons in Mn 3d t_{2g} orbitals, while the single arrows represent itinerant electron spins in Mn 3d e_g and O 2p orbitals. The hopping process is sketched by red broken arrows. Please note that Mn^{3+} and Mn^{4+} change place before a) and after b) the electron has moved.**

Figure 3-10 schematically shows the DE process where an itinerant e_g electron from Mn^{3+} hops to the neighboring Mn^{4+} ion via a central O^{2-} ion. The three arrows below the Mn $3d_{3z^2-r^2}$ orbitals represent the localized spins of the three t_{2g} electrons. As mentioned earlier, a parallel alignment of all t_{2g} and e_g spin moments is favored because the Hund´s coupling energy in the manganites is rather large. The actual transfer of the itinerant electron thus depends strongly on the configuration of these core spins. The largest possible energy gain for the system is realized, if the configuration in figure 3-10 is given.

This is conveniently described by an effective hopping matrix element, $t_{eff} = t \cos(\theta_{ij}/2)$, where t corresponds to the overlap between the involved orbitals and θ_{ij} is the angle between the spin at site i and the core spin at site j. One can see that the hopping amplitude is biggest for parallel alignment and vanishes for antiparallel alignment of itinerant and core spin [**33**].

The fact that in the DE process an electron actually travels, in contrast to the virtual hopping found in SE, makes it important not only for the magnetism but also for the transport properties of the system at hand. It is an effective conduction mechanism and leads to the metallic behavior of the doped manganites. It is also the first proposed model that explains their magnetoresistance (MR) effect. Jonker [**25**] and van Santen [**26**] found a decrease of the resistivity of $La_{1-x}Sr_xMnO_3$ (LSMO), $La_{1-x}Ca_xMnO_3$ (LCMO) and $La_{1-x}Ba_xMnO_3$ (LBMO) for x around 0.3 near their respective Curie temperatures T_{Curie}. At an applied field of 0.3 T Volger [**38**] found a 7% decrease of conductivity in $La_{0.8}Sr_{0.2}MnO_3$. Negative magnetoresistive effects were later found in epitaxial manganite films by Kusters [**39**] ($Nd_{0.5}Pb_{0.5}MnO_3$) and von Helmolt [**40**] ($La_{0.67}Ba_{0.33}MnO_3$).

Parallel alignment of spins by an external magnetic field leads to high hopping amplitudes and low resistivity. At low temperatures, with respect to T_{Curie}, the DE aligns most spins ferromagnetically, at high temperatures the thermal disorder dominates. The biggest influence of the magnetic field is found near the transition temperature.

The term colossal magnetoresistance (CMR) was coined in the middle of the 1990s when a decrease of resistivity of several orders of magnitude was found in epitaxial thin films of LCMO by Jin [**41**]. This also led to an overall increase in the popularity of the manganites as a model system for the study of strongly correlated electrons in solids. The timing was perfect because in 1986 Bednorz and Müller [**42**] had discovered high-temperature superconductivity in another perovskite oxide $La_{5-x}Ba_xCu_5O_{5(3-y)}$. Intensified research on the perovskite oxides quickly lead to a series of important discoveries and improved understanding of the basic physics of strongly correlated electrons.

3.9.2 Beyond the SE/DE competition

The competition between SE and DE qualitatively explains most of the phenomena which make the manganites one of the most studied material class in recent years. However, they cannot account for a concise description of the experimentally observed R(T) behavior, i.e. the metal-to-insulator transition, because many approximations are made.

For example, no lattice distortions from e.g. a dynamical JT effect are considered (possibly changing Mn-O-Mn bond angles and further changing 3d orbital splitting), no differences are made in the Coulomb interactions between Mn^{3+} and Mn^{4+} and their environment (creating polarons and changing orbital overlap). Interactions were only assumed to take place between orbitals with large overlap, atom orbitals instead of hybridized Mn 3d-O 2p-type orbitals were used and so on.

The phase diagrams of LSMO, LCMO and LBMO show further peculiarities, demonstrating that for a complete description many more aspects must be kept in mind. There are ferromagnetic insulating (FMI) and antiferromagnetic metal (AFM) regions, as well as paramagnetic insulatoring (PI) and metallic ones (PM), which are hard to explain by SE and / or DE alone. What is more is the non-linear dependence of properties on the size of the dopant atom: While Ca (134 pm) doping leads to semiconducting behavior above T_{Curie}, Sr (144 pm) doping leads to metallic conductivity and Ba (161 pm) doping gives semiconductivity again.

The isotope effect when replacing ^{16}O by ^{18}O in $La_{0.8}Ca_{0.2}MnO_3$ is 21 K [**43**]. This is a huge value, which is possible only under the assumption of strong electron phonon coupling, i.e. the formation of polarons. In the extreme case, the orbital polaron looks like figure 3-11 where 6 occupied Mn $3d_{3z^2-r^2}$ orbitals point towards a central hole [**44**]. This configuration is proposedly found in LCMO above T_{MI} and is used to explain the insulating behavior. The competition between delocalization and localization is key to explaining the physics behind the metal-to-insulator transition.

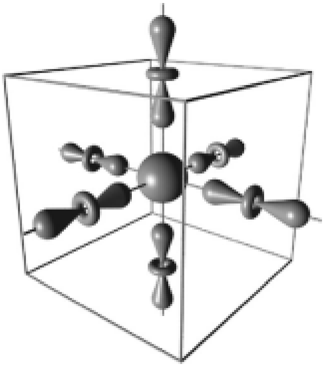

Figure 3-11 (taken from [44]**: An orbital polaron as a way of localizing/trapping a charge carrier.**

As a result of these approximations, there is a discrepancy between R(T) experiments and theoretical values of T_{Curie} in the manganites, which Millis et al. aptly described as “Double Exchange Alone Does Not Explain the Resistivity of $La_{1-x}Sr_xMnO_3$” [**29**]. The authors struggled to explain the incorrect absolute value of resistivity, a too weak doping dependence and the wrong behavior of resistivity below T_{Curie} in an applied magnetic field. They suggested including strong electron-phonon interactions, and all entailing implications, in theory to get better agreement. This also helps to explain the huge differences between single crystal and epitaxial thin film results because it allows accounting for strain imposed on the film by the lattice mismatch between film and substrate.

Finally, one other prominent theoretical model will be briefly mentioned here, the phase separation scenario by Dagotto et al. [**45**]. In this approach the coexistence and competition between ferromagnetic metallic and antiferromagnetic insulating regions is used to model the properties of the manganites. The sample may be viewed as FM clusters with randomly oriented moments separated by regions where Charge Order (CO) Antiferromagnetism is stabilized. In this model the metallic regions would be dominated by DE while the properties of the insulating regions are governed by SE. A percolative approach might then explain the insulator-metal-transition in a way that conducting pathways are formed below T_{MI} and are broken above. Similarly a magnetic field increases the size of the FM clusters and creates more percolation paths which lead to increased conductivity again. This is currently the most widely accepted theory.

3.9.3 Competition between superconductivity and ferromagnetism

The antagonistic materials properties superconductivity (SC) and ferromagnetism (FM) can be united in artificial heterostructures to study their interaction. Proximity between superconductivity and ferromagnetism was earlier studied in detail in metallic ferromagnets and conventional superconductors [**46**], [**47**]. With the advance of growth techniques like MBE or PLD the fabrication of all-oxide heterostructures with sharp interfaces became possible.

This creates an interface where the parallel spins of the ferromagnet meet the antiparallel spins in Cooper pairs. The magnetic field, via the Lorentz force, exerts different momenta on the two electrons of a Cooper pair condensate and tends to break it (orbital mechanism [**48**]). If ferromagnetic domains are smaller than the superconducting coherence length, the Cooper pairs “feel” - on average - antiferromagnetism [**49**]. This so-called cryptoferromagnetic state is allowed.

The exchange field in a magnetically ordered state tends to align spins parallel (see chapter 3.9.2) which leads to pair-breaking as well (paramagnetic effect [**50**]). This second effect reduces superconductivity in samples which contain magnetic impurities [**51**].

If the two materials, FM and SC, meet directly at the interface, pair-breaking via the orbital mechanism dominates. If they are decoupled by for instance a thin insulating layer, the paramagnetic effect via the stray field dominates the pair-breaking. To study such bilayers, thin films of the HTSC YBCO were epitaxially grown on STO substrates and covered by LCMO layers. The results are presented in chapter 8.

3.9.4 Specific materials properties of the investigated samples

Epitaxial thin films of $La_{0.7}Sr_{0.3}MnO_3$ behave like a ferromagnetic metal at room temperature and become a paramagnetic metal above T_{Curie} = 350 K, where they show the CMR effect. $La_{0.7}Ca_{0.3}MnO_3$ is a ferromagnetic metal below T_{Curie} = 270 K and a paramagnetic semiconductor above. It also shows the CMR effect near T_{Curie}.

Doping with Ce^{4+} on the other hand (LCeMO) should consequently lead to a mixture of 70% Mn^{3+} and 30% Mn^{2+} ($3d^5$) with an additional electron in the e_g orbital set. If the double exchange model is valid for all ions with different valences, then LCeMO should behave similar to LCMO. In fact the double exchange model was applied by [**52**] to LCeMO bulk crystals to include the Mn^{2+}/Mn^{3+} system. The authors presented temperature-dependent resistivity and thermopower data but were careful not to mention the exact valence of Cerium which they did not measure directly.

The fact that LCeMO also shows a metal-insulator transition at T_{Curie} = 260 K and ferromagnetic order is a strong indication for the double exchange mechanism; the question is whether or not it takes place between Mn^{2+} and Mn^{3+}.

3.9.5 Structure and tolerance factors

Because the e_g orbitals have lobes that point towards the oxygen sites, the 3d-2p hybridization strongly depends on the Mn-O bond length. Furthermore, because band width (hopping integral t) and band filling (doping level x) determine the stable modification of the manganites, it is not only the dopant concentration but also the dopant´s effect on the lattice that directly determines the electronic properties of the system.

Doping and its effect on the crystal structure can never be separated from each other because of the different ionic radii of the atoms. The effect of various ratios of cations and anions are best explained using the Goldschmidt tolerance factor [**53**] below. Further information can be found in textbooks on inorganic chemistry, e.g. [**18**].

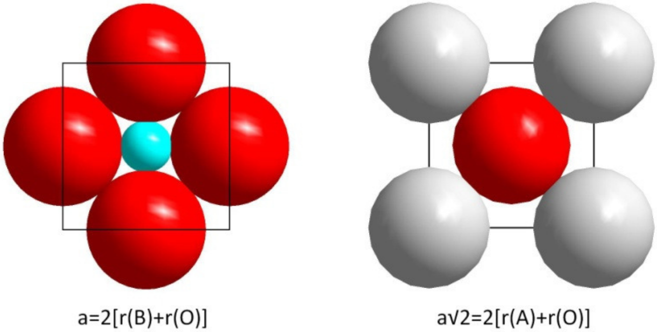

Figure 3-12: **A BO_2 layer (left) and an AO layer (right) of a cubic perovskite unit cell. The lattice parameter a can be described in terms of A-site and B-site ionic radii (r_A, grey - r_B, cyan) together with oxygen r_O (red).**

Deriving the size of a unit cell from the radii of the A, B and O ions, two easy possibilities are displayed in figure 3-12. On the one hand, $r_A+r_O = ½\, a\sqrt{2}$ (diagonal), on the other hand $r_B+r_O = ½\, a$ (edge). The tolerance factor is the ratio of these two descriptions:

$$t = \frac{r_A + r_O}{\sqrt{2}(r_B + r_O)}$$

Stable perovskites are found for tolerance factors between 0.75 and 1.05 with the ideal cubic ($a = b = c$, $\alpha = \beta = \gamma = 90°$) perovskite at $t = 1$. For values below $t = 0.75$ the sesquioxide (corundum) form is found in which oxygen forms a close packed structure and equally sized A and B ions occupy octahedral interstitial sites. For values above 0.75 the perovskite structure is found, however it is rhombohedral for $t < 0.96$ ($a = b = c$, $\alpha = \beta = \gamma \neq 90°$; $<120°$) and orthorhombic for $0.96 < t < 1$ ($a \neq b \neq c$, $\alpha = \beta = \gamma = 90°$).

The ABO_3 structure consists of AO_3 cubic close packed layers, where A and O have ideally the same radii. According to geometrical considerations, octahedral interstices in this arrangement can accommodate ions with radii approximately equal to $(\sqrt{2}\text{-}1)r_O$ or $0.414\, r_O$. For an oxygen radius of 140 pm, this gives an ideal value of $r_B = 58$ pm. The radii should be chosen based on the actual sites that the ions occupy in the perovskite structure, i.e. 12-coordinate A sites (La and substituting dopants in

LXMO, Sr in STO), 6-coordinate M sites (Mn in LXMO, Ti in STO) and 2- or 6-coordinate oxygen sites.

While almost all articles cite Shannon et al. [**54**], there is disagreement about the choice of the coordination sphere. The A-site is surrounded by twelve oxygen atoms with a distance of ½ a $\sqrt{2}$ each (2.8 Å for a cubic unit cell with a 4 Å lattice constant). The B-site is surrounded by 6 oxygen atoms with a distance of ½ a (2 Å) each. Finally, the O-site is two-fold coordinated by Mn neighbors within 2 Å and 4-fold coordinated by lanthanum atoms with distances of 2.8 Å. The question thus arises whether O has a coordination number (CN) of 2 or 6. The difference in ionic radii is small, 135 pm for CN = 2 and 140 pm for CN = 6. Unfortunately, there is disagreement in literature, the underlying work, however, strictly uses a value of 140 pm unless otherwise stated. Table 3-1 gives a list of all necessary ionic radii used in this work for coordination numbers of 9 and 12 for the A-site ions, 6 for the B-site ions (High Spin HS and Low Spin LS where possible) and the effective ionic radius of oxygen for coordination numbers 2 and 6.

Element	CN	IR [Å]	Element	CN	IR [Å]
La^{3+}	12	1.36	**La^{3+}**	9	1.22
Ca^{2+}	12	1.34	**Ca^{2+}**	9	1.18
Ce^{3+}	12	1.34	**Ce^{3+}**	9	1.20
Ce^{4+}	12	1.14	**Ce^{4+}**	9	1.01
Sr^{2+}	12	1.44	**Sr^{2+}**	9	1.31
Mn^{2+}	HS	0.83	**Mn^{2+}**	LS	0.67
Mn^{3+}	HS	0.645	**Mn^{3+}**	LS	0.58
Mn^{4+}		0.53			
Ti^{4+}		0.605			
O^{2-}	6	1.40	**O^{2-}**	2	1.35

Table 3-1: List of 12-coordinate (9-coordinate) A-site Shannon (Shannon1976) [54] **effective ionic radii, 6-coordinate B site radii (high spin HS / low spin LS where possible) and 2- / 6-coordinate radii for oxygen ions. All values are given in Ångstrom.**

As a result, the following tolerance factors can be calculated for some selected manganite and titanate perovskites:

A / B site of ABO_3	CN9, r_O=135pm	CN12, r_O=135pm	CN9, r_O=140pm	CN12, r_O=140pm
***SrTi**	0,96	1,01	0,96	**1,00**
***CaTi**	0,92	0,97	0,91	**0,97**
***LaMn**	0,91	0,96	0,90	**0,95**
***CaMn**	0,90	0,95	0,89	**0,95**
SrMn	0,94	0,99	0,94	**0,98**
$Ce^{3+}Mn^{3+}$	0,90	0,95	0,90	**0,95**
$Ce^{4+}Mn^{2+}$	0,77	0,81	0,76	**0,81**
$(La,Ce^{3+})Mn$	0,91	0,96	0,90	**0,95**
$(La,Ce^{4+})Mn$	0,86	0,91	0,86	**0,91**
(La,Ca)Mn	0,92	0,98	0,92	**0,97**
(La,Sr)Mn	0,94	0,99	0,93	**0,98**

Table 3-2: Tolerance factors for coordination numbers 9 and 12 with oxygen radii of 135 pm and 140 pm, respectively for selected manganite and titanate perovskites ABO_3 (B = Mn, Ti). The doped manganites at the bottom are of the $La_{0.7}X_{0.3}$ (X = Ce^{3+}, Ce^{4+}, Ca^{2+}, Sr^{2+}) type. The last column is highlighted because CN = 12 and r_O = 140 pm are used in this work unless otherwise stated.

Of the compounds in the upper part of tTable 3-2, the ones marked with an asterisk are stable and have tolerance factors between 0.95 and 1.01 (CN12, $r(O^{2-})$ = 140 pm). Using average values of ionic radii for the doped lanthanum manganites, one obtains values of 0.97 for $La_{0.7}Ca_{0.3}MnO_3$, 0.98 for $La_{0.7}Sr_{0.3}MnO_3$ (in agreement with literature e.g. the review on doped manganites by Coey [**23**], the review on CMR by Tokura [**24**] and textbooks e.g. [**55**]) but only 0.91 for $La_{0.7}Ce_{0.3}MnO_3$. Assuming La^{3+}, Ce^{3+} and Mn^{3+} the tolerance factor is increased to 0.95. The compound with the highest tolerance factor also has the highest Curie temperature.

This suggests that the combination of Ce^{4+} and Mn^{2+} would have two disadvantages at once. Not only is Ce^{4+} much smaller than the oxygen site (114 vs. 140 pm) it is supposed to fill but additionally the shift from Mn^{3+} to Mn^{2+} (64.5 vs. 83 pm) creates a B-site ion that is too big for its octahedral interstice (ideal r_B = 58 pm).

Changing the amount of doping or the ionic radius of the dopant leads to huge loads of stress which is typically reduced by a cooperative tilting of the MnO_6 octahedra. This, however, changes the Mn-O-Mn bond angle and drastically affects the electronic and magnetic properties of the sample. Thus, while $La_{0.7}Sr_{0.3}MnO_3$ is a ferromagnetic metal, $Pr_{0.7}Ca_{0.3}MnO_3$ is a ferromagnetic insulator because distortion (129 pm Pr instead of 136 pm La on 140 pm O site) leads to a Mn-O-Mn bond angle decrease from 166° to 156°.

Much cited work by Hwang et al. [**56**] studied the effects of lattice distortions on the magnetoresistance of doped LMO. The authors presented a phase diagram of temperature vs. tolerance factor for 30% doped rare earth manganites. It is reproduced in figure 3-13. Please note that Hwang used ninefold coordination of A-site ions. Thus, for $La_{0.7}Sr_{0.3}$ Hwang gives a $<r_A>$ value of 1.24 Å, while a coordination number of 12 would yield $<r_A>$ = 1.38 Å. The trends are the same, though as is evident from Table 3-2 comparing the tolerance factors for ninefold and twelvefold A-site coordination for oxygen radii of 135 and 140 pm respectively.

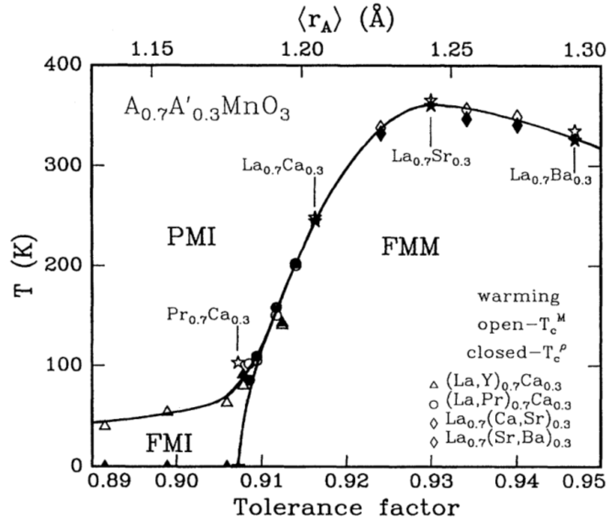

Figure 3-13 (taken from [56]: Phase diagram of the doped manganites showing different ground states (ferromagnetic metallic FMM, paramagnetic insulating PMI, ferromagnetic insulating FMI) in dependence of tolerance factor and temperature.

The internal pressure on the MnO_6 octahedra was varied systematically by changing the average A-site radius $<r_A>$ while keeping the Mn^{3+}/Mn^{4+} ratio constant. One finding is that with decreasing $<r_A>$ the transition temperature T_{MI} decreases while the magnetoresistance increases. The most important effect of this decrease is the change of the Mn-O-Mn bond angle ϕ to values lower than 180°. Despite the smaller distance between neighboring Mn ions, the hopping amplitude gets smaller. For the case of SE [**57**], [**58**] it has been demonstrated that the Mn-O-Mn angle and the Néel temperature $T_{Néel}$ are proportional via $\cos^2\phi$. The DE mechanism has an angular dependence as well, however, here it is the angle between the core moments that determines the transfer probability of an electron to a neighboring site.

Although it is the aim to alter either the band filling via doping or the band width via $<r_A>$, both change at the same time because more doping of course exchanges A-site cations. The findings by Hwang suggest that the tolerance factor determines not only the transition temperature but also the ground state. This was disproved by suitable samples ($La_{0.7}Ca_{0.11}Sr_{0.19}MnO_3$ and $La_{0.32}Pr_{0.38}Sr_{0.3}MnO_3$) that have equal x and $<r_A>$ by

Attfield et al. [**59**], [**60**]. They could show that disorder on the cation sites is important as well, some physical properties were found to change monotonically with the variance of the A-site ionic radii distribution $\sigma^2 = \langle r^2_A \rangle - \langle r_A \rangle^2$.

While LBMO has a tolerance factor that is closer to unity (c.f. figure 3-13) than LSMO, it's Curie temperature is lower because Ba^{2+} (161 pm) creates much more disorder on the La^{3+} (136 pm) A-site than Sr^{2+} (144 pm). The resulting oxygen displacement affects the physical properties stronger than expected from the tolerance factor alone.

An overview of variance values (A-site disorder) in dependence of doping composition is presented in Table 3-3 Again both Ce^{4+} and hypothetical Ce^{3+} are shown for comparison and following discussion. There are about two orders of magnitude between $La_{0.7}Ce^{4+}_{0.3}MnO_3$ and $La_{0.7}Ce^{3+}_{0.3}MnO_3$ with the value for Ce^{4+} being on the verge of phase separation. For large cation disorder, i.e. values of the variance of A-site ionic radii above $1 \cdot 10^{-2}$, phase separation was proposed by [**59**] and is indeed found in LCeMO.

For CN9 the ideal r_A is 1.30 which gives a tolerance factor of 1. Deviations from this value yields oxygen displacement due to the A-site disorder. Table 3-3 shows that $La_{0.7}Ce_{0.3}$ has the largest variance, especially if tetravalent Ce is regarded.

Composition	$\langle r_A \rangle$ Å CN9	variance	$\langle r_A \rangle$ Å CN12	variance
$La_{0.7}Ca_{0.3}MnO_3$	1,21	2,7E-04	1,35	8,4E-05
$La_{0.7}Sr_{0.3}MnO_3$	1,24	1,9E-03	1,38	1,3E-03
$La_{0.7}Ce^{4+}_{0.3}MnO_3$	1,15	8,7E-03	1,29	1,0E-02
$La_{0.7}Ce^{3+}_{0.3}MnO_3$	1,21	8,4E-05	1,35	8,4E-05

Table 3-3: Variance of the average A-site cation ionic radius according to Attfield for different combinations of A-site compositions and different coordination numbers 9 and 12.

Changing the amount of doping or the ionic radius of the dopant leads to huge loads of stress which is typically reduced by a cooperative tilting of the MnO_6 octahedra. This, however, changes the Mn-O-Mn bond angle and drastically affects the electronic and magnetic properties of the sample. Thus, while $La_{0.7}Sr_{0.3}MnO_3$ is a ferromagnetic metal, $Pr_{0.7}Ca_{0.3}MnO_3$ is a ferromagnetic insulator because distortion (129 pm Pr instead of 136 pm La on 140 pm O site) leads to a Mn-O-Mn bond angle decrease from 166° to 156°.

3.9.6 Effects on lattice structure

Tolerance factors that differ from unity create distorted crystal structures, where the MnO_6 octahedra may tilt and / or rotate out of their cubic (Pm3m) equilibrium position. This leads to the superstructures as depicted in figure 3-14.

For the orthorhombic case (space group Pnma) the lattice constants change, a becomes $a\sqrt{2}$, b becomes $b\sqrt{2}$ and c becomes 2c. Furthermore, the new unit cell is rotated by 45° with respect to the original lattice.

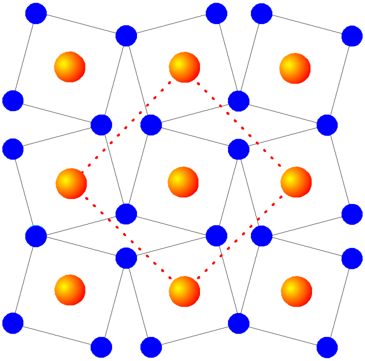

Figure 3-14: **Orthorhombic superstructure of the perovskites in the a-b-plane. The sketch shows Mn atoms (orange) and their tilted oxygen (blue) octahedra in a top view. The orthorhombic unit cell is marked by the dashed line.**

3.9.7 Charge, Spin and Orbital Order

Last but not least, three more phenomena have to be mentioned briefly in this section, namely charge, spin and orbital ordering. For reasons of brevity, only the results but not the origin will be explained. More details are found in a review article by Tokura [**61**].

Charge ordering (CO) occurs when charges are strongly localized on their lattice sites (i.e. when Coulomb repulsion is bigger than the energy gain from hopping), leading to superlattices. Polarons represent a form of charge order as well. In two dimensions stripes and checkerboard patterns are often formed, in three dimensions the patterns are more complex. Figure 3-15 shows a prominent example for charge ordering found in half-doped $La_{0.5}Sr_{0.5}MnO_3$.

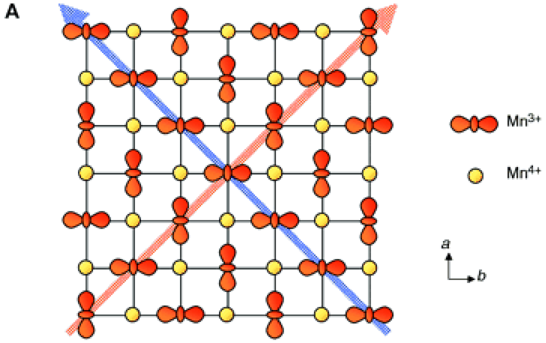

Figure 3-15 (taken from [61]**: Sketch of (orbital and) charge ordering arrangement (CE-type) as found in the MnO_2-planes of half-doped manganites $La_{0.5}X_{0.5}MnO_3$.**

Spin ordering (SO) was described earlier as the alignment of spin moments due to interactions with their environment via SE or DE. Figure 3-16 presents two important types of spin ordered lattices found in the perovskites, namely A- and G-type Antiferromagnetism. Other relevant types are F-type FM (sometimes called B-type, all spins aligned parallel) or mixtures like CE-type (checkerboard arrangement of C- and E-type building blocks, cf. figure 3-15).

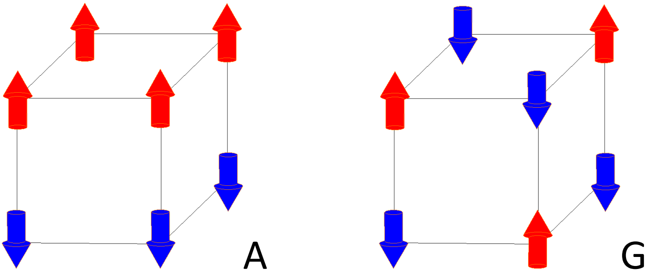

Figure 3-16: **Two examples of spin order, A and G-type antiferromagnetism found in $LaMnO_3$ and $CaMnO_3$ ($SrMnO_3$), respectively.**

Finally, orbital ordering (OO) is the underlying cause for the anisotropy of the electronic properties found in many complex systems. Usually, electrons simply fill up the available orbitals with increasing energy. In the manganites with strong Coulomb interactions and even stronger Hund´s coupling this is not always possible. This creates an additional, orbital degree of freedom that must be considered. Orbital ordering is often connected with cooperative Jahn-Teller distortions.

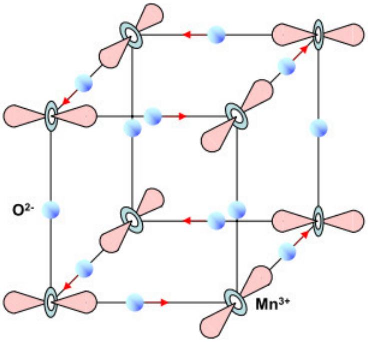

Figure 3-17 (from [55]: Orbital order and displacement of oxygen atoms in $LaMnO_3$ due to the cooperative Jahn-Teller effect. The individual MnO_6 octahedra are elongated in one direction, avoiding each other. The e_g orbitals split, only $3d_{3z^2-r^2}$ is occupied.

Of course none of these orderings can be viewed alone. Orbital order creates spin order because if the Mn $3d_{3z^2-r^2}$ orbitals are oriented as seen in figure 3-17, the magnetic moments of the e_g electrons in these orbitals are ordered as well. Similarly, a polaron (fig. 3-11) orders charges and orbitals at the same time. Since charge ordering leads to localized spins as well, these two phenomena cannot be treated individually either. It is exactly this interplay between the three degrees of freedom that creates the rich phase diagrams of the manganites.

4 EXPERIMENTAL

This chapter introduces the experimental details of the measurements, i.e. the equipment, the sample preparation and the data acquisition and manipulation. Techniques include XPS, XPD and XAS-related methods. The sample deposition by means of pulsed laser deposition was done by Robert Werner [**62**], [**63**] from the physics department at the Eberhard-Karls University of Tuebingen, only minor cleaning steps were necessary before transfer into the UHV chamber. Data acquisition and analysis includes treatment of XPS, XPD and XAS data as well as calculated Multiple Scattering Cluster (MSC) results from both the EDAC code and data provided by another cooperation partner, Christian Langheinrich and Angelika Chassé of Martin-Luther University in Halle.

4.1 X-ray Photoelectron Spectroscopy and Diffraction XPS / XPD

XPS and XPD measurements were performed at the home lab in a custom-built ultra-high vacuum (UHV) chamber with a base pressure in the low 10^{-10} mbar range. Using a SPECS XR 50 twin anode x-ray source (Berlin, Germany) samples were irradiated with 250 W Mg K_{α} (1253.6 eV) or 350 W Al K_{α} (1486.6 eV) light. The photoelectron kinetic energies were measured using a five-channel SPECS PHOIBOS 100 hemispherical electron energy analyzer and recorded with the specs SPECS LAB 2 software package. For automated XPD experiments, two computer-controlled stepper motors (nanotec GmbH, Feldkirchen, Germany) manipulated the polar and azimuthal angle of the sample with respect to the analyzer. Angular distribution curves were recorded using the software CROISSANT by kspace (Zurich, Switzerland).

The analyzer allows the detection of electrons either with high angular resolution or with high energy resolution by selecting appropriate pass energies (PE) and lens modes. Low pass energies of 10 to 30 eV (typically used for XPS) yield low electron counts with high energy resolution, high pass energies around 100 eV (typically used for XPD) give large electron counts at low energy resolution. The different lens modes of the PHOIBOS 100 analyzer allow the acquisition of high-resolution photoemission spectra with low angular / high energy resolution (±4° / pass energy 20 eV) and of photoelectron diffraction patterns with high angular / low energy resolution (±1° / pass energy 100 eV).

After an overview scan to roughly identify the sample composition and cleanliness, photoelectron spectra of the relevant core levels are measured to confirm the chemical state of the elements and to determine the stoichiometry of the sample. The core level spectra were analyzed by peak fitting using UNIFIT [**64**].

Two automated stepper motors control the three–axis goniometer and allow changing the azimuthal (ϕ: 0° to 360°) and polar (θ: -70 to + 70°) orientation of the sample with respect to the analyzer. The software croissant (kspace, Zurich, Switzerland) was used to record polar scans with a step width of 0.5° and azimuthal scans with a step width of 1°. Polar scans were taken in the main crystallographic directions of the cubic samples, namely [100] and [110] and their equivalents, after precisely locating these planes by an azimuthal scan at a polar angle of 45°. Using the photoemission lines of the constituting atoms information on the local structure around these elements was obtained.

In order to run a XPD experiment one starts by identifying the normal emission or θ=0° direction of a polar scan. For this purpose the sample is tilted along θ and the intensity of photoelectrons coming from a given element is recorded. The maximum intensity is typically found at normal emission, corresponding to the [001] direction. To identify the two low index crystallographic directions [100] and [110], the sample is then tilted to a polar angle of 45° and rotated azimuthally by 360° along ϕ. Due to the fourfold symmetry of the cubic system, four equivalent patterns are found in the recorded signal with maximal intensity located in the [101], [0-11], [-101] and [011] direction. These maxima are aligned to appear at the azimuthal angles 45°, 135°, 225° and 315°. This gives complete control over the orientation of the sample with respect to the analyzer.

In all further scans, the data for the angular distribution curves of all elements are recorded simultaneously at the particular angles of emission, whether for polar scans along the main azimuthal directions [100] and [110] or for azimuthal scans along the [101] direction. Three to four nominally equivalent polar scans, i.e. along [100],

[010], [-100] and [0-10] are routinely measured to ensure the reproducibility and the correct alignment of the crystal.

4.2 ANKA / ELETTRA synchrotron radiation sources

For XAS, XLD and XMCD measurements, a tunable light source is necessary. These measurements were performed at two synchrotron facilities in Germany and Italy. The ANKA (Angströmquelle Karlsruhe, angstrom source) storage ring located at the Forschungszentrum Karlsruhe is a third generation synchrotron source with currently 17 beamlines offering research possibilities with highly brilliant, high intensity radiation from the IR to the hard x-ray regime. The WERA (Weichröntgenanalytik, soft x-ray analytics) beamline provides users with soft x-rays with energies of 100 to 1500 eV and an energy resolution of more than 10000 (at the N K absorption edge) from a dipole source. Total electron yield (TEY, surface sensitive) and fluorescence yield (FY, bulk sensitive) x-ray absorption studies for determination of the unoccupied electronic structure can be measured simultaneously. The possibility to linearly polarize the incoming light allowed the study of angle resolved orbital occupation. Further information on WERA is available from the ANKA Instrumentation Book 2010 [**65**].

The APE-HE (Advanced Photoelectric Effect, High Energy) beamline at the ELETTRA synchrotron facility in Trieste, Italy provides 140 – 1500 eV soft x-rays from an undulator source. This yields an energy resolution of better than 8000 at the N K absorption edge with a flux of roughly $5 \cdot 10^{10}$ photons/s. The sample holder in the UHV chamber is equipped with a 0.1 Tesla (pulsed) electromagnet, allowing the easy acquisition of XMCD spectra in TEY and FY detection mode for element-specific spin and orbital moment studies. Details on APE-HE are found in [**66**].

4.3 Sample preparation

4.3.1 STO

The strontium titanate samples are commercially available 10x10 mm $SrTiO_3$ (100) single crystals (Crystal GmbH, Germany) which were studied under various preparation conditions. The sample denoted “as received” was cleaned in acetone and isopropanol in an ultrasonic bath before being transferred into the UHV chamber. The sample denoted as “BHF etched” was wet-chemically etched with buffered HF solution (BHF) and annealed in oxygen to remove alkaline SrO and obtain the chemically inert (and thermodynamically more stable) TiO_2 termination [**67**], refined by [**68**]. This procedure uses the conversion of SrO to $Sr(OH)_2$ in demineralized water and the subsequent dissolution in NH_4F-buffered hydrofluoric acid. Because HF is capable of completely dissolving STO and creating etch pits, the dipping time must be minimized, i.e. selective etching of strontium oxide must be ensured. Only the SrO-termination exhibits a significant inward displacement of the Sr atoms [**69**], leading to a polarized surface which then attracts and reacts with H_2O molecules. The formation of a Sr-hydroxide complex by soaking in demineralized water, confined to the topmost SrO layer, increases the selectivity of solubility of the AO layer.

A possible contamination by $SrCO_3$ is also removed in this second step. The recrystallization of the surface takes place at 900 °C in oxygen. This second step is needed to remove the remnants of the previous treatment and to create sharp, unit cell (0.39 nm) high terraces whose width depends on the crystal miscut. No further surface treatment was performed after transfer into the UHV system. The third sample, named “Ar^+ etched” here, was sputter cleaned in-situ with 500 eV Ar^+ ions for 2x15 min followed by annealing at 620 °C for 30 min. Finally, the sample “O_2 annealed” was additionally heated in an oxygen atmosphere at 4×10^{-5} mbar O_2 at 670 °C for 30 minutes [**70**], [**71**].

4.3.2 LXMO treatment

LXMO and LCMO/YBCO bilayer samples were routinely cleaned by ultrasound bathing in ethanol and acetone before transfer into the UHV chamber. LXMO samples were further heated at 450 °C in an oxygen atmosphere of around $4x10^{-5}$ mbar for 10 - 15 minutes [**72**] to remove contaminations like adsorbed water and adventitious carbon (monoxide). The bilayer samples were not treated in this way to avoid interfacial diffusion.

4.4 Data analysis

This segment deals with the data acquisition and analysis of XPS and XPD data (3.4.1 & 3.4.2), calculated MSC data (3.4.3) and XAS data (3.4.4).

4.4.1 Specs Lab, Unifit and Croissant

The specs PHOIBOS hemispherical electron energy analyzer can be operated by the Specs Lab 2 software suite for XPS measurements or by the custom-made Croissant software for XPD measurements. Necessary parameters are the energy range of acquisition (overview or detail scan), the appropriate lens mode (i.e. “high magnification” for small samples or “high angular dispersion” for diffraction studies), dwell time per data point, step size between points, number of scans and pass energy for energy resolution.

Croissant features additional parameters for manipulation of the sample with respect to the analyzer, i.e. polar and azimuthal angle scan range.

For the determination of valence states or the number of components in a core level peak, fitting is performed with the Unifit software package by R. Hesse and T. Chassé [**64**] which allows the description of line shapes by Gaussian and / or Lorentzian curves.

4.4.2 XPD data manipulation, intensity ratio procedure

The usual approach of presenting anisotropies in XPD is to show the so-called χ-functions, which represent the relative intensity modulations $\chi = (I_{exp}-I_0)/I_0$ with respect to a reference intensity I_0, which represents an angular average. In case of azimuthal scans $I_{exp}(\phi)$ the reference intensity I_0 is just a constant, which may be determined by performing an angular average of the intensity data from the azimuthal scan. In case of polar scans $I_{exp}(\theta)$ the reference $I_0 = I_0(\theta)$ also becomes dependent on the polar angle. This $I_0(\theta)$ may be determined experimentally by measuring the intensity from a polycrystalline sample in dependence on the polar angle. Alternatively, $I_0(\theta)$ may be approximated by fitting a smooth, angle dependent model function to the experimental polar scan data $I_{exp}(\theta)$.

However, in case of our present data sets the general intensity decrease at higher polar angles turned out to be particularly sensitive to the kinetic energy of the photoelectrons. Due to the fact that the investigated samples contain three ($SrTiO_3$) or even four ($La_{0.7}X_{0.3}MnO_3$) elements as heavy as Ce (Z = 58), a rather large number of core levels are found in the samples studied here. Each photoemission line brings about a certain amount of secondary electrons, some of which are coherent and thus have a clear anisotropy [**73**]. This creates a very complex background function that could not be modeled in a routine way. Because neither reference from polycrystalline substrate nor use of fitted model functions offered a generally applicable route for data analysis here, we have compared experimental and theoretical ADCs directly by forming intensity ratios I_{exp}/I_{theo} [**74**]. From the polar angle dependence of this intensity ratio a model function has been determined, which takes the different angular dependent intensity behavior between the particular experiment and theory into account. After correction of the experimental data with respect to this effect we have been able to perform direct comparisons of experiment and theory over the full angular range.

4.4.3 XAS normalization

While XPS measurements yield direct information (Intensity in counts per second vs. Energy in eV) and need not be treated further, the detected signal in Total Electron Yield (TEY) X-ray Absorption Spectroscopy (XAS) is a picoampere current that requires manipulation. This drain current is a result of electrons that leave the sample after irradiation with synchrotron radiation and the ensuing cascade processes.

During all measurements at ANKA, the light hits not only the sample but also a gold mesh and a tiny NiO single crystal. The x-ray absorption of these two tools is detected as well. The gold mesh gives the signal I_0, which is crucial for all absorption experiments. It eliminates all fluctuations from the storage ring and the optical devices (mirrors, beamsplitter, monochromator, …) and their possible contaminations.

Because the monochromator gives only relative but not absolute values of the photon energy, the drain current of NiO is detected simultaneously as well. The O K edge of NiO is a sharp peak at 530.8 eV (determined by EELS, e.g. [**75**]) and may be used for energy calibration.

By closing a valve in front of the sample, the dark current of the Keithley picoamperemeter is measured. The final x-ray absorption intensity is the [(drain current) - (dark current)] / I_0. This intensity is then normalized to zero in the region before the edge jump and to unity in the region following the edge jump.

If linearly or circularly polarized light and / or a tilt angle was used, further corrections are of course necessary for quantification. The degree of linear polarization is 95% at ANKA and 90% at ELETTRA, the circular polarized light has a value of 90% at both beamlines. Tilting the sample increases the illuminated area (cosine function) and must be corrected as well.

Out-of-plane and in-plane absorption differs for the L edges of the investigated films, because the electrons are excited into empty d-orbitals with well-defined geometries. The normalized linear dichroic signal introduced in chapter 3.4 is defined as XLD = $2[I_{\text{out-of-plane}} - I_{\text{in-plane}}] / [I_{\text{out-of-plane}} + I_{\text{in-plane}}]$. The nomenclature is such that out-of-plane means that the electric field vector is perpendicular to the surface so that for instance transitions into the $3d_{3z^2-r^2}$ orbital take place.

If the sample is ferromagnetic, a magnetic field is applied and XAS is performed with left or right circularly polarized light, there are differences as well. This x-ray magnetic circular dichroic signal is defined as XMCD = $2[I^+ - I^-] / [I^+ + I^-]$, where I^+ (I^-) is the x-ray absorption intensity for photon helicity parallel (antiparallel) to the magnetization direction.

4.4.4 XMCD sum rules

While the sum $(I^+ + I^-)$ provides electronic information, the difference $(I^+ - I^-)$ is magnetic in origin. Thole and Carra [**76**], [**77**], for L edges see [**78**], [**79**] have developed a set of sum rules that use this fact to determine spin and orbital moments from XAS data.

After the XAS data manipulation mentioned in 4.4.3, the sum and the difference of two data sets with different helicity or magnetization direction are calculated.

Then a double step function must be found that describes the transitions of electrons into the continuum. Typically a rather simple background function is sufficient, having a step height of $^2/_3$ at the L_3 edge, an additional $^1/_3$ at the L_2 edge (ideal branching ratio) and a step width of approximately 1 eV. The necessary integrals are shown in figures 4-1 and 4-2.

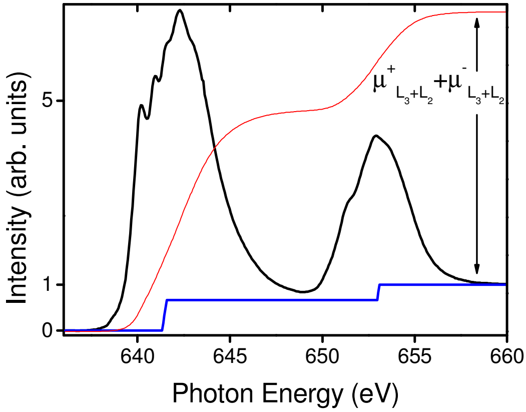

Figure 4-1: Example of the Mn $L_{2,3}$ edge (black), a simple step function (blue) and the integral area (red) of the difference edge - step function.

Here the integral area (red line) between the XA intensity (black line) and the step-function (blue line) is proportional to the number of unoccupied Mn3d states. The XA intensity is the average of the two helicities.

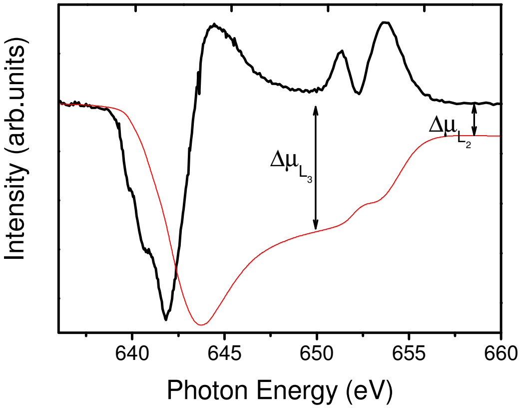

Figure 4-2: **Example of a typical Mn XMCD signal (black) with the integral over the dichroic signal (red) at the L_3 (up to 650 eV) and the L_2 edge (650 eV and above).**

The difference between the two helicities is shown in figure 4-2 (black curve). Here the integral area is separated into two regions for the two parts of the Mn L absorption edge.

The final step is to calculate the integral values and use these in the sum rules for orbital μ_l and spin μ_s moment:

$$\mu_l^{3d} = -\frac{2n_h}{N}\int\left(\Delta\mu_{L_3} + \Delta\mu_{L_2}\right)dE$$

$$\mu_s^{3d} = -\frac{3n_h}{N}\int\left(\Delta\mu_{L_3} - 2\Delta\mu_{L_2}\right)dE$$

$$\text{mit } N = \tfrac{3}{2}\int\left(\mu^{+}_{L_3+L_2} + \mu^{-}_{L_3+L_2}\right)dE$$

n_h is the number of 3d holes or (10-n_{3d}), the 3d electron count. For electron doped manganites, the (theoretical) Mn 3d electron count is 4.3, for hole-doped manganites it is 3.7.

4.5 Parameters of EDAC calculations

4.5.1 Initial Guess

To simulate multiple scattering effects, the cluster model approach of the EDAC code was used, [**14**], which is based on the muffin-tin potential approximation. The atomic positions in the cluster are bulk-like, i.e. alternating slabs of SrO and TiO_2 layers form cubic unit cells with lattice parameters a = b = c = 0.3905 nm. As a starting point, the following input file was used:

```
1       initial state 3d
2       emitters 1 l(A)    0    0    0    0
3       beta 55
4       emission energy E(eV) 1120 1120 1
5       emission angle theta -10 80 91
6       emission angle phi 0 360 361
7       V0 E(eV) 10.5
8       cluster surface l(A) 2.3
9       imfp inline 1 l(A) 22
10      lmax 15
11      orders 3 1 3 5
12      temperature 300 693
```

After the definition of the atom types and positions in the cluster, as well as the cluster size, above-mentioned parameters determine:

The intitial state for photoemission (line 1), the position of the emitter (line 2), the angle between x-ray source and analyzer (line 3), the Sr3d kinetic energy (line 4), the emission angles θ (line 5) and ϕ (line 6), the muffin-tin zero (line 7), the surface step height (line 8), the inelastic mean free path of Sr3d photoelectrons in $SrTiO_3$ at 1120 eV (line 9), the maximum angular momentum used in the development of the multiple scattering series (line 10), the iteration (scattering) order (line 11) and the experiment and Debye temperature in line 12.

Parameters V_0 and “cluster surface” are suggestions by Garcia de Abajo, the Debye temperature of STO is 693 K [**80**]. The other parameters are expected to have an effect on the result of the scattering cluster calculations. These starting values were then varied systematically to identify their influence.

4.5.2 Influence of the cluster size

The first parameter to be varied is the cluster size. The number of atoms in the hemispherical cluster (figure 4-3) is determined by a radius around a central atom at the surface.

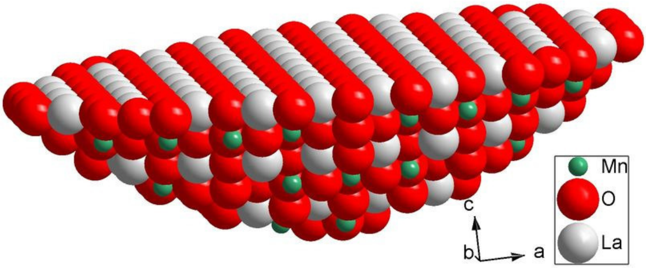

Figure 4-3: **Example of a typical EDAC hemispherical cluster with a maximum depth of three unit cells and containing 614 atoms.**

It is expected that too small clusters may influence the scattering calculations in the way that convergence is not reached if atoms on the edge of the cluster are included. Like the surface the edge of the cluster is a region of reduced symmetry because edge atoms are not surrounded by other atoms on all sides but are adjacent to vacuum. These atoms have thus different and - physically non-realistic - muffin-tin potentials whose inclusion in the scattering calculation leads to difficulties.

To estimate the cluster size, de Abajo suggests $N \approx (1.5\ \lambda)^3$, i.e. all atoms within a (half) sphere of radius 1.5 times the IMFP. For the case of Sr3d with an IMFP of 21.5 Å (TPP-2M calculations, see 4.6.1.1 for more details) this means a half sphere with a radius of 32 Å comprising more than 2000 atoms. For this set of test scans the cluster size was varied in the following steps, 10, 15, 20 and 25 Å, which results in clusters with 90, 270, 603 and 1168 atoms. Results of test calculations are shown in figure 4-4.

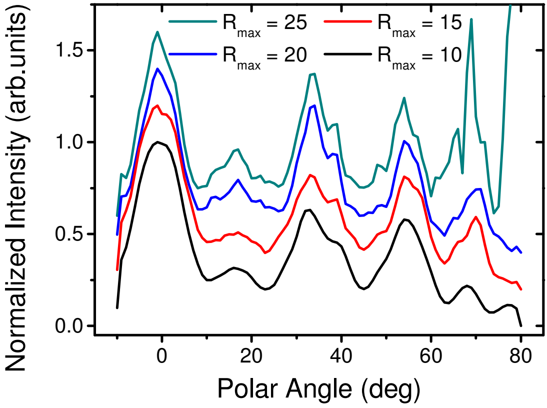

Figure **4-4**: **Evolution of a Sr3d-[110] test scan with increasing cluster size from 90 (black) to 1168 (green) atoms.**

The figure shows the evolution of the Sr3d polar scans in the [110] direction with increasing R_{max}. Looking at the red and black lines one can see that especially at higher angles there is more intensity for the bigger cluster because for R_{max} = 10 no shallow scatterers at these angles are present. New structures arise at low angles with an even bigger cluster (blue) and fine structures change. With increasing cluster size big spikes are found in the polar scans at angles of 60° and above. This is an indication for numerical problems in the scattering calculations if too many scatterers are involved: Many low intensity values (that should be regarded as zero) at high angles add up during multiple scattering with every additional iteration step and eventually dominate the polar scan. Since additional cluster atoms are responsible for these glitches and prolong the calculations, the search for the optimal number of atoms is of great importance. A compromise must be made between the suggested cluster size (1.5 λ) and the maximum cluster size for which convergence is still reached.

4.5.3 Influence of the angular momentum

The next parameter, that was varied, is l_{max}, i.e. the maximum angular momentum for which the scattering phase shifts take non-negligible values. The maximum angular momentum is approximated as $l_{max} \approx k\, r_{MT}$. Here, the muffin-tin radius r_{MT} is in turn approximated by the ion radius and k is the wave vector of the electron. For emission from the Sr 3d level (1120 eV, 1.4 Å) we get a value of $l_{max} \approx 25$. It was varied between 10 and 25 in steps of 5. Results of test calculations are presented in figure 4-5.

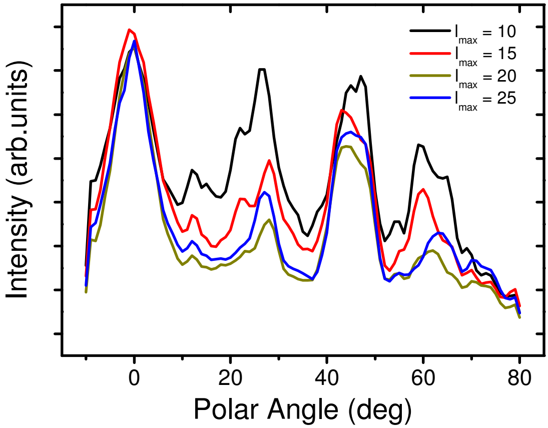

Figure 4-5: **Evolution of a Sr3d-[100] testscan with increasing l_{max} from 10 (black) to 25 (blue).**

With increasing accuracy of the outgoing wave, the polar scan of Sr3d-[100] changes drastically. Most of the changes concern the intensity rather than the position of the peaks. For example at polar angles of 27° and 60° the intensity decreases from l_{max} = 10 to l_{max} = 20 but then increases again for l_{max} = 25. The same goes for the main peak at around 45°. It becomes obvious that convergence is absolutely necessary for reliable data. For both too small and too large values of l_{max}, the calculations do not converge. There is a small optimum that must be found for each set of cluster size and atom type, kinetic energy and emitter position.

Apart from these obviously important parameters, two others were varied systematically, scattering order and inelastic mean free path. Further parameters were the iteration method and the number and the positions of the emitters. They will be explained in the following segments.

4.6 Influence of other parameters

4.6.1.1 IMFP

The inelastic mean free path of the emitted photoelectron influences the necessary size of the cluster and the number of scattering events that need to be taken into account. If the IMFP is large an electron travels longer distances before being inelastically scattered. Elastic scattering at farther away neighbors becomes more and more important and multiple scattering occurs. Varying the IMFP between 0.1 and 0.3 nm in steps of 0.1 nm and calculating Sr3d polar scans, the following trend is found (figure 4-6):

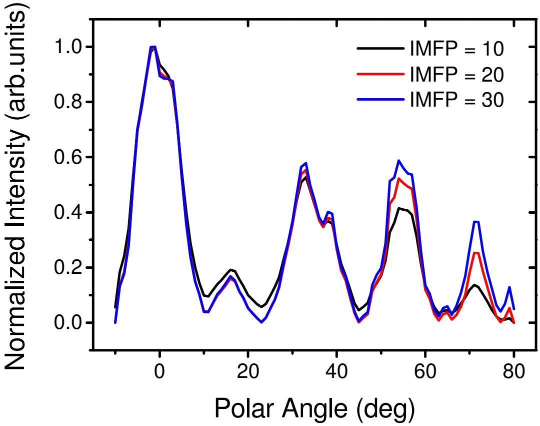

Figure 4-6: **Evolution of a Sr3d-[110] testscan for inelastic mean free path lengths of 10 (black), 20 (red) and 30 Å (blue).**

The influence of the increasing path length concerns the intensity mainly, no additional structures appear. This result is somewhat unexpected, because features from deep layers (at low polar angles) or scattering at far away (shallow) atoms (at high polar angles) are expected to show up when the IMFP increases. On the other hand, most of the scattering happens at nearest neighbor atoms, no further than two to three unit cells away from the emitter. Consequently, the IMFP merely changes the intensity of the scan with small effects on relative intensities of the various peaks.

Up to the [112] peak at 33°, there is almost no change in the ADCs in figure 4-6. At 54°, the [111] peak shows a 26% increase going from 10 to 20 Å and an additional 12% increase for IMFP = 30 Å. At 71°, this effect is even more pronounced, yielding 85% more intensity between IMFP = 10 Å and IMFP = 20 Å and 45% for the step from 0.2 nm to 0.3 nm. These differences are, however, not a cause for concern if the IMFP is chosen well and physically meaningful. Calculations for $SrTiO_3$ using the Tanuma-Powell-Penn equation (TPP-2M, figure 4-7, [**81**] and references therein) give values of 15, 16 and 21 Å for oxygen (1s), titanium (2p) and strontium (3d) photoelectrons. Necessary input for the TPP-2M equation is the band gap energy in eV (3.2), the number of valence electrons (24) and the density (5.12 gm/cm^3).

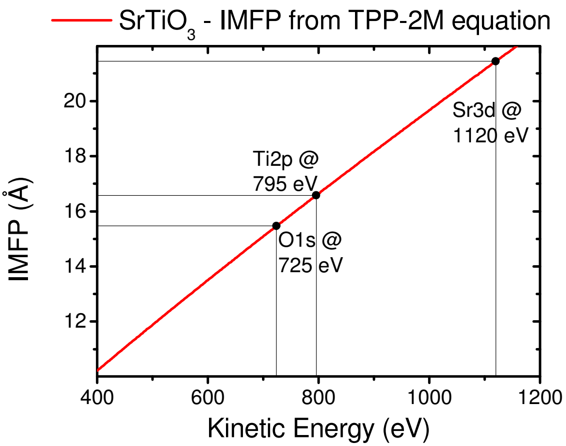

Figure 4-7: **IMFP calculated using the TPP-2M formula for photoelectrons with a kinetic energy of 725 eV (O1s), 795 eV (Ti2p) and 1120 eV (Sr3d) in a $SrTiO_3$ crystal.**

4.6.1.2 Iteration Method

The direct inversion of the MS matrix is possible only for small numbers of atoms and small values of l_{max} because $N^3(l_{max}+1)^6$ products have to be calculated. Three other solutions are however available in EDAC, the simultaneous relaxation (SR) method, the direct Jacobi iteration and the modified recursion method. Since the SR method requires yet another parameter (the so-called relaxation parameter η, which mixes results from consecutive iteration cycles to accelerate convergence) this method was not used here.

The Jacobi method is the default method in EDAC, the fastest algorithm and it allows calculating single-scattering. However, several problems arose and the modified recursion method was applied in most calculations in this work.

Both Jacobi and recursion initially give the same results. The [100] direction of a Sr3d testscan in both iteration methods is identical. In the [110] direction (figure 4-8), however, a feature at 13° brought the decision in favor of the modified recursion method.

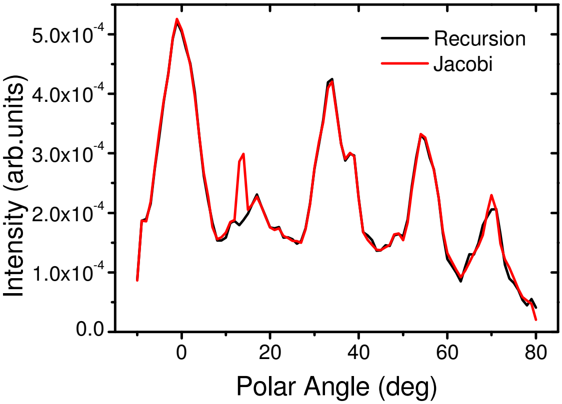

Figure 4-8: **Testscan of Sr3d-[110] comparing the iteration methods „modified recursion“ (black) and “direct Jacobi iteration” (red).**

Here a spike is found in the Jacobi calculation which is not a single data point glitch. Such a feature is difficult to identify because it looks like a real peak. It is not one single data point that is off the curve by a large difference, but rather a small peak that could well be misinterpreted. Further test calculations showed that especially for heavier atoms and dense lattices the direct Jacobi iteration seems to converge less reliably than the modified recursion method. The EDAC approach is most reliable for systems with strong forward scattering and little interference effects (C. Langheinrich, personal communication). All relevant calculations in chapter 5 were thus performed using the modified recursion approach.

4.6.1.3 Choice of Emitters

The number (and position) of emitters is an important factor that determines the shape of the calculated polar scans. As a starting point, one single Sr emitter in the uppermost layer is selected. This gives no structure because there are no scatterers above the emitter and backscattering is negligible.

For an emitter in a deeper layer, i.e. 1 unit cell below the surface, a lot more features are found. The main peaks at 0°, 45° and 63° in the [100] azimuth come from the first expected scattering directions, corresponding to neighboring atoms in the [001], [101] and [201] directions.

The first expected scattering directions in the [110] direction for a Sr emitter are along [001], [112], [111], [312] and [211], or 0°, 35°, 55°, 65° and 71°. All of them are found in the ADC.

For even deeper emitters and for both azimuths, big changes are found in the low to medium polar angle range (10° - 25°). Here, scattering at atoms is found that are several layers above the emitter. Combining these scans, one can study the contributions from the individual layers. This is possible because the overall intensity is comprised of many scattering paths that do not interfere with each other. The interference between the primary wave and the scattered wave coming from a given emitter is a coherent process, whereas the total intensity arriving at the detector is the sum of all photoelectrons emitted from the sample for a given solid angle.

Results are shown in figure 4-9. From bottom to top, emission from SrO layer 1 (at the surface, brown), layer 3 (1 unit cell below the surface, green) and layer 5 (2 unit cells below the surface, blue) is shown. Layers 2 and 4 are TiO_2-layers and do not contain Sr atoms. The average of these three curves is plotted in red and may be compared to a calculation with three emitters (black curve) at once. The red and black lines are offset for comparison but otherwise identical.

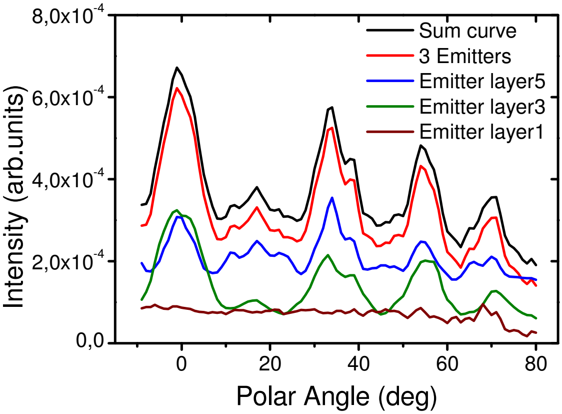

Figure 4-9: **Plot of emission from single emitters in different depths, (brown, green and blue), their average (red) and a calculation with three emitters (black).**

This allows determining the contributions of single emitters in different positions or depths to the overall intensity. In this way it is possible to correlate many structures in the polar scans with actual atomic positions and types of scatterers. Only then is it possible to determine structural properties from measured data, such as sample termination or lattice distortions.

Additional benefits include the possibility to perform calculations on many computers in parallel and the possibility to identify and treat non-converging emitters alone without having to discard the entire multiple scattering cluster calculation. The computation time is roughly cumulative as well, Sr in layer 1 (34 min), Sr in layer 3 (34 min) and Sr in layer 4 (32 min) are comparable to a calculation with two (67 min) or three emitters (96 min). The only remaining point that needs to be examined is, whether or not the results are identical for equivalent atoms at different positions.

4.6.1.4 Central Atom

For any given cluster, there will always be atoms that are located at or exactly below the so-called cluster reference point. This point is the center of the cluster and determines the dimensions in all three directions via the parameter R_{max} as mentioned above. Thus, a Sr atom at the position (0, 0, 0) leads to four surrounding O atoms at (±½, ±½, 0), which have an identical environment. Of course this is true only in the first approximation because for example the atom at (+½, +½, 0) is $a\sqrt{2}$ unit cells closer to the upper right corner of the cluster than the atom at (-½, -½, 0) and vice versa. For big clusters, the ensuing asymmetry is however negligible.

Looking at the strontium titanate unit cell, one finds three inequivalent lattice sites, labeled Sr (0, 0), Ti (±½, ±½) and O (±½, 0) and (0, ±½). In the following these clusters will be labeled Sr-centered, Ti-centered and O-centered. Figure 4-10 shows the AO (SrO) layer of STO with the central atoms highlighted by circles.

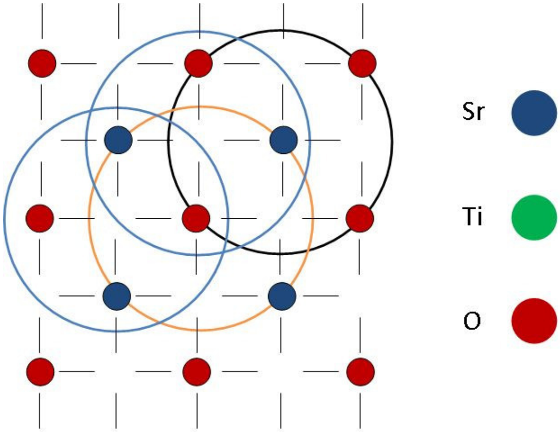

Figure 4-10: **The AO layer of STO showing different centerings in black around (0,0) (Sr, blue dots), in blue around (±½, ±½) (where Ti is found in the BO_2 layer) and in orange around O ((±½, 0) red dots)**

The original cluster was shifted by the vectors (½, 0) and (½, ½) to yield the inequivalent centerings. From figure 4-10 it is easy to see that not all centerings lead to fourfold symmetric results. This must be kept in mind when analyzing the calculated data.

The atoms were labeled as follows. O_{xy} is the oxygen atom y in the layer x. The layers are labeled from the surface to the bottom of the cluster, i.e. layer 1 is the uppermost, terminating SrO-layer, followed by layer 2, TiO_2, and so on.

The atom position are labeled from 0 to 4, where 0 stands for the central atom at (0, 0) and the atoms 1 to 4 are either at the corners or on the edges. Atom 1 corresponds to either the (½, ½) or the (½, 0) site, atom 2 is found at (½, -½) or (0, -½), the numbering goes on clockwise.

Thus, the following atoms have to be compared for e.g. layer 3, the second SrO layer from top at a depth of one unit cell.

Sr-centered	Oxygen atoms $O_{31}/O_{32}/O_{33}/O_{34}$ at (±½,±½, -1),
Ti-centered	Oxygen atom O_{30} at (0, 0, -1) and
O-centered	Oxygen atoms O_{31}/O_{33} at (±½, 0, -1).

The resulting polar scans are shown in figure 4-11. All seven polar scans should be identical, which they are, except for the obvious spike at 45°. The center point of the cluster does not affect the outcome of multiple scattering cluster calculations.

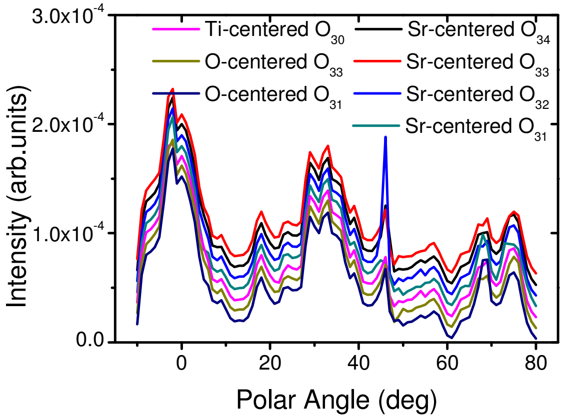

Figure 4-11: **Comparison of seven polar scans from three differently centered clusters. There are 4 inequivalent O-sites for Sr-centering, one O-site for the Ti-centering and 2 inequivalent O-sites in the O-centered configuration. All calculated polar scans are comparable except for an obvious spike at 45°.**

The spike is only a minor cause for concern (although it is not fully understood) because calculated data was always averaged over all available equivalent emitters. While calculations for Sr-centered O_{32} and O_{34} overestimate the intensity at 45°, the intensity is underestimated in the scans from Sr-centered O_{31} and O_{33}. After averaging the four curves, the curve shape is almost identical to the other centerings.

4.6.1.5 Iteration Steps (Recursion)

Having determined several disadvantages of the standard direct Jacobi iteration, the modified recursion method was applied to all further EDAC calculations presented in this work. This method does not allow computing single scattering (first order), in fact here the precision of the results indeed converges with growing number of iteration steps. Convergence is reached for an order of 10 for the testscans. For the final calculations, including the optimized parameters according to this chapter, the order 20 was chosen for $SrTiO_3$.

To conclude this chapter, several parameters were analyzed with respect to their influence on the outcome of multiple scattering cluster calculations using the EDAC code. Test calculations showed how l_{max}, the number of iteration steps or the cluster size changed the diffraction pattern. It is demanding but necessary to find an optimal set of parameters for each calculation. Some compromises between precision and stability have to be made because higher values for l_{max} or R_{max} do not always lead to better results [**82**]). The most important finding is that the recursion method has to be used for the system at hand, which requires rather large cluster sizes and high values of l_{max}, the maximum number of angular moments used in the description of the outgoing scattered photoelectron wave.

Using optimized parameters, the computation times on a standard office computer (Intel Pentium Dual Core E2200 processor running at 2.2 GHz, 2 GB memory) were: 60 hours for O1s, 168 hours for Ti2p and 752 hours for Sr3d, which means a total of 41 days for the bulk STO cluster. Since the calculations are the sum of 68 individual emitters, a convenient parallelization is possible.

4.7 Intensity ratio procedure

As mentioned in chapter 4.4.2, χ-functions were not used in this work but rather an intensity ratio procedure to give better comparability between experiment and simulation. This is necessary because no physically meaningful I_0 curve could be determined that could be applied to the polar scans (see chapter 4.4.2 for details).

The performed steps for the treatment of raw XPD data are described here. After normalization of experimental data to zero and unity they are shifted, if necessary, to correct misalignment. Calculated polar scans are smoothed (5 point adjacent averaging) to broaden the angular resolution to ±0.5° and normalized to values between 0 and 1 as well.

In the next step, the simulated data is shifted and rescaled to match the experimental data, putting special attention to low and medium polar angles. The intensity I becomes I·p+(1-p).

The intensity-ratio is calculated, I_{exp} / I_{theo} and fitted by a Boltzmann curve $\left(y = \frac{A_1 - A_2}{1 + e^{x - x_0/dx}} + A_2\right)$ to yield a sigmoidal correction curve that is comparable to the apparative function.

Finally, the experimental curve is divided by this I_0 curve or the anisotropy is calculated for determination of R-factors.

5 STO

Preparation and investigation of A- and B-site terminated $SrTiO_3$

5.1 Motivation

Over the last two decades, $SrTiO_3$ has become a readily available substrate for the growth of superconducting cuprates [**63**] and manganites [**62**]. It also received considerable attention when a 2D electron gas was observed at its interface to $LaAlO_3$ [**83**]: Heterostructures of these two wide bandgap insulators (3.2 and 5.6 eV, respectively) exhibit electronic conduction at the interface, ferromagnetism and superconductivity [**84**], [**85**].

The STO unit cell can be described as alternating layers of charge neutral sheets of basic SrO and acidic TiO_2. There are thus two possible terminations, which influence growth behavior and microstructure of overlayers. The stacking sequence of interfaces is influenced as well, i.e. only if the STO substrate is terminated by a TiO_2 layer there is electronic conductivity at the interface to LAO.

The growth of the superconducting cuprates on top of strontium titanate on the other hand requires a SrO termination for monolayers [**86**]. Only then can the correct stoichiometry be maintained. On a TiO_2-terminated surface YBa_2Cu_2O and CuO_x form, which leads to precipitation of copper oxide.

The very complex nature of cuprate growth on STO involves perovskite-like nuclei ($BaCuO_2$, $YCuO_2$) that grow in a step-flow mode before changing to layer by layer growth of complete unit cells. While the exact stacking sequence (absence / presence of CuO chain layers, doubling of $BaCuO_2$ units at the interface to the substrate, etc.) depends delicately on growth conditions, what can be said for sure is that growth starts and ends with a BaO layer because it has by far the lowest surface energy. Excess copper oxide precipitates forms planar and / or point defects during growth. These defects facilitate the relaxation of the strain imposed by the substrate on the YBCO film within the first few unit cells [**87**], [**88**], [**89**], [**90**], [**91**], [**92**].

While as-grown single crystals of STO usually exhibit a mixture of both terminations, techniques have been established to obtain smooth single-terminated surfaces [**93**], [**68**].

In the underlying work, both terminations were successfully prepared and studied by means of XPS and XPD. The results presented in this chapter have been published in [**74**] and are reproduced with kind permission of the American Institute of Physics (©2012).

5.2 XPS results

Four samples were investigated, two of them having been treated outside the UHV chamber (ex situ) and two samples that received further surface preparation steps after transfer into the analysis chamber (in situ).

Samples “as received” (pristine) and “BHF etched” (dipped in buffered HF solution and annealed in air) were measured directly after transfer. Samples “Ar^+ etched” and “oxygen annealed” were sputter cleaned with Argon ions, the latter sample was additionally heated in an oxygen atmosphere. Typical XP spectra are presented in figure 5-1.

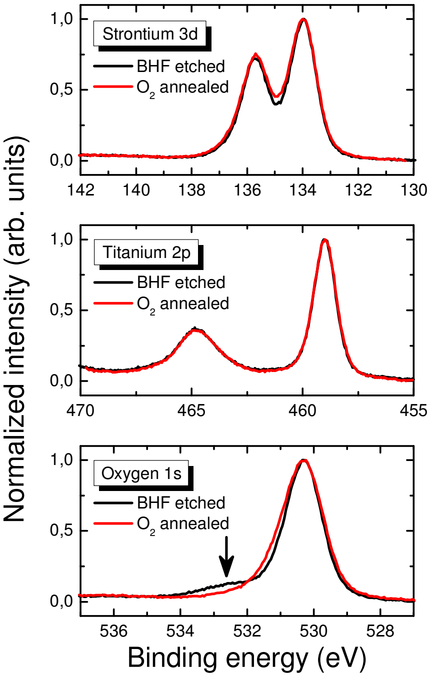

Figure 5-1: XPS detail scans of the Sr3d (top), the Ti2p (middle) and the O1s (bottom) region of $SrTiO_3$ for an ex situ treated sample (BHF etched, black lines) and an in situ prepared sample (O_2 annealed, red curves).

Photoelectron spectra of the Sr3d (binding energy 134.0 eV), Ti2p (459.0 eV), O1s (530.3 eV) and C1s (284.6 eV) core levels were measured to confirm the chemical state of the elements as well as the stoichiometry of the sample and the cleanliness of its surface. The stoichiometry of all samples is very close to the ideal 1:1:3 ratio with slightly enhanced amounts of Sr. A look at the polar scans in chapter 1 shows that the forwards scattering direction around $\theta = 0°$ is more prominent in Sr compared to Ti. We thus describe this small off-stoichiometry to a diffraction effect and the finite angular resolution of the analyzer.

No bulk contaminations were found, the surface of the BHF etched sample was however contaminated with tiny remnants of SrF_2 (about 0.25%) as a result of dipping the sample in buffered hydrofluoric acid [**94**]. Furthermore, water is adsorbed on the ex situ samples due to their contact with ambient air. This is found in the shoulder at 532.5 eV in the lower graph of figure 5-1 (marked by an arrow). Decreasing the information depth by tilting the sample with respect to the analyzer results in an increase of this shoulder. This hints at a surface related species.

Small amounts of carbon containing contaminations are also found on ex situ samples but we can basically rule out the presence of $SrCO_3$ because the C1s and Sr3d emission lines can be described by a singlet and a doublet, respectively. Amorphous hydrocarbons, adsorbed CO or dust do not affect photoelectron diffraction experiments.

It should finally be noted, that the ex-situ samples show a concerted shift of all core level positions by almost +2 eV towards higher binding energies. In the figure this shift was removed to facilitate comparability. It is attributed to charging effects. The absence of charging for the in situ samples indicate the presence of defects which leads to increased conductivity and reduced charging.

Oxygen vacancies are the most common defects at transition metal oxide surfaces [**95**]. $SrTiO_3$ becomes conducting upon reduction [**96**], even metallic with very low carrier concentrations ($n \approx 10^{18}$ [**97**]). The redistribution of the two electrons on neighboring Ti sites leads to the formation of Ti^{3+} ions according to ${}^{+II}Sr^{+IV}Ti_{1-2}x^{+III}Ti_{2x}{}^{-II}O_{3-x}$ [**98**]. However, no significant amounts of Ti^{3+}, which would appear as a shoulder on the low binding energy side of the $Ti2p_{3/2}$ line, could be found in the spectra. Within the sensitivity of XPS, no significant oxygen depletion could be found either.

5.3 XPD results

This chapter presents the XPD results of the four differently prepared STO samples, starting with emission from the Sr3d core level at 1120 eV along the [100] azimuth in figure 5-2.

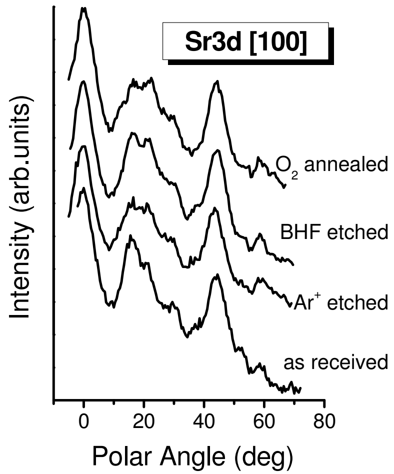

Figure 5-2: Comparison of XPD polar scans of Sr3d along the [100] azimuth for all samples investigated.

The experimental ADCs exhibit significant diffraction structures indicating well-ordered near surface regions of all the samples. The scans look very similar at first glance but also reveal differences in the fine structures. It is well-known that electron forward scattering (fs) has strong effect on the formation of peaks in XPD in particular for electron energies exceeding about 500 eV, and a number of experimental results could be successfully explained on the basis of forward scattering and single scattering calculations [**99**], [**100**], [**101**].

There are two possible cuts through the perovskite unit cell in the [100]-direction and two in the [110]-direction. Figure 5-3 shows one of each set as an example for forward scattering angles. Also, since the surface termination changes the unit cell, the left side ([100]) shows a TiO_2-terminated crystal, while the right side ([110]) shows a SrO-terminated sample. Finally, the left hand side shows the expected angles for emission from a Ti atom (green) with scattering at oxygen (red) in the [102] direction and at titanium in the [101] direction, while the right hand side shows Sr emission (blue).

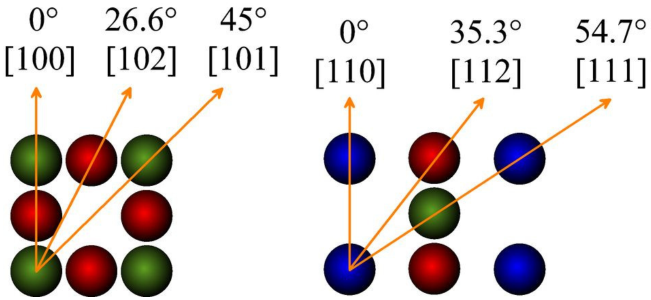

Figure5-3: Two projections of atoms positions in a cubic perovskite unit cell. The left picture shows one of the two possible cuts through the STO crystal along the [100] azimuth (face) for a TiO_2-terminated sample together with some important emission angles. The right picture shows one of the two possible cuts through STO along the [110] azimuth (diagonal) for a SrO-terminated surface together with some important emission angles.

These two sketches are typical of the cubic perovskite lattice, because they can be translated into others by a change of origin. In case of bulk STO(001) as for other cubic systems we expect strong forward scattering enhancements e.g. along [100] (θ=0°), [102] (θ =27°) and [101] (θ =45°) for the [100] azimuth. In fact, a very strong intensity enhancement at normal emission (θ =0°) can be observed in all ADCs. A prominent peak is also observed in Sr3d-[100] near θ =45°.

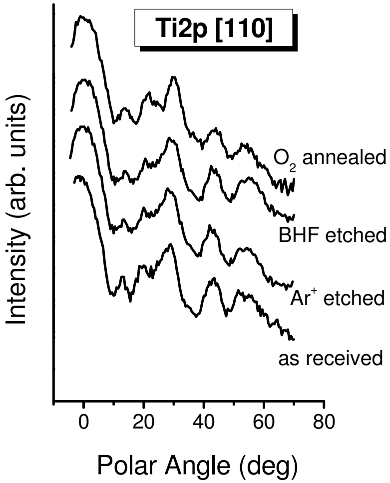

Figure 5-4: Comparison of XPD polar scans of Ti2p along the [110] azimuth for all samples investigated.

Table 5-1 shows an overview of the expected forward scattering angles for Sr3d along the two low-index azimuths. Nearest neighbor atoms are found at angles of 45° and 55° for the two azimuths. Second nearest neighbors are found at 0° in both cases and so on. Similar scattering angles are also expected for Ti and O. The polar scans of Ti2p along the [110] azimuth in figure 5-4 are expected to, in a forward scattering picture, show similarly enhanced intensities along the [111] direction at $\theta = 54.7°$ and the [112] direction at $\theta = 35.3°$. Neither of these peaks are however found in the experimental data.

Neighbor	Sr3d-[100]	direction	Angle (deg)
1st	O	101	45
2nd	Sr	100	0
3rd	Sr	101	45
4th	O	103	18
5th	Sr	100	0
6th	O	101	45
7th	Sr/Sr	102/201	27/63
8th	O	105	11
9th	Sr	101	45
10th	O/O	305/503	31/59
11th	Sr	100	0
Neighbor	**Sr3d-[110]**	**direction**	**Angle (deg)**
1st	Ti	111	55
2nd	Sr	110	0
3rd	O	112	35
4th	Ti	113	25
5th	Sr	111	55
6th	Sr	110	0
7th	O	114	20
8th	O	312	65
9th	Sr	112	35
10th	Ti/Ti	115/111	16/55
11th	O	314	47
12th	Sr	211	71
13th	Sr	110	0

Table 5-1: Forward scattering pathways of Sr3d photoelectrons.

Thus, while being useful for a first interpretation of major structures, the forward scattering picture breaks down when a quantitative understanding of the ADCs is desired. Therefore, full multiple-scattering calculations are needed to permit an interpretation of the experimental XPD data from STO.

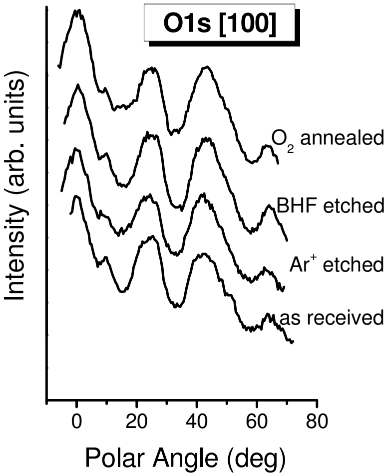

Figure 5-5: Comparison of XPD polar scans of O1s along the [100] azimuth for all samples investigated.

Just like the Ti2p ADCs, the O1s scans in figure 5-5 only exhibit minor differences for the various treatments, slight changes in the peak shapes at 24° and 42° are found. The Sr3d ADCs along the [100] azimuth show recognizably different fine structure patterns between about θ=10° and θ=35°. Interestingly, diffraction features in this angular region should derive from scattering of photoelectrons which originate from emitters more deeply buried in layers below the surface at atoms at the surface.

However, the experiments need to be analyzed by comparing them to multiple scattering calculations directly to come closer to an understanding of the surface of interest. Therefore, procedures have to be developed in particular to handle the problem with the angular dependence of background intensities, in order to permit this comparison on a quantitative level. The intensity ratio procedure described above accounts for this problem in an adequate manner.

5.4 EDAC results

Multiple scattering cluster calculations were first performed using the free code from Garcia de Abajo, van Hove and Fadley. Their electron diffraction in atomic clusters or EDAC code was described in chapter 3.5, calculation parameters are found in chapter 4.5. It was previously successfully employed for instance in the study of RhO on a Rh(100) single crystal [**102**], the c(4x2) reconstruction of 3C-SiC(001) [**103**] or on $PbTiO_3$ [**100**]. Results of calculations on the $SrTiO_3$ cluster are presented in figures 5-6, 5-7 and 5-8.

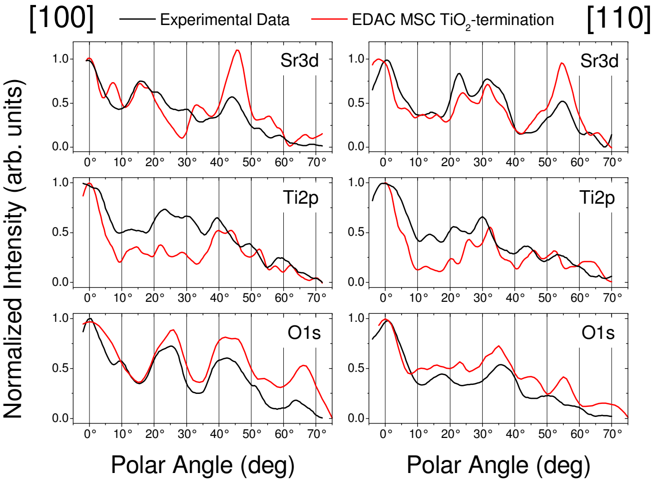

Figure 5-6: Comparison of experimental XPD polar scans for sample „as received“ and results of EDAC MSC calculations for photoelectron diffraction of Sr3d, Ti2p and O1s (from top to bottom) core levels from a TiO_2-terminated STO cluster in the [100]- (left) and the [110]-direction.

The first graph compares experimental XPD results of pristine STO ("as received") to EDAC multiple scattering cluster calculations for a TiO_2-terminated sample. Starting with the Sr3d core level in the top row, agreement is reasonable for the [100] azimuth and good for the [110] direction. The same goes for Ti2p in the middle row, while for O1s the [100] direction gives really good agreement between experiment and theory while the other main crystallographic axis shows worse overlap. It must be noted, that the same cluster is used for all calculations and convergence was also reached in all cases. The varying quality of agreement can thus not be explained by differences in the input files. These differences are rather a true result and require an explanation.

For calculation of the SrO-terminated sample surface, the uppermost TiO_2 layer of the cluster is simply switched off. No other changes were made, to minimize errors. A similar comparison between experiment (STO "as received") and MSC simulation is presented in figure 5-7. It shows the same trends as for the TiO_2-termination. The agreement between experiment and simulation is reasonable also for this termination.

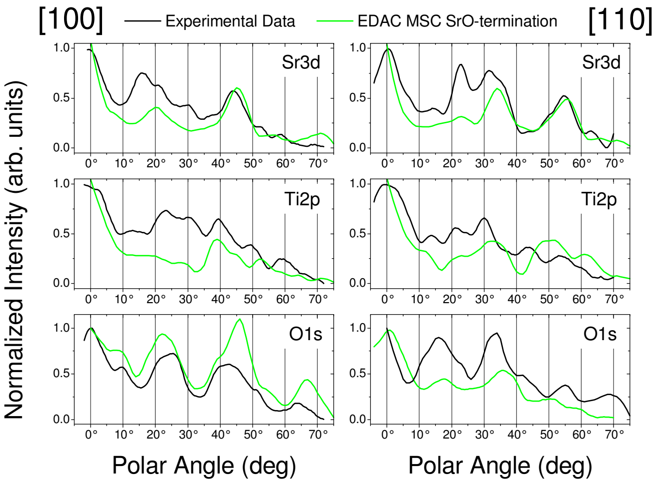

Figure 5-7: Comparison of experimental XPD polar scans for sample „as received" and results of EDAC MSC calculations for photoelectron diffraction of Sr3d, Ti2p and O1s (from top to bottom) core levels from a SrO-terminated STO cluster in the [100]- (left) and the [110]-direction.

It is striking that the calculated polar scans for the two different terminations differ strongly in direct comparison (see figure 5-8). If this was also the case in the experiment, it would be easy to determine the terminating layer of strontium titanate.

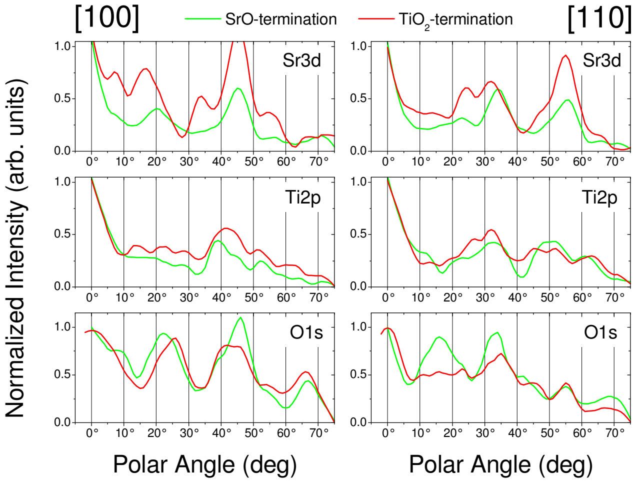

Figure 5-8: Comparison of calculated EDAC results for the two possible sample (SrO green and TiO_2 red) terminations of STO along the [100]- and the [110]-direction.

Especially the Sr3d polar scans should be helpful in this case: Along the [100] azimuth the emphasis in the region between 10° and 30° lies at 15° for a TiO_2-terminated sample and at 20° for a SrO-terminated sample. Along the [110] azimuth, the absence (presence) of the peak at 22° is a good indication for the SrO- (TiO_2-) termination.

The Ti2p polar scans are rather similar and less useful for the determination of the top sample layer. Finally the O1s-[100] scans show different peak positions (between 22° and 26°) and peak shapes (between 40° and 50°). The O1s-[110] ADC either has a peak at 16° for SrO-termination or it does not for the TiO_2-termination.

Looking at the abovementioned differences, the agreement between experiment and a TiO_2-termination seem to give a better fit. The experimental weight in Sr3d-[100] is closer to 15°, the Sr3d-[110] scan consists of a double structure at 23° and 32° and the peak shapes and positions of O1s-[100] and –[110] fit better as well. Comparing these findings to the experimental datasets in figure 5-2 suggests that the medium angle region of Sr3d-[100] may be helpful for a termination study of STO because it exhibits differences in experimental as well as in calculated polar scans.

An interesting point is that for Sr3d-[100] (and O1s-[100]) the MSC data does not have its maximum at 0° but at 45°. A look at Table 5-1 shows, that for Sr3d-[100] among the ten-nearest neighbors of a given Sr emitter, there are four atoms along a polar angle of 45° and only two above the emitter at $\theta = 0°$. This holds especially true for a TiO_2-terminated surface, because atom number 11 is located at 0° but is found in an SrO-layer three unit cells above the emitter and thus absent for the BO_2-terminated crystal.

For the 45° peak, one might expect a defocusing effect which would decrease its intensity in favor of the 0° feature. This was described by Tong [**104**] for a linear chain of atoms and is schematically shown in figure 5-9.

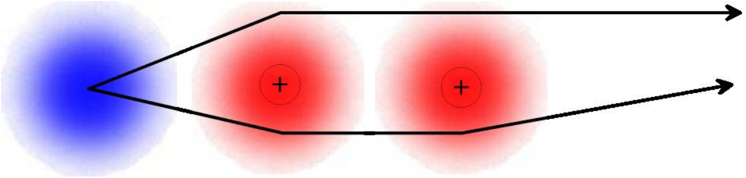

Figure 5-9: Schematic drawing of the defocusing effect in diffraction, blue emitter, first scatterer in the middle, second scatterer on the right. The upper trajectory experiences negligible phase shift from the second scatterer and is forward scattered while the lower trajectory is defocused and decreases forward scattering intensity.

A trajectory which is forward scattered by the nearest neighbor may be scattered out of this direction by a second atom's positively charged nucleus. For even more scatterers in a row, the emitter trajectories are scattered away ever more strongly, as a result the intensity and the width of the forward-scattering peak decrease.

As a summary of this segment, using bulk-like atom positions and parameters that are a compromise between precision and convergence it was possible to simulate the polar scans of Sr3d, Ti2p and O1s of $SrTiO_3$ with the free multiple scattering cluster calculations code EDAC. The agreement between experiment and theory is good and relevant termination-sensitive regions could be identified in the Sr3d polar scans. However, regarding the rather small differences between the datasets for the different preparation conditions and the fact that writing one's own multiple scattering code was beyond the scope of this work, no further conclusions can be made at this point.

5.5 Halle PED MSC code

A collaboration with Christian Langheinrich and Angelika Chassé (Quantum Theory of Solids, Martin-Luther-University Halle-Wittenberg) was consequentially established. Results are presented in this chapter and are compared to experimental data. Further information on their multiple scattering cluster code for photoelectron diffraction is found in [**105**], [**16**], [**106**], [**107**] and in chapter 3.6.

First results are presented in figure 5-10, showing calculations of intensities from the three emitters (O1s, Sr3d, Ti2p from left to right) in the two main directions ([100] left and [110] right) and for the two terminations (SrO green, TiO_2 red).

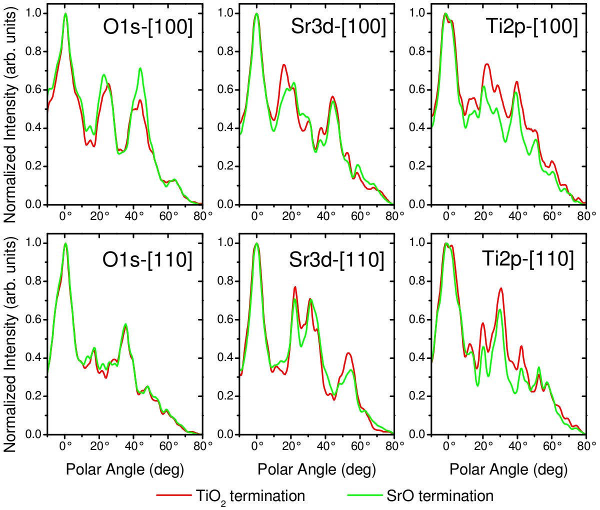

Figure 5-10: Comparison of MSC calculations for the three STO emitters (O1s, Sr3d, Ti2p from left to right) in the two main directions ([100] left and [110] right) and for the two terminations (SrO green, TiO_2 red).

What first catches the eye is how little the scans differ from each other with respect to the sample termination. Oxygen shows the same trends as in the EDAC calculations – different peak positions at about 20° and peak shape at 45° in the [100]-direction, as well as higher intensity at 16° for the SrO-termination along the [110] azimuth.

On the right hand side, the angular resolved titanium photoemission simulation shows similar patterns for the two terminations, both consisting of a number of peaks which seem slightly shifted with respect to each other.

Finally, the Sr3d curves in the center are almost identical along the low-index direction [110] in the lower half for both terminations.

For the purpose of termination detection, the medium angle region of the Sr3d-[100] in the upper middle ADC is interesting. Here, as well as in the experimental data in figure 5-2, the relative intensities change from a left-leaning peak shape in the case of SrO-termination towards a right leaning peak shape in the case of a TiO_2-termination between 10° and 25°. This region is used as a fingerprint region in the following discussion.

5.6 Discussion

The four samples investigated are expected to be TiO_2-terminated (“as received” and “BHF etched”) or SrO-terminated (“Ar^+ etched” and “O_2 annealed”) because of their different surface treatment.

The pristine sample (“as received”) should be TiO_2-terminated according to the supplier and because this is the thermodynamically stable surface layer. The etching procedure with buffered HF (87.5% NH_4F, 12.5 % HF) preferentially removes the SrO-layer (BHF etched).

On the other hand, preferential sputtering of light atoms by Argon ions is typically found as a result of the mass effect described by Holloway (Holloway1979) [**108**]. This would lead to a Ti- ($Z = 22$) and O- ($Z = 8$) depleted surface region, with Sr ($Z = 38$) being left behind (“Ar^+ etched”). The following annealing step in an oxygen atmosphere should recrystallize the surface and ensures the correct stoichiometry ("O_2 annealed").

5.7 XPD of ex situ prepared samples

First, results of ex situ samples are presented in figure 5-11.

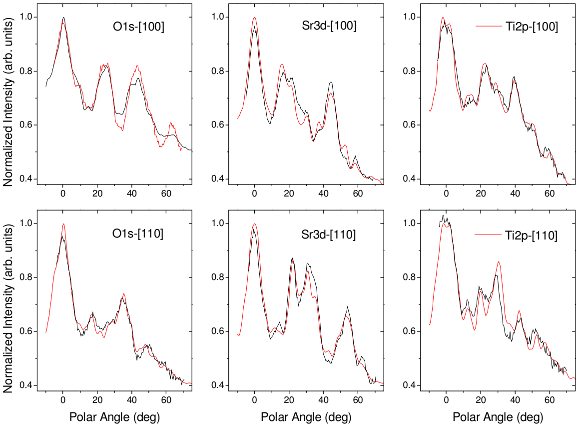

Figure 5-11: Measured XPD polar scans (black curves) of sample "BHF etched" in the [100] (top) and the [110] (bottom) direction. Angular distribution curves are shown for photoelectrons coming from the O1s (left), Sr3d (middle) and Ti2p (right) core level. Results from MSC calculations for a TiO_2-terminated STO sample are shown in red.

Polar scans of the "BHF etched" sample, i.e. the wet-chemically etched STO, along [100] and [110] for each of the three elements are shown in comparison to calculated ADCs of a TiO_2-terminated surface. Applying the intensity ratio correction method on the experimental results allows direct comparison of experimental and simulated data. Atoms are assumed to be located at bulk-like positions in these calculations.

The general shapes of the angular curves, but also the relative intensities of the peaks and even the details of the fine structures are represented very well by the calculations, as can be judged from a first glance. This very good agreement between experiment and theory is observed for both azimuthal directions, which is a strong hint for an essentially TiO_2 -terminated surface in agreement with literature. The calculated R-factors fall between 0.035 and 0.13 for all ADCs. These low R-factors are further indication for the excellent description of the data by the theoretical modeling even without consideration of possible surface relaxation.

Nevertheless, because the differences between the two terminations are so small, low R-factors can also be obtained for SrO termination in the ”BHF-etched” case. Looking at these R-factor values alone is therefore not sufficient at the achieved level of agreement between experiment and theoretical model.

5.8 XPD of in situ prepared samples

First results on in situ prepared samples are presented in figure 5-12.

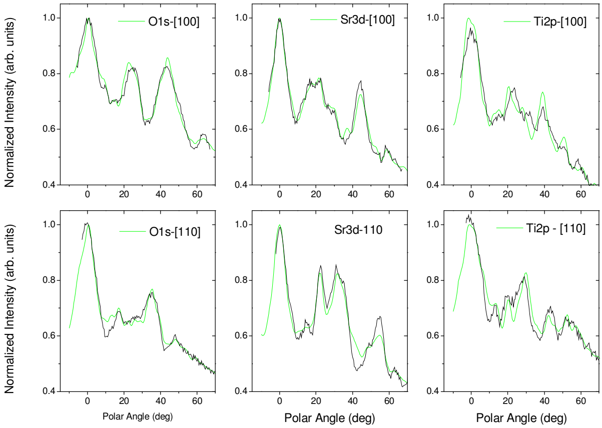

Figure 5-12: Measured XPD polar scans (black curves) of sample "O_2 annealed" in the [100] (top) and the [110] (bottom) direction. Angular distribution curves are shown for photoelectrons coming from the O1s (left), Sr3d (middle) and Ti2p (right) core level. Results from MSC calculations for a SrO-terminated STO sample are shown in red.

The resulting XPD polar scans of a STO(001) surface prepared in the above-described manner are shown in black. The results from MSC simulations for a SrO-terminated STO(001) surface (green lines) are also included in the graphs. Again, ADCs for the two main crystallographic directions of all three elements of STO are presented. The calculated R-factor (0.037) is again very low, indicating a very good agreement between experiment and applied structural model. In general, the agreement between ADCs derived from experiment and theory (for the SrO-terminated surface) is excellent for all displayed graphs in figure 5-12, even fine structures are outlined correctly.

The in-situ prepared STO(001) surface most likely exhibits a SrO-termination. While one cannot rule out completely a partially remaining surface coverage by TiO_2 , the XPD results strongly point to a dominating SrO layer after sputtering and O_2-annealing. The above-mentioned sputtering process evidently removes Ti cations and O anions preferentially. Berlich [**71**] suggested a completely Ti free monolayer at the very surface of the similar ABO_3 compound $BaTiO_3$ on top of 7 oxygen depleted layers after sputtering.

While one could expect significant disorder in these sputtered samples, the sharp diffraction patterns shown in figures 5-2, 5-4 and 5-5 disprove this. Furthermore, no off-stoichiometry and no significant amount of Ti^{3+} (due to oxygen loss) could be found in the XP spectra. The recrystallization step at elevated temperatures in O_2 following the ion bombardment fills possible oxygen vacancies and should smoothen the surface terraces again.

5.9 Preparation conditions and resulting surface termination

This chapter finally presents data of all four samples with special attention paid to the already mentioned fingerprint region between 10° and 25° in the Sr3d-[100] polar scans, displayed and compared in figure 5-13.

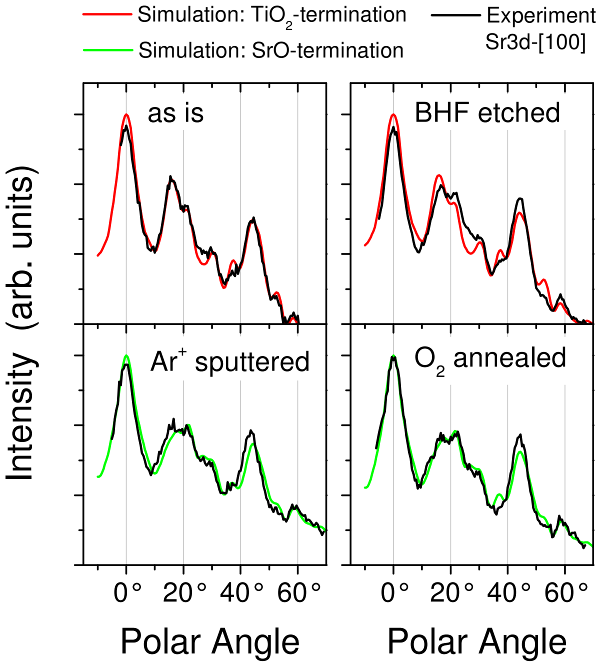

Figure 5-13: Comparison of Sr3d-[100] polar scans (black lines) for all samples and best fitting theoretical results. Agreement between experiment and theory is best for ex-situ prepared samples with TiO2 -termination (red curve, top row) and in-situ prepared samples with SrO-termination (green curve, bottom row).

The top row shows the corresponding ADCs for two samples, which have been surface-treated ex situ, outside the UHV chamber. Both ”as received” and ”BHF etched” polar scans are best described by calculations for a TiO_2–terminated strontium titanate sample, as may be guessed from the very good agreement between experimental (black) and theoretical (red) curves. The bottom row features the respective polar scans for two samples, which were further processed in-situ by sputtering and UHV-annealing (left) and an additional annealing step in an oxygen partial pressure (right). For these two experimental Sr3d-[100] ADCs (black curves) the best agreement is found when compared to calculations for a SrO-terminated surface (green curves), as may again be guessed from looking at the graphs directly.

The best and nearly ”ultimate” agreement seems to be achieved for either ”as received” experimental ADC and a TiO_2 -terminated STO surface, and on the other hand for the ”O_2 annealed” experimental ADC and a SrO-terminated STO surface. That statement is valid regarding the agreement in general but in particular also because of the excellent description of fine structures and relative intensity ratios in the fingerprint region. To the best ability of the present XPD experiments those two samples may be characterized by a TiO_2 and a SrO termination in case of ”as received” and ”O_2 annealed” samples, respectively. The Ar^+-bombarded sample is also well represented by the model of a SrO-terminated STO-surface.

On the other hand, the agreement between experimental ADC for the ”BHF etched” sample and the theoretical modeling is still reasonable but does clearly fit less ideal than for the ”as received” sample. From this comparison a not perfectly TiO_2–terminated surface seems most likely. While the assumption of ideal TiO_2-termination of STO following BHF etching is typically adopted due to earlier evidence from ion scattering and lateral force atomic force microscopy investigations [**70**], [**67**], [**68**], [**109**], [**86**], it has been rarely reinvestigated. AFM images showing flat and sharp terraces with steps of unit cell height cannot replace spectroscopic techniques completely, because of the locally confined information in AFM. Some admixture of SrO termination or a few SrO islands on top can easily lead to a termination that is more precisely described as mainly TiO_2 terminated (or Ti-rich) with a few percent SrO termination [**110**], [**111**], [**112**], [**113**], [**114**].

5.10 Summary

Strontium titanate samples have been prepared following typical steps of standard preparation procedures and analyzed using x-ray photoemission (XPS) and x-ray photoelectron diffraction (XPD). The purpose of the investigations has been twofold, first to analyze surfaces and in particular surface terminations by this particular set of methods and then to find access to routes of preparations for both Ti- and Sr-rich surface terminations.

Traces of adventitious carbon and water contaminations have been only found on ex situ prepared samples, as well as some fluorine after BHF treatment. Otherwise, XP spectra have confirmed the presence of Sr^{2+}, Ti^{4+} and O^{2-} related to STO only, but did not indicate other surface species, confirming the success of the preparations. The well-developed diffraction features observed in XPD angular distribution curves (ADCs) demonstrate the good structural ordering of all surfaces. In addition, there have been minor but significant deviations in the appearance of the ADCs in dependence on the kind of surface preparation. In particular, for Sr3d polar scan ADCs along [100] azimuth a fingerprint region has been identified between $\theta = 10°$ to 35°, which sensitively indicates changes in the surface termination. Preliminary analysis on the basis of forward scattering has indicated that the appearance of this fingerprint region in the ADCs is strongly affected by scattering of photoelectron waves from emitters more deeply below the topmost layers on scattering atoms in the surface layer. However, detailed analysis and understanding of the terminations has only been achieved by performing MSC calculations for $SrTiO_3(001)$ and adapting experiment and theory by an adequate handling of ADC background. Excellent overall agreement has been obtained for STO using ideally terminated bulk structures, mostly rather independent from the special TiO_2 - or SrO- termination. However, theory has also clearly confirmed the Sr3d-[100] fingerprint region with high sensitivity on the termination. In this manner it was possible to describe ”as received” and ”O_2 -annealed” samples as being TiO_2 - and SrO-terminated, respectively, while standard BHF-treated samples turned out to be mostly TiO_2 - terminated but with a non negligible admixture of different, likely SrO-type termination. Thus, both TiO_2- and SrO-terminated STO samples have been successfully prepared.

Despite the high energy and the low surface sensitivity used here and despite the complex structure of the materials investigated, angle-dependent XPD was successfully used to analyze surface terminations for STO and may be suitable for other ABO_3-type oxides.

It is suggested, that more data should be recorded at more surface-sensitive angles of emission (high polar angles) and at more surface-sensitive kinetic energies (<500 eV), in order to permit detailed analysis also of surface relaxations [**115**]. On the other hand, the evidence from our investigation does clearly indicate that XPD investigations provides another experimental tool to investigate the surface termination of complex oxides as has been shown here for ABO_3 -type transition metal oxides. More complex structures will be investigated in the following chapter.

6 LCeMO

Electronic structure of $La_{0.7}Ce_{0.3}MnO_3$ thin films

6.1 Motivation

The hole-doped manganites $La_{0.7}X_{0.3}MnO3$ where 30% of the rare-earth atoms are replaced by divalent alkaline earth metal atoms like Ca, Sr or Ba are among the most studied systems in solid state physics today due to their rich phase diagrams [**25**], [**27**]. Their perovskite structure may be described as a three-dimensional network of corner-sharing MnO_6 octahedra which are responsible for their physical and chemical properties [**23**]. Each individual manganese site has a spin, orbital and charge degree of freedom and the interactions between them creates a conduction band and allows magnetic exchange interactions [**116**].

The resistivity vs. temperature ρ(T) curves of these materials shows a metal-to-insulator (or metal-to-semiconductor) transition at T_{MI}, typically in combination with a magnetic phase transition from ferromagnetism to paramagnetism at T_{Curie}. Zeners double exchange mechanism [**30**] accounts qualitatively for these effects. In the vicinity of the transition temperature and in an applied magnetic field, a large reduction of the resistivity is observed – the so-called (negative) colossal magnetoresistance effect [**41**].

Doping with Ce^{4+} on the other hand (LCeMO) should consequently lead to a mixture of 70% Mn^{3+} and 30% Mn^{2+} with an additional electron in the e_g orbital set. If the double exchange model is valid for all ions with different valences, then LCeMO should behave similar to LCMO or LSMO. In fact the double exchange model was applied by [**52**] to LCeMO bulk single crystals to include the Mn^{2+}/Mn^{3+} system. The authors presented R(T) and thermopower data but were careful not to mention the exact valence of Cerium which they did not measure directly by spectroscopic means. The fact that LCeMO also shows a metal-insulator transition, ferromagnetic order and the CMR effect is a strong indication for the double exchange mechanism; the question is whether or not it takes place between Mn^{2+} and Mn^{3+}.

Later it was found that the bulk samples were in fact a multiphase mixture and not single crystals [**117**], conventional solid-state reaction methods stabilize a CeO_2 secondary phase and / or La-deficient phase. The use of pulsed laser deposition soon enabled the epitaxial growth of single phase LCeMO thin films on various substrates [**118**], [**119**]. These were found to consist of Ce^{4+} and $Mn^{2+}/^{3+}$ valences by X-ray Absorption Spectroscopy [**120**], which hinted at electron doping. The fabrication of LCeMO/LCMO or LCeMO/STO/LCMO tunnel contacts and their characterization supported this assumption [**121**], [**122**].

On the other hand, thermopower [**123**], [**124**] and Hall mobility measurements [**125**], [**126**], [**127**] gave clear evidence of holes as charge carriers. The observation of nm-sized CeO_2 inclusions [**125**] by high-resolution transmission electron microscopy (HR-TEM) presented another twist in the research on LCeMO because it showed that films may contain a secondary phase that is not identifiable by X-ray Diffraction (XRD). Also it was mentioned that removing oxygen by annealing drives the system into the electron-doping state. This would mean that under reducing conditions electron-doped LCeMO is stable, however, the metal-to-insulator transition typical for a hole-doped manganite disappears. Having electrons doped into LMO by the introduction of Ce would be possible, but the desired properties would only be found under oxidizing conditions. Finally, another compromise was suggested by proposing that electrons are doped into the system, filling e_g holes, but that their number was not sufficient to create n-type doping [**126**]. Thus, there is ongoing discussion about whether LMO (I) accepts Ce doping without phase separation, (II) Ce^{4+} doping leads to excess electrons, i.e. Mn^{2+} and (III) whether there is double exchange between Mn^{2+} and Mn^{3+}.

To address these questions a series of measurements were planned and conducted. They will be presented in the following chapter. Results were published in [**62**] and are reproduced with kind permission of the American Physical Society (© 2009).

6.2 XPS spectra of LCeMO

To determine the most important factor for or against electron-doping the electronic structure of LCeMO has to be studied. By means of XPS and XAS the occupied and unoccupied density of states has been studied, with special regard to the valences of Mn and Ce.

Figure 6-1 shows an overview spectrum of a typical LCeMO sample directly after growth, following transfer into the UHV chamber but prior to cleaning. The relevant peaks of La (4d, 4p and 3d), Ce (3d), Mn (3p, 2p) and O (1s) are labeled. Small amounts of carbon contamination are found at the C1s peak position at 284.6 eV which can be removed in-situ by heating the sample to around 500 °C in an oxygen atmosphere of 10^{-6} mbar O_2 [**72**].

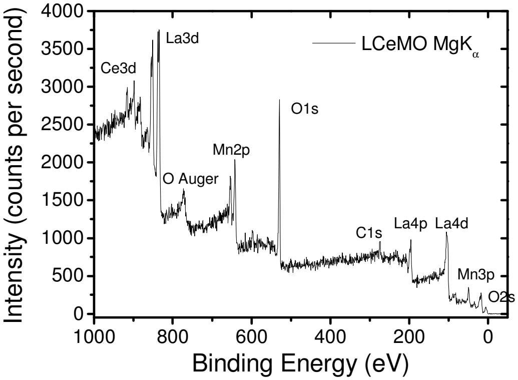

Figure 6-1: **XPS overview spectrum of a LCeMO sample, main lines are annotated (La4d, 4p, 3d, Ce3d, Mn3p, 2p and O 2s, 1s, KVV Auger).**

More detailed scans of the La3d and Mn2p peak regions are found in figure 6-2. Lanthanum on the perovskite A-site is chemically inert [**128**], [**129**] and is always found in a La^{3+} state. The Mn2p line is very broad (FWHM of $Mn2p_{3/2}$ is at least 3.5 eV for all samples) and does not show any fine structure. These two photoemission signals are thus difficult to use for the deduction of the electronic structure. A hint one may get from the shape of the Mn2p line is the absence of a satellite feature at 648.5 eV. This satellite is found in Mn^{2+} systems ($3d^5$) like MnO for instance at 6 eV higher binding energy with respect to the $Mn2p_{3/2}$ line. It also stems from photoemission from the 2p core level but there are two possible initial states in MnO. While the main line features a $3d^5L$ ground state, transfer of an electron from the ligand (L) oxygen to the manganese atom leads to a $3d^6\underline{L}$ initial state with a hole on the oxygen site ($\underline{L}$) [**130**]. Other ways of determining the valence of Mn will be presented in chapter 6.3.

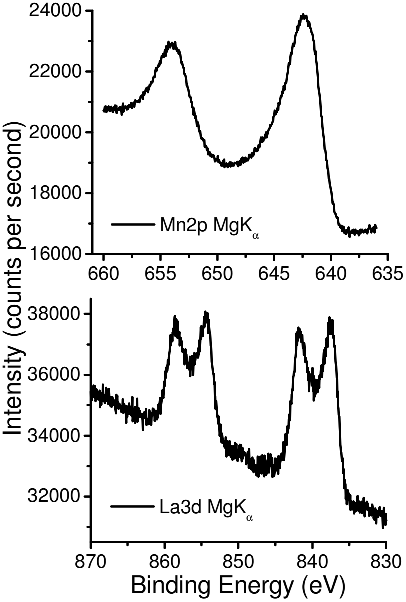

Figure 6-2: **XPS detail scans of the Mn2p (top) and the La3d (bottom) region of LCeMO. The Mn2p doublet is located at 642 and 654 eV, the two La3d doublets are centered at 840 and 857 eV**.

The Ce3d signal shown in figure 6-3 on the other hand allows direct conclusions about the valence of the Cerium ions doped into $LaMnO_3$. The complex shape of this photoemission line is explained in terms of three spin-orbit split doublets, separated by 18.6 eV.

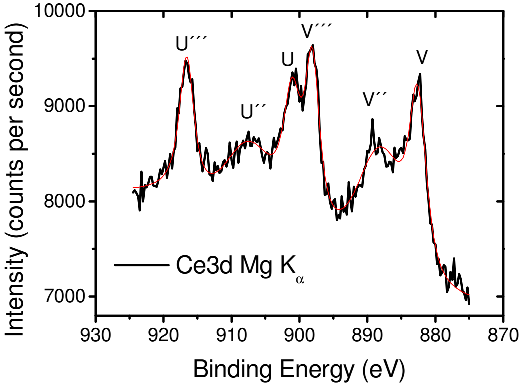

Figure 6-3: **Ce3d XPS data (black) and sum curve of peak fit (red). The three doublet structure is characteristic of Ce^{4+}.**

The states arise from different Ce4f occupancies [**131**], the labeling u and v refer to Ce3d$_{3/2}$ and Ce3d$_{5/2}$ states, respectively [**132**]. Table 6-1 shows the possible initial and final states for the Ce^{3+} and Ce^{4+} ions in Ce3d core level spectra.

Ion	Initial State	Final State
Ce^{3+}	$3d^{10}\,4f^1$	v^0, u^0: $3d^9\,4f^2\,O2p^5$
	$3d^{10}\,4f^1$	v^I, u^I: $3d^9\,4f^1\,O2p^6$
Ce^{4+}	$3d^{10}\,4f^0$	v, u: $Ce3d^9\,4f^2\,O2p^4$
	$3d^{10}\,4f^0$	v^{II}, u^{II}: $Ce3d^9\,4f^1\,O2p^5$
	$3d^{10}\,4f^0$	v^{III}, u^{III}: $Ce3d^9\,4f^0\,O2p^6$

Table 6-1: Summary and nomenclature of Ce^{3+} and Ce^{4+} initial and final states in the photoelectron emission process.

The shape of the Ce3d line in figure 6-3 is indicative of a tetravalent Cerium ion. Trivalent Ce, which consists of two spin-orbit split doublets only, may be found in minor amounts at the onset of the v feature at 877 eV and in the region between v and v^{III} at 885 eV (more details are given in the following chapter).

6.3 Valences in dependence of oxygen content

Early on in the studies of the perovskite manganites, one of the main goals was to correlate transport properties with photoelectron spectroscopic results. Because of the high surface sensitivity of XPS, this may seem difficult to realize. The possibility to look deeper into a sample by means of high kinetic energy XPS relieves this problem. The information depth of XPS is determined by the escape length of the excited photoelectrons. In a first approximation the length which an electron can travel in a solid is described by the distance between two inelastic scattering events. This so called inelastic mean free path (IMFP, λ) limits the information depth of x-ray photoelectron spectroscopy to about 3λ = 2.75 nm for Ce3d photoelectrons (E_{kin} = 370 eV) excited with Mg K_α (1253.6 eV) x-rays. Using Ag L_α (2984.2 eV) radiation and increasing the kinetic energy of Ce3d electrons to 2100 eV, the information depth almost quadruples to 9.87 nm [**81**].

This gives insight into the more bulk-related electronic structure of LCeMO. The use of the second order Bragg reflection of the monochromator for Al K_α x-rays allows the use of the Ag L_α line because it has roughly half the wavelength of Al K_α. Without monochromatization, however, the natural line width of 2.6 eV would prevent the use of a silver anode. The monochromatized line is 0.8 eV wide (compared to 0.4 eV for monochromatized Al K_α at the Ag3$d_{5/2}$ line, 0.7 eV for nonmonochromatized MgK_α and 0.85 eV for nonmonochromatized Al K_α), making it a practical source for most experiments [**133**], [**134**]. It must be noted, that the intensity is strongly reduced (2 orders of magnitude) due to the use of the second order Bragg reflection and the significantly lower cross section at higher x-ray energies.

Following a procedure by Beyreuther et al. [**72**] the LCeMO sample (60 nm thickness, T_{MI} = 250 K) was subjected to thermal treatment to remove oxygen and reduce the manganese ions. In hindsight it must be mentioned that, while the thermocouple reading was only 400 °C, the temperature must have been higher to achieve this degree of reduction. A comparison to data from Beyreuther gives a more realistic value of 600°C based on the observed Mn valence. The temperature was held for 30 minutes. Either the contact between thermocouple and sample holder was insufficient or thermal equilibrium was not reached after that time. The effect was, however, reversible by annealing in 750 mbar O_2 at 700 °C for 2h, ruling out the possibility that the sample was destroyed. Even temperatures as low as 350 °C were found to lead to oxygen outdiffusion [**127**].

Resistance vs. temperature measurements (measured by R. Werner, figure 6-4) clearly prove that these reducing conditions lead to a disappearance of the metal-to-insulator transition and the concomitant increase in resistivity at low temperatures. The resulting changes of the Ce3d and Mn3s photoemission lines are found in figures 6-5 and 6-6.

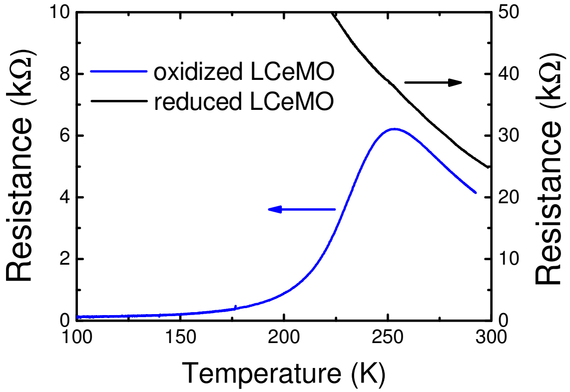

Figure 6-4 (measured by R. Werner): R(T) behaviour of LCeMO before (blue) and after (black) reduction showing a metal-to-insulator transition (blue) and semiconducting behavior (black), respectively

Ce3d and Mn3s spectra before and after in-situ annealing were taken with Ag L_α x-ray irradiation. While the upper curve in figure 6-5 consists of the abovementioned three doublets shown in red, blue and green color, an additional orange doublet is found in the Ce3d data after reducing the sample. It represents the v^I and u^I lines of Cerium in a trivalent state. The v^0 and u^0 contributions were not included in the curve fitting process but are located on the right hand side of the two red peaks, i.e. at roughly 877 and 895 eV.

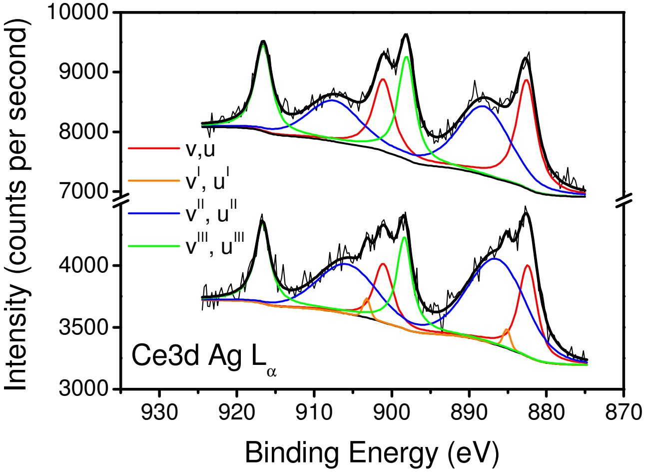

Figure 6-5: Comparison of the Ce3d region before (top) and after (bottom) annealing. Peak fits show the appearance of an additional component u', v', indicative of Ce^{3+}.

The Mn3s line in figure 6-6 is special due to its exchange splitting, which means that the open Mn3d valence band shell (3d holes) interacts with the created Mn3s core hole. This leads to a multiplet structure with different energies in the photoelectron spectrum. In this case there are two possible configurations, parallel or antiparallel alignment of the remaining Mn3s electron spin to the Mn3d electron spin. The value of the exchange splitting is proportional to the size of the Mn3d spin via $\Delta E \sim 2S + 1$. This means of course, that the doublet separation of Mn3s is a measure for the Mn3d occupation, i.e. the valence of Mn. Typical values are found in Galakhov et al. [**135**]. A comparison shows that ΔE = 5.0 eV for the oxidized sample equals an effective valence of +3.4 and that ΔE = 5.7 eV for the reduced sample corresponds to a mean valence of +2.5. This yields the conclusion that the sample could in fact be reduced by decreasing its oxygen content. It is thus highly likely that the fresh grown sample showing a metal-to-semiconductor transition is composed of Mn^{3+} and Mn^{4+} ions, while the reduced sample contains a mixture of Mn^{2+} and Mn^{3+}.

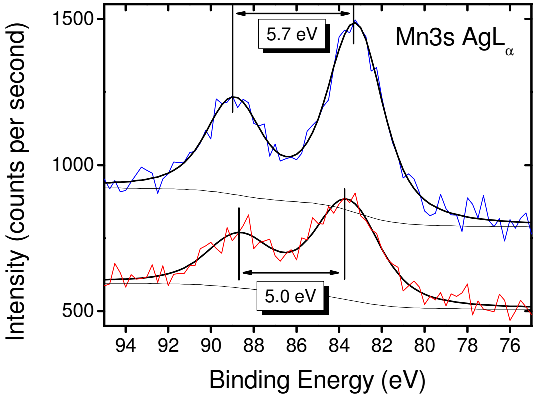

Figure 6-6: Comparison of Mn3s photoemission lines of LCeMO before and after annealing, showing a decrease of the doublet separation by 0.7 eV.

The effect of reduction on the Cerium valence is not so easily understood. On the one hand, it is clear to see that reducing conditions do not only affect the Mn valence but also the Ce valence. On the other hand, assuming the highly desired coupling between the dopant atom and the central atom, a shift from Mn^{3+} / Mn^{4+} towards Mn^{2+} / Mn^{3+} would be accompanied by a charge transfer from Ce to Mn and a stabilization of its tetravalent state.

What can be concluded from this XPS dataset is that only oxidizing conditions yield LCeMO with the wanted properties. Only if the mean valence of Mn is between +3 and +4 does the sample behave like a ferromagnetic metal at low temperatures and show the colossal magnetoresistance effect near its transition temperature. If, by reducing the sample via oxygen outdiffusion, the mean Mn valence is lowered to values between +2 and +3 these properties cease to exist and the sample becomes a semiconductor at low temperatures. The question of electron doping cannot be resolved conclusively in this way because the Mn and Ce valence were not coupled strongly enough to be simultaneously tuned to the nominal valences of $^{+III}$Mn$_{0.7}$$^{+II}Mn_{0.3}$ and Ce^{4+}. Instead the oxygen loss leads to a reduction of manganese and cerium ions at the same time.

6.4 Valences from X-ray Absorption Spectroscopy

To further elucidate the electronic structure of LCeMO, x-ray absorption experiments were carried out at the ANKA synchrotron facility in Karlsruhe. For this purpose several LCeMO samples with different properties and film thicknesses were grown on $SrTiO_3$ by PLD. All films were grown at a substrate temperature of T_S = 720 °C but with varying oxygen pressures during ablation. For $p(O_2)$ = 8 Pa the LCeMO samples contained no CeO_2 inclusions as evidenced by XRD. This partial pressure is also ideal for the morphology of the films because higher oxygen pressure during growth leads to strongly increasing surface roughness. The reason is found in the growing step density, the resulting lower surface mobility and 3D island growth behavior.

X-ray absorption spectra of four samples were recorded at the O K (O1s -> O2p), the Mn $L_{2,3}$ (Mn2p -> Mn3d) and the Ce $M_{4,5}$ (Ce3d -> Ce 4f) edges in two different detection modes. For a surface sensitive study of the samples, the drain current may be measured. For information about bulk properties the fluorescence yield detection mode is suggested.

A typical spectrum of the O K edge of LCeMO, measured in FY mode, is seen infigure 6-7. It must be noted that partial covalency must be given to even find unoccupied O2p states. In a fully ionic picture the oxygen 2p shell would be closed. Finding a peak at 530 eV in the XA spectra is clear evidence of hybridization between Mn3d and O2p. Thus the O K edge maps directly the unoccupied electronic structure at the metal site but without the multiplet effects found for instance at the Mn L edge [**136**]. The second feature at 532 to 537 eV is attributed to La5d (Ce), La4f (Ce) states hybridized with O2p states. The third set of states is found at about 543 eV and comes from hybridization with higher energy metal-states like Mn 4sp and La 6sp. Fluorescence yield detection mode was typically used for the O K edge to get information about the bulk of the sample, rendering possible surface contaminations like water negligible.

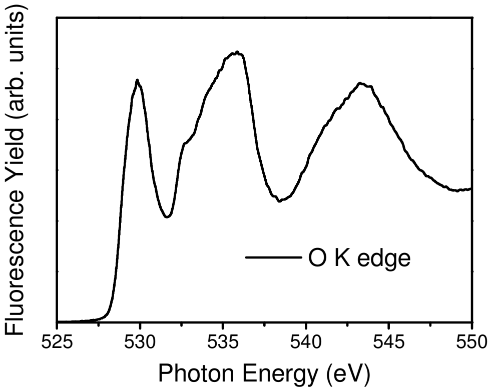

Figure 6-7: **X-ray absorption intensity at the O K edge of LCeMO in fluorescence yield detection mode, prepeak at 530 eV (empty Mn2p-O1s hybrid orbitals), La(Ce) 4d, 5f states hybridized with O2p are found at 537 eV, higher energy metal states hybridized with O2p are found above 540 eV.**

Figure 6-8 shows a typical Mn $L_{2,3}$ edge spectrum of LCeMO taken in TEY mode. Both the L_3 edge at 642 eV and the L_2 edge at 653 eV are strongly broadened by multiplet effects [**137**]. The arrow marks the relevant feature at 640 eV, which is the indicator for the presence of Mn^{2+} ions [**138**]. At the Mn L edge most spectra were taken in total electron yield mode because of strong self-absorption effects that distort the FY signal.

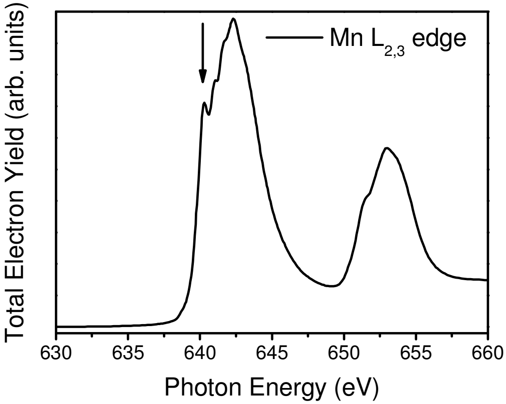

Figure 6-8: **X-ray absorption intensity at theMn L_3 (642 eV) and Mn L_2 (653 eV) edge of LCeMO. The arrow marks the region where divalent Mn ions appear.**

Figure 6-9 presents a Ce $M_{4,5}$ edge XA spectrum taken in TEY mode. It consists of two very similar transitions at 884 eV and 902 eV, doublet split by 18 eV and two corresponding satellite features 5 eV to the right of each of the main lines. The shape is indicative of Ce^{4+} as will be shown later. The La $M_{4,5}$ edge consists of two narrow lines. As mentioned earlier, La is chemically inert and is always found in the La^{3+} state on the A-site of the ABO_3 compounds. This $5d^0$ configuration does not show any additional shoulders or satellites and is rather irrelevant for the electronic structure.

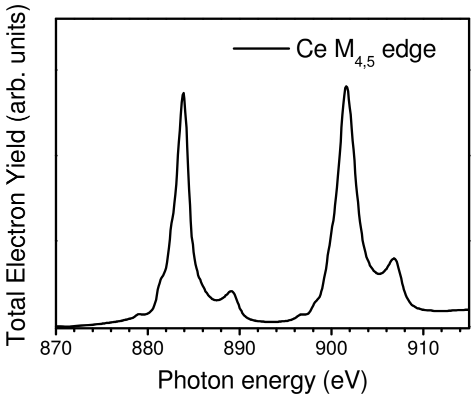

Figure 6-9: **X-ray absorption intensity at the Ce $M_{4,5}$ edge of a LCeMO thin film in total electron yield detection, main lines at 884 / 902 eV are accompanied by satellites at 889 / 907 eV.**

In order to correlate the relative spectral weight at the oxygen preedge with the amount of holes and the transport properties of the respective sample, the O K preedge spectral weight and the Mn L density of states at 640 eV was studied. It was found that when the Mn L edge shows a Mn^{2+} signature, the O K edge shows more intensity at 530 eV. This is exemplified in figure 6-11 showing a comparison of the two extreme cases in this study, namely a sample grown at $p(O_2)$ = 25 Pa without post-growth annealing (T_{MI} = 180 K) and consequently a charge-ordered ground state at low temperatures and a sample grown at $p(O_2)$ = 8 Pa with 1h of post-growth annealing, a T_{MI} of 232 K and a metallic ground state.

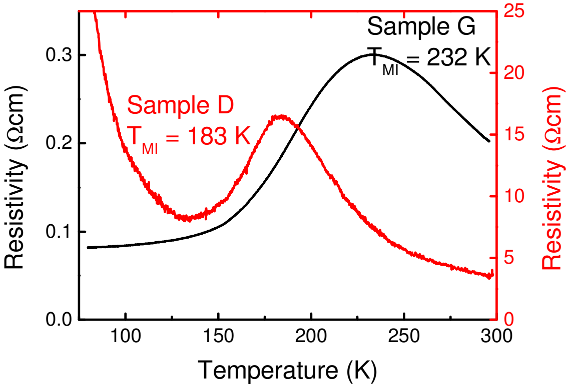

Figure 6-10 (measured by R. Werner): Electrical transport measurements of two LCeMO samples with different R(T) behavior. Sample D (as grown) has a T_{MI} = 183 K and a semiconducting low-temperature ground state while post-growth annealed sample G has higher T_{MI} = 232 K and a metallic ground state.

Charge ordering is a phenomenom found in as-grown LCeMO films before being annealed in an oxygen atmosphere, see figure 6-10 and [**62**]. The in-plane resistivity vs. T curves were measured using a van-der-Pauw setup (four contact measurement technique for two-dimensional samples of arbitrary shape) and are kindly provided by R. Werner. They show a slight metal-to-insulator transition at 183 K and drastically increasing resistivity below 100 K. After annealing in oxygen, the metal-to-insulator transition temperature increases [**62**] and the resistivity decreases. Again it must be said that only samples with R(T) curves as shown in figures 6-4 (blue line) and 6-10 (black line) are technologically relevant. If the oxygen content is even lower, semiconducting R(T) curves as in figure 6-4 (black line) are observed.

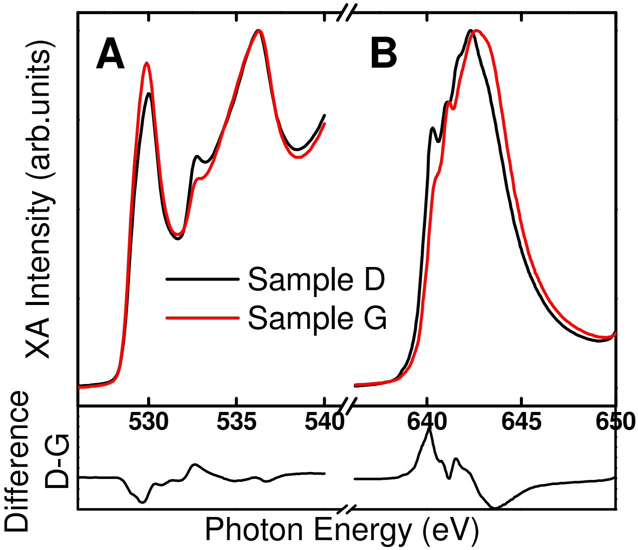

Figure 6-11: **The corresponding XA intensities at the O K and Mn L_3 edges of samples D (black) and G (red), low and high oxidized LCeMO samples. The difference curve in the lower part shows the transfer of spectral weight in dependence of oxidation state.**

The two features at the O K edge in figure 6-11 a) at 530 and 532.8 eV are labeled valence band VB and upper Hubbard band UHB in accordance with Merz et al. [**139**]. The authors could show by analyzing polarized XA spectra of single crystals that the VB spectral weight comes from in-plane oxygen $O2p_x/O2p_y$ states hybridized with $Mn3d_{x^2-y^2}$ states. The UHB stems from out-of-plane $O2p_z$ states hybridized with $Mn3d_{3z^2-r^2}$ metal states.

Accordingly, when comparing oxidized LCeMO (G) to reduced LCeMO (D), one can see that spectral weight is transferred from in-plane states to out-of-plane states. This decrease in electronic bandwidth along the sample surface is the reason for the higher in-plane resistivity of the reduced sample D compared to the oxidized sample G in figure 6-10.

This behavior is reflected at the Mn L edge in figure 6-11 b) where the form and shape of the Mn L_3 edge change in a way that was previously related to hole doping [**136**]. The fact that the Mn L edge is even affected by the hole content means that the O2p states are indeed strongly hybridized with Mn3d states. Only if a certain degree of covalency exists, can the oxygen content influence the manganese valence. The decreasing 3d electron count ($Mn^{2+} > Mn^{3+} > Mn^{4+}$) upon oxidation leads to transfer of spectral weight from the Mn^{2+} region at 640 eV to the Mn^{4+} region at 644 eV (change in chemical potential). Conclusion: Samples with more oxygen have more holes in Mn3d-O2p-hybrid states and an increased manganese valence.

6.5 Valences in dependence of sample depth

Similar to the XPS approach above, information about the electronic structure of the bulk was obtained. For this purpose, the FY spectra of Mn and Ce were also taken in FY detection mode. Results are presented for the Ce M_5 edge and the Mn L_3 edge in figures 6-12 and 6-13.

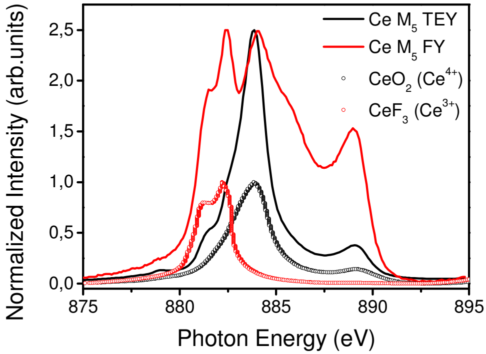

Figure 6-12: **XA spectra of sample D at the Ce M_5 edge in surface- and bulk-sensitive detection (black and red solid lines, respectively). Reference spectra of CeO_2 and CeF_3 are added for comparison (red and black dots)**

There are striking differences between surface-sensitive TEY and bulk-sensitive FY datasets for sample D. The black line shows the signal from the very surface of LCeMO and may be compared to the blue curve, a reference dataset for CeO_2 taken from Mitra et al. [**120**]. The red bulk signal clearly contains additional Ce^{3+} ions as is evident from comparison with the green line (reference data for CeF_3 taken from the same article). This is a very confusing finding at first glance, because the ablated target is made of stoichiometric amounts of pure CeO_2, La_2O_3 and Mn_2O_3 powders and was heated for several hours in oxygen. All preparation steps are performed under oxidizing conditions so tetravalent Ce should be stabilized. Finding Ce^{3+} means that Ce, instead of donating one electron, even accepted one electron. The origin of this electron is, however, unclear. The result also casts doubts on the determination of valences by means of surface-sensitive techniques and correlating them to true bulk properties like magnetization or resistivity.

This is underlined by figure 6-13, the respective spectra at the Mn L_3 edge. Again, the comparison of FY and TEY signal reveals large differences between the valences of manganese at the surface and in bulk. First of all, the edge becomes broader towards higher photon energies where Mn^{4+} is located. This chemical shift leads to the reference spectra [**140**] of MnO (Mn^{2+}, $3d^5$), Mn_2O_3 (Mn^{3+}, $3d^4$) and MnO_2 (Mn^{4+}, $3d^3$) being found at 640 eV, 642 eV and 644 eV according to the higher Mn 2p core level binding energies with decreasing 3d electron count. Additionally, the absence of the peak at 640 eV is evidence that speaks against the presence of Mn^{2+} ions. Since quantification is difficult, it is well possible that Mn^{2+}, Mn^{3+} and Mn^{4+} are found in LCeMO.

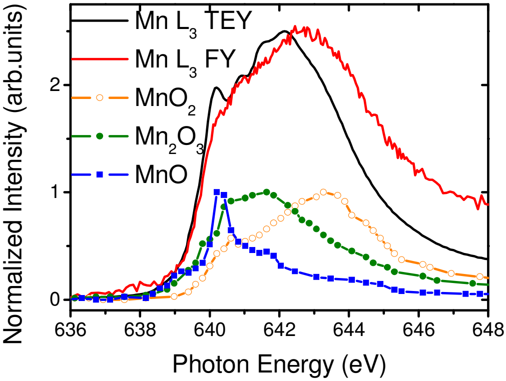

Figure 6-13: **XA spectra of sample D at the Mn L_3 edge in surface- and bulk-sensitive detection mode (TEY and FY, black and red solid lines, respectively). Reference spectra of MnO (blue dots), Mn_2O_3 (green dots) and MnO_2 (orange dots) are added for comparison.**

The picture that emerges from figures 6-12 and 6-13 is that of a surface region with reduced Mn and oxidized Ce on top of a bulk phase containing oxidized Mn and reduced Ce. It looks like the preparation conditions were not oxidizing enough to yield tetravalent Cerium throughout the sample and that only post-growth annealing can achieve this. This was also suggested from XPS data (chapter 6.3). The oxidation step that is performed after growth either oxidizes Ce towards Ce^{4+} or it doesn't. In any case the Ce valence does not couple to the Mn valence, i.e. Mn is oxidized as well instead of being electron-doped by Ce. The result is an oxidized bulk phase with Ce^{4+} and Mn^{3+}/Mn^{4+} with the desired magnetic and transport properties and possibly a reduced surface layer with the desired valences.

6.6 Magnetic structure of LCeMO

The magnetic and structural properties of the manganites are investigated next. XMCD and magnetization measurements give additional insight into the LCeMO system. For this purpose another experiment was performed at ANKA. A sample grown under the same conditions as sample D was post-growth annealed in oxygen to change from the charge ordering state towards a system with a T_{MI} of 225 K. Then x-ray magnetic circular dichroism spectra were taken at liquid nitrogen temperature. The difference between two x-ray absorption spectra taken with circularly polarized light (left / right circular) and in an applied magnetic field ($B\uparrow$ / $B\downarrow$) gives element-specific information about the presence of ferromagnetism, its orientation and the value of the spin and orbital magnetic moment. The sheer presence of this dichroic signal is evidence of the ferromagnetic nature of the LCeMO system. The fact that it appears at the Mn L edge proves that Mn ions are responsible for the magnetism of the sample.

What was previously known from magnetization measurements is that the saturation magnetization is sensitive to the oxidation state of the samples. The magnetic moment in multiples of the Bohr magneton μ_B ($\mu_B = eh/4\pi m_e = 9{,}3\ 10^{-24}\ Am^2$) is written as $\underline{m} = \mu_B(\underline{L} + g_S\underline{S})$ and takes theoretical values of 4.3 μ_B for LCeMO and 2.7 μ_B for LCMO. Because La and O have closed shells, only Mn has a magnetic moment. Assuming that the orbital moment is quenched (cubic environment, large crystal field, [**141**]), the spin is the only relevant parameter (g_S, the Landé factor is 2 for electrons). The expectation values for Mn^{2+} ($3d^5$), Mn^{3+} ($3d^4$) and Mn^{4+} ($3d^3$) are 5 μ_B, 4 μ_B and 3 μ_B respectively (S = 2s+1). It may thus be expected that annealing leads to a lower values of m_S because it shifts the 3d count towards lower values if Mn^{4+} replaces Mn^{2+}. This proves again that the necessary post-growth annealing leads to higher oxidation states and consequently lower magnetization. It must be noted, however, that the magnetization changed from 3 μ_B/Mn to 2.4 μ_B/Mn, which is even lower than the expected value for a 70 : 30 mixture of Mn^{3+} and Mn^{4+} as in the case of the hole-doped manganites LCMO and LSMO.

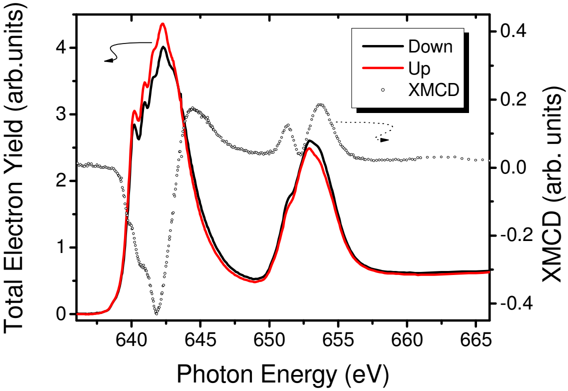

Figure 6-14: **XA spectra of the Mn L edge of a LCeMO sample recorded with light of different helicity at a temperature of 77K (red and black curves) and the resulting XMCD signal (dotted line).**

The $MnL_{2,3}$ edge shown in figure 6-14 has a different shape and intensity for two different (opposite) orientations of the external magnetic field, B↑ and B↓. The presence of the Mn^{2+} shoulder at 640 eV hints at incomplete oxidation of the film surface (cf. chapter 6.5). The XMCD signal amounts to 10 % at liquid nitrogen temperatures and is clear evidence of ferromagnetism in the studied sample. Sum rule analysis is typically not performed on Mn because of the very large error bars. The first problem lies in the value of n_{3d}, the number of 3d electrons, which is unknown because the valences of Mn are not exactly known. The second and more important source for errors is the integration itself. Due to the overlapping multiplet structures of the Mn L_3 and L_2 edges the exact determination of the necessary integrals depend on the arbitrary choice of the edge region. Finally, the appearance of a magnetic multipole term gives additional errors of up to 50% for a $3d^4$ configuration [**142**].

Because sum rule analysis is difficult, most reports use comparisons with data from well-defined model systems for analysis. A simple comparison of the measured XMCD signal with the shape and position of the dichroic signal of hole-doped LCMO in chapter 8.4 (and hole-doped LSMO in [**143**] for instance) shows the similarity between the two datasets. The dichroic signal is highest at the position of Mn^{3+} (642 eV) but almost absent at 640 eV where Mn^{2+} should be found. This becomes especially evident when looking at true Mn^{2+} XMCD spectra which are for instance observed in (Ga,Mn)As) [**144**].

To sum it up, ten percent dicroic signal are less than one could expect from this system, a ferromagnetic (oxidized) LCeMO sample with a T_{Curie} of 225 K. In LCMO almost 30 % XMCD are found at LN_2 temperatures. Nevertheless, these are the only reported numbers on the Cerium doped manganites, so there is no comparison with literature. Yanagida et al. [**145**] presented XMCD data on LCeMO but did not show numbers. The magnetization measurements mentioned above together with these XMCD results prove that the magnetic situation is more complicated than expected because the values do not fit to the expected magnetic moment. Applying the sum rules despite the implications mentioned, a magnetic moment of about 0.6 μ_B/Mn site is found which is about five times smaller than the magnetic moment derived from SQUID data. Unpublished data by Stefan Gold of the Schütz group found 1.1 µB in a LCeMO sample [**146**]. But since the oxidation state of their sample is not known, a quantitative comparison is impossible.

In view of the finding that increasing Mn^{2+} content correlates with lower T_{Curie}, i.e. less stable ferromagnetism and the fact that the LCeMO sample surface is typically less oxidized than bulk explains this deviation. While SQUID measurements probe the entire sample volume, XMCD only gives information about the top few nm of the film.

6.7 Discussion

Following controversial discussions in literature about the nature of doping in lanthanum manganites where La^{3+} is substituted by Ce^{4+} and the successful preparation of LCeMO thin films, extensive spectroscopic studies were conducted on these samples. X-ray Photoemission was performed and the valences of Mn and Ce were investigated with respect to the oxidation state of the samples. X-ray Absorption studies were conducted on the valence states of Mn and Ce in dependence of oxidation state and with different information depths. Finally, X-ray Magnetic Circular Dichroism was recorded and analyzed. The experiments are summarized as follows:

- XPS data shows a broad Mn 2p line and a chemically inert La 3d line, which yield little information on the electronic structure of the samples. Mn3s and Ce3d signals allow determination of manganese and cerium valences and have been investigated in dependence of oxygen content. Reduced samples show Ce^{4+} and an average Mn valence between +2 and +3. Oxidized samples also contain Ce^{3+} and have a mean Mn valence between +3 and +4. Only oxidized samples have low resistivity and show a metal-to-insulator transition, while reduced samples are semiconducting.
- XAS allows the study of unoccupied Mn, O and Ce states in dependence of information depth. With increasing oxygen content, the Mn^{2+} shoulder decreases and the amount of holes in Mn-O hybridized bands increases. With increasing information depth, the Mn L edge shifts towards higher manganese valence and Ce M spectra reveal additional Ce^{3+}. While the surface of as grown samples shows the presence of Mn^{2+} and Mn^{3+} as well as Ce^{4+}, the bulk valences were found to be Ce^{3+}/Ce^{4+}, $Mn^{2+}/Mn^{3+}/Mn^{4+}$.
- XMCD data shows the ferromagnetic order of manganese ions but also indicates that Mn^{2+} seems not to be involved in the double exchange mechanism responsible for this ordering. The magnetic moment according to XMCD (and SQUID) is lower than expected.

In conclusion, none of the experimental results speaks in favour of electron doping in the La-Ce-Mn-O system. All results can be only understood in terms of mixed Mn^{3+} / Mn^{4+} species being responsible for the measured properties. With oxygen annealing after thin film growth the films gain their desired properties, exhibit ferromagnetism up to T_{Curie} of 260 K, show a metal-to-insulator transition at T_{MI} of 260 K and change their resistivity in dependence of the strength of an applied magnetic field. Without this oxidation step, LCeMO samples are semiconducting, even insulating. Doped holes instead of electrons are thus responsible for the desired properties. The origin of these holes is subject to further discussion.

Of course the valences of Cerium and Manganese atoms are affected by the post-growth annealing step. While as grown samples (and samples that have been reduced by oxygen outdiffusion) show a mean manganese valence between +2 and +3 with cerium valences of 3+ and +4 throughout the sample, oxidation leads to a concerted increase of valences. Not only is Ce oxidized to its nominal tetravalent state but also is Mn oxidized to an average value between +3 and +4. This raises questions about the coupling between Ce and Mn valences. The coupling between these two ions appears to be too weak to have tetravalent Ce donate electrons to Mn. The doping of an electron from Cerium to Manganese must take place via the oxygen cage around Ce that is also part of the MnO_6 octahedron around Mn. In fact, the O K edge in XAS shows that hybridization is found between Mn and O as well as Ce and O. However, if parts of Ce are not located there but form CeO_2 inclusions, or have little overlap due to distortion, this electron doping may be ineffective. While Cerium in fact donates four electrons, making it tetravalent, these charge carriers do not necessarily reach the bonding partner but are located in the strongly hybridized Ce4f-O2p valence band [**147**].

Werner et al. [**62**] found nanometer sized CeO_2 inclusions in the studied films by means of high-resolution transmission electron microscopy that had gone undetected by XRD due to their small size. This opens the way for an explanation of the findings above. If Ce forms CeO_2 precipitates instead of occupying A-sites, a cation-deficient phase results that leads to hole-doping. In the end, a consistent picture emerges from the spectroscopic results in this chapter in the sense that the desired properties are associated with hole-doping. The hole-doped behavior of the films may be explained by the presence of cation vacancies due to CeO_2 clustering. Magnetic measurements also fit into the Mn^{3+}/Mn^{4+} double exchange scenario while results of structural investigations will be presented in the next chapter.

7 LXMO

Microstructure of $La_{0.7}X_{0.3}MnO_3$ (X=La, Ca, Sr, Ce) thin films

7.1 Motivation

Following unresolved questions about the microstructure of LCeMO (chapter 6) and the successful application of XPD for the complex oxides (chapter 5), it is the aim of this chapter to present and discuss diffraction data obtained on doped manganite thin film samples.

This is a further step in the use of XPD, commonly employed for the study of more simple systems, metals, binary compounds or adsorbates on metal surfaces, towards quarternary compounds with a high degree of complexity with respect to their microstructure.

The interconnecting 3D network of corner-sharing MnO_6 octahedra forms the backbone of the crystal structure of the manganite perovskites. The Mn-O-Mn bonds are the pathways along which carriers travel through the film. The bond angle determines the transport and magnetic properties of the samples because the hopping integral t depends on it. For the case of SE [**57**], [**58**] it has been demonstrated that the Mn-O-Mn bond angle φ and the Néel temperature are proportional via $T_{Néel} \sim \cos^2\varphi$. The magnetic properties on the other hand have been found to be dependent on the angle between Mn core spins, $t = t_0 \cos(\rho/2)$ [**33**]. The transfer probability ranges between zero for ↓↑ / ↑↓ and 1 for ↑↑ / ↓↓. This is the underlying principle of magnetoresistance - aligned magnetic core moments result in low resistance.

The effects of doping on the properties are threefold: The band-filling is directly determined by the amount of dopands while the different size of the doping atom changes the orbital overlap and thus the effective bandwidth. Finally, the disorder created on the A-sites must be considered because it leads to oxygen displacements and accordingly changes bond angles and bond lengths as well.

The samples are thus categorized in terms of their tolerance factor and their A-site cation size variation because these values have an influence not only on the results of photoelectron diffraction measurements but also on the abovementioned bond angle and the sample properties.

Chapter 6 deals with the structure of the lanthanum manganites LXMO (X = La, Sr, Ca, Ce), starting of course with the parent compound LMO but moving on to the more technologically relevant CMR materials LSMO, LCMO and LCeMO. Results of this chapter were submitted to the Journal of Applied Physics on November 8, 2012 and accepted for publication on January 15, 2013.

7.2 XPS and XRD results

A first look at the samples was performed by means of XPS, focusing on stoichiometry, cleanliness and electronic structure. For reasons given in chapter 6.2, not much information is available from the photoemission peaks of the doped manganites. Amorphous carbon and adsorbed water was removed by in situ annealing in oxygen and confirmed by XPS.

Due to the multiplet structure of the manganese photoemission line and the random distribution of Mn^{3+} and Mn^{2+}/Mn^{4+} ions, the Mn2p spectra of all samples are rather difficult to analyze. The full width at half maximum (3.7 ±0.2 eV at a pass energy of 20 eV) and the doublet separation (11.7±0.1 eV) are almost identical for all samples, allowing no conclusions to be drawn from this particular core level about differences in the electronic structure. Results are presented on the left hand side of figure 7-1.

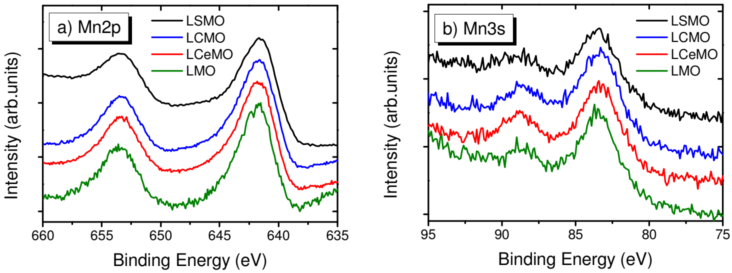

Figure 7-1: **Comparison of Mn2p (left) and Mn3s (right) XPS lines of LSMO (black), LCMO (blue), LCeMO (red) and LMO (green).**

The Mn3s line, which is indicative of the Mn valence was measured as well, shown in figure 7-1 on the right. The doublet separation is 5.4±0.1 eV, in perfect agreement with data by Galakhov et al. [**135**], who systematically investigated doped manganites and concluded that for Mn formal valences between 3 and 3.3 the Mn3s splitting is stabilized at this value.

Lanthanum as well as the dopand atoms Ca and Sr are exclusively found in the following valences: La^{3+}, Ca^{2+}, Sr^{2+}. The case of Ce is still a matter of debate. All emission lines can be reasonably well fit by a single species. Due to the ex situ transfer of the samples from the PLD chamber to the XPS chamber and the resulting uncertainty about the absolute amount of oxygen, the stoichiometry of the samples was analyzed with respect to the cations only. All samples have values that are close to the ideal stoichiometry as expected for films grown by PLD.

Samples were also studied by means of x-ray diffraction (XRD) by Robert Werner from the Institute of Physics at the Eberhard-Karls-University Tuebingen directly after growth. The focus was on the lattice constants of the films. The out-of-plane c-axis is easy to determine, it’s value may be derived from the Bragg condition $2d_{hkl}\sin\Theta = n\lambda$ from one or more of the (00l) reflexes in the Θ-2Θ scans. Table 7-1 gives an overview of the values for the four investigated samples.

Compound	LMO	LSMO	LCMO	LCeMO
c-axis [Å]	3.889	3.838	3.818	3.887

Table 7-1 (data from R. Werner): Lattice constant c for the different compounds determined by XRD.

The c-axes of thin manganite films are a measure of the oxygen content of the samples, because oxygen vacancies increase the c-axis [**148**], [**127**], [**149**]. Values in literature are: LCeMO-(3.88 ± 0.01Å, [**62**]), LCMO-(3.81 ± 0.02Å, [**150**], [**151**], LSMO-(3.84 ± 0.01Å, [**152**]), LMO-(3.90 ± 0.03Å, [**149**]. All samples have almost ideal c-axes and oxygen contents.

Reciprocal space mapping also performed by R. Werner yields the in-plane lattice parameters which were found to be identical to the lattice constants a and b of the substrate STO (a = b = c = 3.905 Å). All samples are fully strained to the substrate as expected for the manganites [**153**]. The comparable values for LSMO / LCMO and LMO / LCeMO will be addressed later.

7.3 XPD results

In the following chapter polar scans of manganese and oxygen atoms in all four samples are presented and discussed. The chapter is divided into three segments – angular distribution curves of the MnO_6 octahedra are shown first (7.3.1), followed by diffraction patterns from the A-site atoms, La, Sr, Ca and Ce. They are further differentiated into core levels with photoelectron kinetic energies near or above 1000 eV (high kinetic energy, 7.3.2) and near 400 eV (low kinetic energy, in 7.3.3).

7.3.1 Polar scans from the MnO_6 building blocks (Mn2p, O1s)

The first results are from the Mn2p core level, as usual for both low-index crystallographic directions. The left column of figure 7-2 shows the [110]-ADCs of LMO, LCMO, LSMO and LCeMO from top to bottom. The top graph showing the parent compound LMO is compared to MSC simulations for two different clusters, LaO- (XO-) and MnO_2-termination in green and red. The doped samples are presented together with the thermodynamically more stable MnO_2-termination.

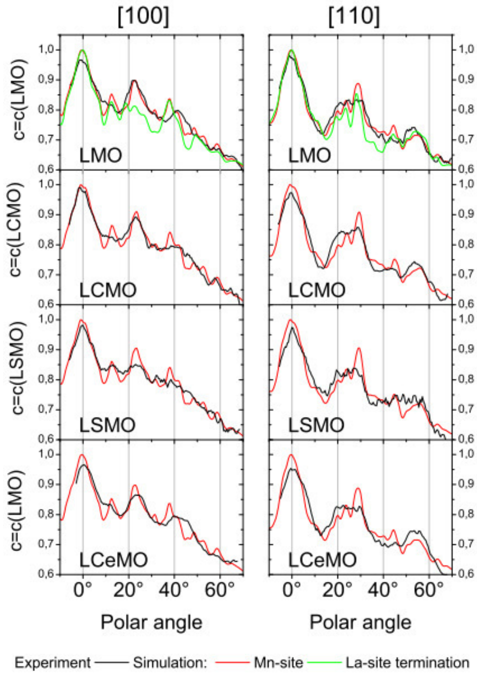

Figure 7-2: Comparison of XPD polar scans (black lines) of Mn2p in the [100]-direction (left) and along the [110]-azimuth (right). The upper graph shows the diffraction pattern of LMO and results of MSC calculations for a LaO- (green) and a MnO_2-terminated cluster (red). The angular dispersion curves of LCMO, LSMO and LCeMO (from top to bottom) are compared to the latter termination only.

In the Mn2p-[100] scans the main structures are found at approximately 0°, 22° and 42° in the experimental data. They are not found at the positions that one would expect in a simple forward scattering picture like 45° ([101]). The Mn2p-[110] angular distribution curves on the right hand side of figure 7-2 mainly consist of a broad complex-shaped region between 15° and 35° with an additional peak at 55°. From the topmost two layers, only the signal at 55° shows a clearly resolved peak, showing the necessity to properly treat multiple scattering effects in theory.

The medium-angle region between 15° and 35° is occupied by several signals which are not found at forward scattering angles and are expected to come from multiple scattering from deeper layers. This is fully reproduced by calculations and can be interpreted in terms of interference effects. The agreement with MSC calculations demonstrates the breakdown of the simple forward scattering picture and underlines the demand for an exact treatment of the situation. In [**107**], the authors found that despite the rather large photoelectron kinetic energies of 610 (Mn2p) and 720 eV (O1s), the forward scattering picture was insufficient for the description of XPD data of MnO, which consists of the very same MnO_6 building blocks as LXMO.

The upper graph features results of MSC calculations for a LaO and a MnO_2 termination of the LMO cluster in green and red. The doped manganites are only compared to the red MnO_2 simulations. In general, the agreement between experiment and calculations for MnO_2-terminated samples is better compared to calculations for a LaO-terminated cluster. This result may be expected from previous DFT calculations [**154**], [**155**], [**156**], angle-resolved photoemission spectroscopy [**157**], [**158**], [**159**], [**160**], [**161**], [**162**] or ion scattering [**163**] because the MnO_2 layer has a significantly lower surface energy.

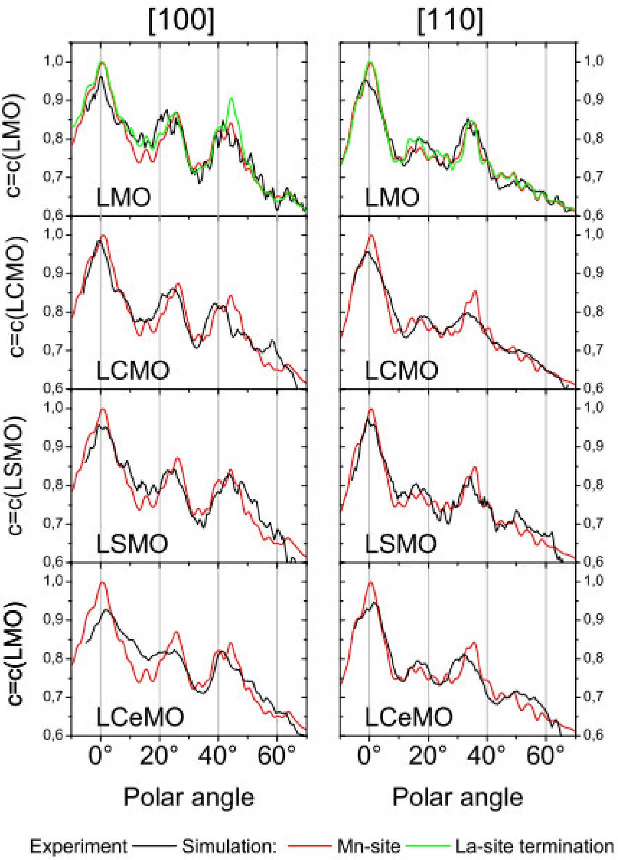

Figure 7-3: **Comparison of XPD polar scans (black lines) of O1s in the [100]-direction (left) and along the [110]-azimuth (right). The upper graph shows the diffraction pattern of LMO and results of MSC calculations for a LaO- (green) and a MnO_2-terminated cluster (red). The angular dispersion curves of LCMO, LSMO and LCeMO (from top to bottom) are compared to the latter termination only.**

Figure 7-3 shows the corresponding data for photoemission from the O1s core level of the four manganite samples. Peaks are again found at 0°, near 25° and slightly above 40° in the [100]-direction. The [110]-scans feature signals at 0°, 15° and around 35°. The absence of a sharp [101] peak at 55° in experiment and theory is worth mentioning in this context. Again, the top graph for LMO shows the two possible terminations directly compared to the experimental data, while the doped manganites below are plotted together with the red curve calculated for emission from a MnO_2-terminated cluster only. Again, it is the MnO_2-termination that fits better to the measured polar scans. We can speak in favor of a MnO_2 layer at the very surface of the films in this study.

Overall, there is only little difference between the scans taken of different films for Mn2p and O1s photoemission. All perovskite lattices seem to consist of a similar MnO_6 network which is little influenced by the chemical pressure from the dopand atoms, at least as far as XPD data is concerned. The good agreement between experiment and theory proves that the octahedral environment around Mn and the surrounding of O were successfully modeled, that they are rather similar and that both of them show features expected for cubic structures. All structures are well reproduced by MSC calculations without the need for additional changes to the bulk atom positions. It must be noted that no additional (surface) structural changes have been made to the bulk LMO cluster, i.e. relaxation, rumpling, or surface reconstructions have been neglected here. Chapter 7.3.3 will show that their effects on Mn and O polar scans are small. Only the tetragonal distortion for the pseudocubic films according to table7-1 was taken into account. Tetragonality, defined as the c/a ratio is small, however, for all samples. It amounts to no more than 2% for LCMO.

7.3.2 Results from high kinetic energy core levels of dopands (La4d, Ca2p, Sr3d)

Because the ADCs of Mn and O in the MnO_6 octahedra showed comparable results for all samples, the local environment around the other cations La, Ca, Sr and Ce was investigated. This chapter focuses on the diffraction patterns of A-site atoms with high kinetic energy photoemission lines. Higher kinetic energies of the photoelectrons typically reduce interference effects in favor of stronger intensity along internuclear axes or in the direction of close, strong scatterers. The data in figure 7-4 gives a lot of information about the doping atoms in LCeMO, LCMO and LSMO already at a first view.

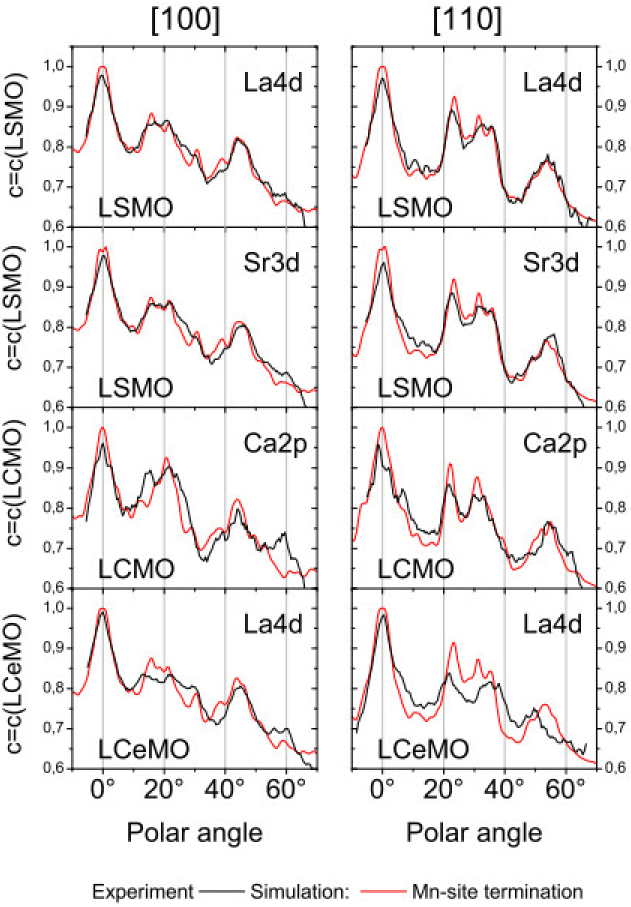

Figure 7-4: Comparison of XPD polar scans (black lines) of high kinetic energy core levels of A-site ions in LXMO in comparison to MSC calculations (red lines) in the [100]- and the [110]- direction for a MnO_2-terminated cluster.

From top to bottom the polar scans of La4d (1150 eV) and Sr3d (1120 eV) in LSMO, emission from the Ca2p level (900 eV) in LCMO and the La4d level of LCeMO are shown. Again, the left column shows results of the diffraction experiment in the [100]-direction, while the right hand side presents data along the [110] azimuth. The higher photoelectron kinetic energies compared to Mn2p / O1s at 610 / 720 eV make the forward scattering picture more applicable but it must still be used with great caution.

The first important point to make is the similarity between photoemission from the La4d (1150 eV) and the Sr3d (1120 eV) core levels in LSMO. They both show almost identical diffraction patterns from the A-sites that they occupy. The same goes for the comparison of Sr3d and Ca2p in both directions. It is intuitive to assume equal positions of the two dopands in the perovskite lattice. The [100]-direction of Mn and O was dominated by broad peaks at 0°, 22° and 42°. The dopand ADCs on the other hand feature a broad complex region between 10° and 30° and a peak at 45° with a shoulder reaching up to 60°. This shape seems to be characteristic for the twelve-fold coordinated A-site and is very well reproduced by MSC calculations. The occurence of the [101] peak at 45° is an indication for stronger forward scattering at these energies, but the medium-angle region is still formed by a multitude of different peaks.

In the [110]-direction presented in the right column of figure 7-4, peaks are found at angles of 0°, 25°, 35° and 55°, which is in rather good agreement with the [001], [113], [112] and [111] directions of a cubic structure, respectively. Finally the comparison between the two La4d scans for LSMO (top) and LCeMO (bottom) show distinct differences between these two compounds. While the calculated intensity nicely fits to the experimental data for LSMO, there is disagreement between the measurements and theoretical results for the case of Ce doping. It is safe to say, that Sr and Ca occupy the La lattice sites as expected. Furthermore, the A-site provides a cubic environment for the atoms located there. The case of Ce-doping will be discussed in more detail in the following segment. The high kinetic energy A-site data of LCeMO La4d in the bottom row of figure 7-4 displays a slightly stronger discrepancy between experiment and theory.

It must be mentioned again, that the achieved level of agreement between experiment and simulation with the intensity ratio approach is very good. The two well-known and much studied colossal magnetoresistance materials LCMO and LSMO behave similarly with regard to their structure and their transport and magnetic properties while this is a matter of discussion for LCeMO. The question whether or not LMO accepts electron doping by means of substituting La for tetravalent Cerium and whether or not a Mn^{2+} / Mn^{3+} mixed configuration results, was previously discussed in chapter 6. The structural data presented on LCeMO so far is different from the two benchmark manganites as well. To add to this controversy, the La3d and Ce3d polar scans of this compound will be more closely examined in the following section.

7.3.3 Results from low kinetic energy core levels (La3d, Ce3d)

The La3d niveau at a photoelectron kinetic energy of 420 eV was also used to record XPD patterns. Typical polar scans in the [110] direction show a very broad feature at normal emission, a weak peak at 20° and an even weaker shoulder at 35°. The [100]-direction in figure 7-5 features a broad 0° peak as well, accompanied by weak peaks at around 20° and 40°. Although it may be weak, such anisotropy is found for all samples in this study. The highly surface-sensitive nature of these low kinetic energy photoelectrons has a profound effect on the polar scans: The IMFP at $E_{kin} \approx 400$ eV is less than half as big (c.f. figure 4-7) compared to electrons with $E_{kin} \approx 1100$ eV (Sr3d in the previous segment) which means that less emitters are probed and the signal is weaker. A comparison between experimental (black line) and simulated La3d-[100] (red line) polar scans is found in figure 7-5.

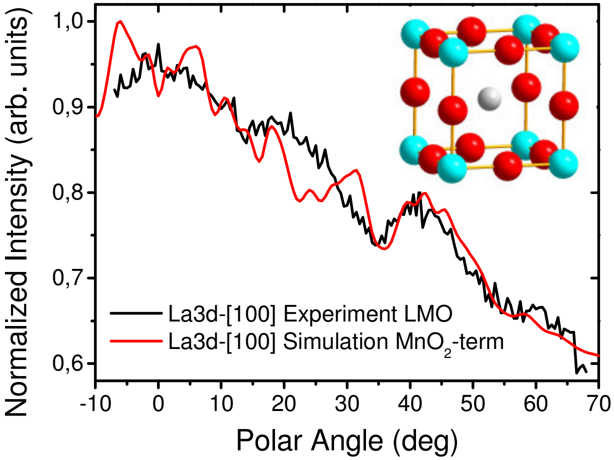

Figure 7-5: La3d polar scan of LMO in the [100]-direction (black) compared to calculated angular-dependent intensity for a MnO_2-terminated LMO cluster (red). The inset shows a sketch of the LMO unit cell with La (grey), Mn (blue) and O (red) atoms.

The agreement between experiment and theory is rather poor except for the peak at 40°. What is most striking is that the enhancement of the forward scattering direction at 0° is not found in the simulated curve (red line) but a local minimum is instead seen with two peaks at ± 7°. Such a drastic deviation should be detected by the measurement.

The reasons for this so-called volcano shape are found when looking at a sketch of the environment around a La atom (inset of fig. 7-5). For a given La emitter (grey) the normal emission direction (vertical) is surrounded by 4 oxygen (red) atoms in [100], [010] [-100] and [0-10] directions and 4 manganese (cyan) atoms in [110], [1-10], [-1-10] and [-110]. A La3d photoelectron from a deeper lying lanthanum atom is forward-scattered at the grey atom in the inset of figure 7-5 and then passes through the square of atoms above La. Here interference effects between electron waves of oxygen character near normal emission and the scattered electron wave of La itself are possible and lead to the calculated dip at 0°. The fact that this was not observed in the experimental data needs to be understood and explained.

For this purpose the effects of several changes to the bulk atom positions were studied, namely tetragonal distortion, rumpling (displacement of O atom positions relative to the ideal AO (BO_2) layer) and polar shifts (where mainly La is displaced). Neither displacing Mn nor O changes the La3d-[100] polar scan. Adding tetragonal distortion according to table 7-1 (a = b = 3.905 Å, c = 3.889 Å) does not affect the ADC either because the change amounts to no more than 0.4 % for LMO. The biggest change is possible when displacing La atoms alone along z, which is a means of compensating charges in the near surface region in this polar arrangement of alternating MnO_2^- and LaO^+ layers. Density-functional theory calculations by Evarestov et al. [**154**], [**164**] have shown that La atoms in LMO shift by up to 8 % from their ideal lattice positions in the first three unit cells near the surface. The uppermost La atom moves towards the vacuum (upwards) by about 8%, atoms in deeper layers move upward by 4% and 5% respectively. This of course has a much bigger effect than tetragonality, especially on the La3d polar scans. A mean upward shift of 5% compared to the equilibrium position for the La atom in the uppermost three layers gives the best R-factor for both polar scan directions. The volcano-shape around 7° then gives way to a regular peak shape. The agreement in the middle region becomes better as well because the peak at 20° gains intensity at the expense of the peak at 30° (unpublished data by Ch. Langheinrich, personal communication).

Finally the Ce3d core level was used for photoelectron diffraction. However, the curve in figure 7-6 does not show any diffraction pattern at all, not even the typical enhancement by forward scattering in normal emission ($\theta = 0°$) is observed.

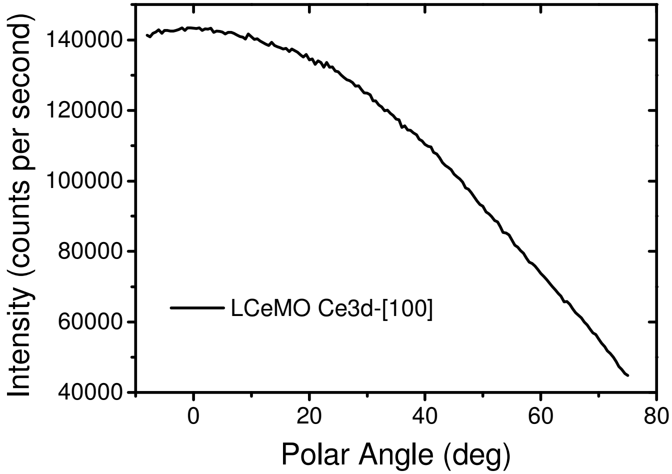

Figure 7-6: Polar scan of the Ce3d core level in the [100] direction. It must be noted that the data is presented as measured, prior to background correction and normalization.

Since XPD intensities of all elements were recorded at the same time, we can rule out technical difficulties on the basis of Mn, O and La diffraction presented in figures 7-2, 7-3 and 7-4 from the LCeMO sample. Thus, a different explanation must be found. One can, however, only speculate on the reasons for the missing diffraction.

The cation disorder induced by doping on the La site and the accompanying oxygen displacements may be quantified by the variance according to Attfield (Table 3-3). The biggest La site disorder is found when it is replaced by Ce^{4+}. The variance reaches values of $1 \cdot 10^{-2}$ in this case, which is the predicted limit for phase separation. In fact, many references [**117**], [**165**], [**125**], [**127**], [**166**], [**167**] refer to LCeMO as a multiphase mixture of A-site-deficient LCeMO and CeO_2 clusters. Alifanti [**167**] states that only 8% Cerium are soluble in LMO, which would result in $La_{0.7}Ce_{0.08}MnO_3$ and CeO_2).

Werner et al. [**62**] found evidence for nm-sized CeO_2 inclusions in the same LCeMO samples used in this work. They were not detected by XRD but are only found by means of high-resolution transmission electron microscopy (HR-TEM). Possible reasons include the low total amount and / or their small size or their amorphous nature. It can be seen in figure 7-7, that the CeO_2 segregation leads to crystalline droplets that are found at or near the surface of the film.

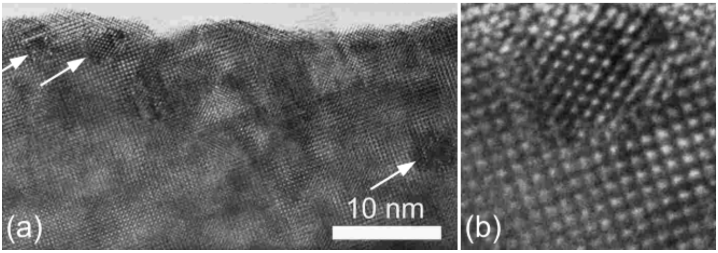

Figure 7-7 (taken from [62]: Plan-view HRTEM image of (a) a LCeMO sample with nm-sized CeO_2 inclusions and (b) a more detailed example of an inclusion (left arrow in (a)).

They represent CaF_2-like CeO_2 inclusions in a La-deficient matrix. Only if all segregates are aligned, i.e. if they are not amorphous and if they have a well-defined orientation with respect to the matrix, one could expect to find a diffraction pattern coming from them.

An additional explanation for the absence of diffraction from the Cerium core level is the photoelectron's low kinetic energy and its abovementioned high surface sensitivity. It is possible that randomly oriented CeO_2 segregations near the surface lead to the absence of scattering patterns from the Ce3d core level while photoelectrons from the other elements reach the analyzer.

A last possibility is that the Ce^{4+} ion is too small for the A-site that it is supposed to occupy and that it can consequently move inside the interstice, leading to a diffuse diffraction pattern. This idea is supported by the Shannon ionic radii in (Table 3-1) that may be used to calculate the Goldschmidt tolerance factor (Table 3-2). Of all doped manganites studied in this chapter, LCeMO has by far the lowest tolerance factor. Furthermore, while the radius of Ce^{4+} is 114 pm compared to La^{3+} with 136 pm or O^{2-} with 140 pm, its volume ($^4/_3 \pi r^3$) amounts to no more than 54% of the ideal size r_O.

7.4 Discussion

The element-specific investigation of atom positions in the doped manganites by means of x-ray photoelectron diffraction was possible and delivered several results.

It could be shown that the Mn and O positions of the father compound LaMnO3 and the doped samples $La_{0.7}Sr_{0.3}MnO_3$, $La_{0.7}Ca_{0.3}MnO_3$ and $La_{0.7}Ce_{0.3}MnO_3$ are all very similar. The MnO_6 octahedra network that determines the structure AND the properties of the manganites is robust and barely affected by chemical pressure from differently sized and differently charged A-site atoms. This explains the similar behavior with respect to transport and magnetism of the doped films. Experimental findings were strongly supported by the extraordinary agreement with theoretically calculated angular dependent intensities. Strong evidence for a MnO_2-termination of all samples was found, in agreement with literature.

Furthermore, it could be shown in direct comparison that the diffraction patterns of the dopand atoms Sr and Ca are almost identical and that their characteristic footprint from the A-site could be simulated with high accuracy as well. For this purpose it was necessary to compare diffraction from core levels with similar (and high) kinetic energy of the emitted photoelectrons.

A comparison between high and low kinetic energy photoemission data even for the same element was not useful due to the large differences between the scattering characteristics of different initial states, the different scattering amplitudes and information depths. The forward scattering picture is not sufficient to explain the experimental data of medium (Mn2p and O1s) energy core levels at 610 and 720 eV. Only high kinetic energy scans at 900 to 1100 eV display strongly pronounced peaks from scattering at nearest neighbors.

Therefore, low energy photoelectrons near 400 eV from La3d and Ce3d core levels were treated separately. One finding is that while Ca and Sr give clear diffraction patterns, angle-dependent Cerium photoemission from LCeMO does not show any anisotropy at all. From the same sample, LCeMO, a weak diffraction pattern from La3d could be recorded and the high kinetic energy La4d data shows clear features. The question remains whether the missing diffraction pattern of Ce is an intrinsic property of LCeMO or a problem of the low kinetic energy and the low IMFP of these electrons.

Together with the findings in chapter 6, discrepancies in transport and magnetic properties as well as electronic structure, the picture emerges that possibly not all Ce atoms in LCeMO are found in their octahedral interstice. Not only does this explain the missing diffraction pattern but also the differences in the high energy La4d scans with respect to, for instance, LSMO-La4d presented in figure 7-4.

For the case of La3d a theoretically predicted polar shift of La atoms towards the surface is necessary to explain the behavior of the angular distribution curve in the [100]-direction. The polar nature of the alternating layers of LaO^+ and MnO_2^- creates an uncompensated potential at the interface to the vacuum which is in part relieved by this La displacement. Only if this displacement is accounted for, is it possible to describe the La3d polar scans of LMO. The doped manganites do not experience such drastic shifts because they obviously have other ways of relieving the abovementioned charge at the interface to vacuum.

As a summary, XPD was successfully employed to study the atomic environments around all constituting atoms of LMO, LCMO, LSMO and LCeMO. Several findings were presented in this chapter that were only possible with the help of multiple scattering cluster calculations. The forward scattering picture is not sufficient to explain the shape of most of the measured curves alone, interference effects and multiple scattering have to be taken into account.

The underlying study shows the difficulties arising from the choice of the photoelectron energy. Low energy electrons give surface-sensitive information typically used to investigate the sample termination. These core levels yielded only scarce information in this experiment. Multiple scattering cluster calculations in the energy regime around 400 eV are difficult because radial matrix elements and phase shifts (scatterer properties) depend strongly on the energy and small deviations can cause big uncertainties.

Medium energy photoelectrons were found to be affected by multiple scattering effects despite energies of up to 700 eV, above the widely accepted 500 eV barrier that separates single scattering behavior from multiple scattering. Finally the high energy photoelectrons delivered clear indications for the positions of the dopand atoms but are unreliable for the study of sample termination.

In brief, the benchmark manganites LCMO and LSMO feature polar scans that are in better agreement with simulations compared to LCeMO, which is most likely a multiphase mixture. All samples appear MnO_2-terminated and polar shifts of La atoms are necessary to explain diffraction patterns of the $LaMnO_3$ sample.

8 LCMO / YBCO Magnetic structure of cuprate / manganite bilayers

8.1 Motivation

The final experimental part of this thesis deals with an interface between two oxides. It requires the experience from the study of the crystal structure, the electronic structure and the magnetic structure that was gained in the last three chapters. It also takes this knowledge to a new level, because - after the titanates and the manganites - another important class of oxides is introduced: The high-temperature superconducting (SC) cuprates and its most important member $YBa_2Cu_3O_7$ (YBCO). This chapter presents an example of the untapped potential that the oxides offer. Besides their bulk properties, resistivity ranging from insulator to superconductor, all possible sorts of magnetism, multiferroicity, catalytical activity, mechanical hardness and wear resistance only to name a few, even more fascinating phenomena were found when creating oxide heterostructures [**168**], [**169**], [**170**], [**171**], [**172**], [**173**]. The most prominent example may be the discovery of Ohtomo and Hwang [**83**] who found metallic conductivity of the interface between two wide bandgap insulators ($LaAlO_3$ and $SrTiO_3$). On the same system collective phenomena of electrons were later found, ferromagnetism and superconductivity [**84**], [**85**], and even their coexistence at this exact interface was observed [**174**], [**175**]. Hoppler [**176**] found a modulation of ferromagnetism (FM) by a superconductor in SC-FM multilayers while Chakhalian [**177**] noticed induced ferromagnetism in the superconductor in similar structures.

Ever since de Gennes [**178**] proposed to study Cooper pairs by investigating their behavior at the interface of a SC towards normal metals this method was applied to all sorts of junctions between Insulators (I), Metals (M), Ferromagnets (F) and normal (BCS theory) or high-temperature Superconductors (S). This lead to a great variety of (Josephson) junctions of M-S, F-S, I-S character as well as a lot of sandwich structures S-I-S, S-M-S, S-F-S, S-I-F-S, S-F-I-F-S… For a review the articles by Buzdin [**46**] and Bergeret [**47**] are suggested. For the case of all-oxide SC-FM interfaces, the pioneering works by two groups must be mentioned: Habermeier [**179**] and coworkers Holden [**180**], Stahn [**181**] and Soltan [**182**] as well as Santamaria and coworkers Prieto [**183**], Sefrioui [**184**] and Pena [**185**]. They studied the transport properties and the magnetic structure of bi- and multilayers of LCMO and YBCO. It must be noted that all of Habermeier´s samples were grown using pulsed laser deposition (ablation of a target by an excimer laser in an oxygen atmosphere) while all of Santamaria´s samples were grown by dc sputtering (sputtering of a target by pure oxygen ions).

At the interface Cooper pairs may enter the ferromagnet while spin-polarized electrons may diffuse into the superconductor. Following a great amount of articles focusing on transport properties across this interface, the competition between the two effects was first studied on an atomic level by means of x-ray absorption spectroscopy and x-ray magnetic circular dichroism by Chakhalian et al. [**177**]. The authors found evidence for an induced magnetic moment on interfacial copper atoms antiferromagnetically coupled to manganese spins. The same group of authors suggested an orbital reconstruction scenario at the interface to explain this behavior [**186**].

The thickness-dependence of the competition between SC and FM was thoroughly studied by a number of methods but never before by synchrotron-based x-ray spectroscopies. At first, it was the aim of this chapter to learn more about the magnetic moment induced on copper in dependence of LCMO film thickness. During the experiments at the ANKA and ELETTRA storage rings, the focus shifted because we could not reproduce all details of abovementioned investigations. The differences and results are presented and discussed on the following pages. They were in part published in [**63**] and are reproduced with kind permission of the American Physical Society (© 2010). The article contains further information on the growth of LCMO and YBCO thin films and bilayers as well as transport and magnetic measurements on these films.

8.2 Previous Results in Literature

Due to the rather complex nature of the system at hand, an additional introduction will be given here, summarizing the work that led to the experiments presented later in this chapter. The research field was very new in 2010, so only a few articles had been published at that time. For instance, no article on XMCD results on artificial all-oxide SC-FM bilayers was available at that time, which motivated our research.

[**180**] Holden et al., Physical Review B **69** (2004) 064505

- Todd Holden et al. found a reduced free-carrier response in YBCO-LCMO superlattices compared to the pure films by means of far-infrared ellipsometry. The density of states in the FM is reduced due to the proximity effect while the Cooper pairs in the SC are polarized in the direction opposite to the magnetization direction of the free electrons in the itinerant ferromagnet. A simultaneous suppression of the Curie temperature T_{Curie} in LCMO and the critical temperature T_C in YBCO results.

[**182**] Soltan et al., Physical Review B **70** (2004) 144517

- Soltan Soltan worked on bilayers instead of superlattices by means of transport measurements and SQUID magnetometry. The aim was to use the CMR halfmetal LCMO as an electrode to inject spin-polarized electrons into the superconductor and to measure the spin-diffusion length. For fixed LCMO thickness, the ferromagnetic ordering temperature T_{Curie} decreases with increasing YBCO layer thickness. Also as a function of YBCO thickness, the critical temperature T_C of the superconductor decreases with decreasing thickness. Derived from the estimated spin diffusion length of 10 nm, the authors conclude that for YBCO layers of 30 nm and less, the critical temperature is strongly influenced by polarized electrons coming from the ferromagnet.

[**181**] Stahn et al., Physical Review B **71** (2005) 140509

- Jochen Stahn was in charge of neutron reflectometry on the multilayers. He and his coworkers found a structurally forbidden Bragg peak as a signature of differences between the nuclear and the magnetic structure. Two scenarios were proposed to explain this peak: Either a magnetically dead layer in the ferromagnet or a magnetic layer in the superconductor. The second option had been proposed theoretically a few months earlier by Bergeret [**47**].

[**177**] Chakhalian et al., Nature Physics **2** (2006) 244

- To decide which of the two scenarios was correct, Jacques Chakhalian et al. performed additional XMCD measurements on the multilayers. The second goal was to gain a microscopical insight into the cuprate-manganite system which had previously been studied in a more phenomenological way. The authors found a x-ray magnetic circular dichroic signal at both the Mn L (20 times bigger) and the Cu L edges. The sign of the signal indicated an antiparallel orientation of the two magnetic moments. The temperature dependence of the two signals (both magnetizations decay simultaneously with increasing T up to T_{Curie}) made it clear that the magnetism in the SC was in fact induced by neighboring Mn moments across the SC-FM interface. The study ruled out the magnetically dead layer which was the second possible explanation for Stahn´s results. For the interaction between Cu and Mn to be antiferromagnetic, however, either Mn $3d_{x^2-y^2}$ has to be preferably occupied or Cu $3d_{3z^2-r^2}$ must be partially unoccupied according to the Goodenough Kanamori Anderson rules.

[**186**] Chakhalian et al., Science **318** (2007) 1114

- In an attempt to explain the results presented in the Nature Physics paper, further measurements were presented by Chakhalian et al. in Science. In contrast to the proposed preferential occupation of Mn $3d_{x^2-y^2}$, the absence of x-ray linear dichroism measurements at the Cu L edge hinted at a partial occupation of Cu $3d_{3z^2-r^2}$. While the first scenario is plausible as a result of strain due to the tetragonality of LCMO for example, the partial occupation of Cu $3d_{3z^2-r^2}$ is remarkable. All d orbitals in the cuprates except $d_{x^2-y^2}$ lie well below E_F, are thus fully occupied and electronically inactive. A massive orbital reconstruction is necessary to have this orbital even partially unoccupied. From XAS experiments, an electron charge transfer was proposed in the direction of the cuprate which was explained by covalent bonding between Mn and Cu via an oxygen atom across the interface. This yields molecular orbitals in which the electrons are redistributed over Mn, Cu and O, leading to roughly 0.2 holes in Cu $d_{3z^2-r^2}$.

[**187**] Yang et al., arXiv e-prints 0911.4349 (2009)

- The last article that will be summarized in this introductory part is the attempt by Ole Krogh Andersen and coworkers to simulate the results of Chakhalian´s studies. The main author Xiaoping Yang demonstrates that it is possible to reproduce the Cu XMCD by means of ab initio methods, here spin polarized DFT. As a result of hybridization between (completely filled) Cu $d_{3z^2-r^2}$ and (unoccupied, ↑) Mn $d_{3z^2-r^2}$, a tiny number of holes is created in the Cu $d_{3z^2-r^2}$ orbital. Despite their small number (in comparison to holes in Cu $d_{x^2-y^2}$) they account for appreciable dichroic signal but do not lead to the absence of linear dichroism at the Cu L edge.

At this point, epitaxial bilayers of LCMO and YBCO were grown by R. Werner from the Institute of Physics of the University of Tübingen and taken to the synchrotrons ANKA and ELETTRA for XLD and XMCD measurements of our own. Samples were investigated at home by means of SQUID and resistivity probes as well as XRD analysis. Results are presented in chapter 8.3.

8.3 External Results

Several manganite-cuprate bilayers were deposited on $SrTiO_3$ by means of PLD by R. Werner. They were compared with single layers of YBCO and LCMO to study the effect of the FM-SC interface on transport properties. Key results are presented in figure 8-1.

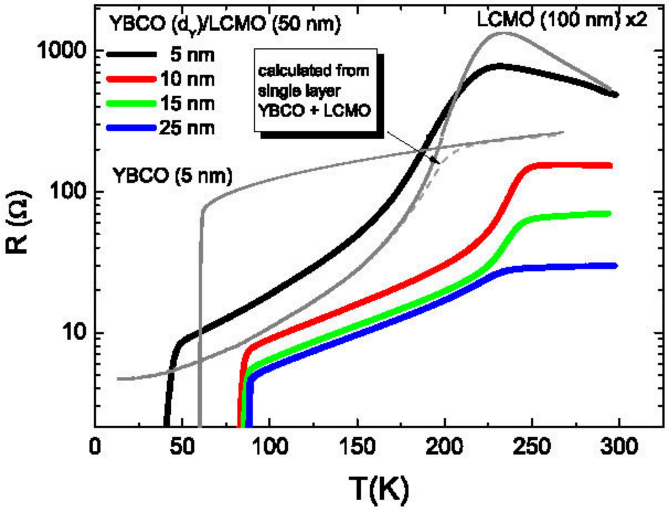

Figure 8-1 (measured by R. Werner): Resistance vs. temperature curves of YBCO / LCMO bilayers with different YBCO film thicknesses d_Y (black, red, green and blue). Theoretical R(T) curves for single cuprate / manganite layers and their superposition are drawn in grey.

YBCO thin films with a varying thickness ranging from $d_Y = 5$ to 25 nm were deposited on STO and covered with $d_L = 50$ nm LCMO films each. The resulting bilayers show the resistance vs. temperature curves in figure 8-1. The shape of the curves (black, red, green and blue) is approximated by a superposition of the grey curves and shows the metal – insulator transition of LCMO at $T_{MI} \approx T_{Curie} = 230 - 240$ K and the vanishing resistivity of the superconductor at $T_C = 85 - 90$ K (red, green and blue curves). This proves that ferromagnetism and superconductivity coexist in the samples.

A relevant suppression of the critical temperature, however, is found only for YBCO thickness below 10 nm in contrast to results presented by Soltan (T_C suppression for $d_Y < 30$ nm). More recent work by Giblin et al. [**188**] also found a suppression of T_C only for $d_Y < 9.4$ nm (8 unit cells) in sputter-deposited samples. Such a suppression is, however, found in pure YBCO layers as well and can thus not be attributed to the presence of the ferromagnet [**189**]. The reason is most likely found in the different strain states that are found in the two sample sets. While the bilayers of Soltan consisted of LCMO deposited on a STO substrate and covered by YBCO, the samples investigated here (and in [**188**]) were deposited the other way round. The YBCO film was deposited on $SrTiO_3$ and capped by LCMO. This has several advantages: For the ex-situ transport measurements the capping of YBCO is a benefit because the cuprate is much more prone to deterioration in ambient air compared to the manganite. Especially humidity leads to rapid degradation of YBCO films.

The second advantage lies in the amount and direction of strain and therefore the crystalline quality. While LCMO grows fully strained on STO for film thicknesses up to 200 nm[**153**], the superconducting film relaxes within the first few unit cells from the substrate. This gives slight compressive strain (0.3%) on LCMO instead of tensile strain (1%) in the other configuration [**190**]. The prize for these advantages is paid in the form of a higher root mean square interface roughness, 0.8 nm vs. 0.5 nm.

The observed T_C suppression as a result of spin-polarized electrons tunneling into the superconductor [**182**] could not be reproduced. Our interface configuration most likely leads to a different transparency for Cooper pairs and / or spin-polarized electrons which is known to be the key factor for the transport properties over such a junction[**46**], [**47**],[**191**]. For the purpose of examining this aspect in more detail, spectroscopic data on the interfacial Cu and Mn atoms is discussed in the following segment.

8.4 Spectroscopic results I: XMCD

The electronic structure of the samples was investigated by means of different x-ray absorption spectroscopies. Standard XAS in total electron yield and fluorescence yield detection mode was used to measure the absorption intensities of the bilayers at the Mn and Cu L edges at 640 and 930 eV, respectively. As described earlier, the polarization of the light and the magnetization of the samples can be controlled at the WERA beamline at ANKA and at APE-HE beamline at ELETTRA, where these experiments have been performed. Using linearly polarized light with the electric field vector either in-plane or out-of-plane with respect to the sample surface allows determining the linear dichroism (XLD) which is a measure of the orbital occupation in this case. Using circularly polarized light and an external magnetic field, the XMCD signal of the samples may be recorded which gives information about the magnetic structure. XMCD results of a YBCO / LCMO bilayer sample (d_Y = 20 nm, T_C = 80 K and d_L = 5.2 nm, T_{Curie} = 200 K) are shown in figure 8-2.

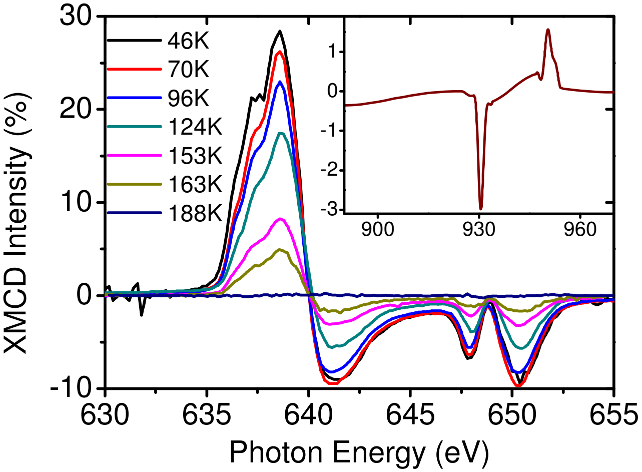

Figure 8-2: XMCD spectra at the Mn $L_{2,3}$ edge at different temperatures for a YBCO (20 nm) – LCMO (5 nm) bilayer. The inset shows the Cu L edge dichroic signal at T = 46 K, antiferromagnetically coupled to Mn magnetic moments.

While ferromagnetism at the Mn $L_{2,3}$ edges is expected for a ferromagnet and is comparable in size and shape to reports in literature (for instance [**192**], [**193**]), the more important finding is the observed dichroism at the Cu $L_{2,3}$ edges at 931 and 951 eV. The inset shows a 3% dichroic signal with opposite sign, i.e. coupled antiferromagnetically to manganese moments. Reproducing the result by Chakhalian is astonishing, finding even bigger dichroism requires an explanation. In the case of XMCD results, the bilayers are compared to multilayers (alternating layers of 10 nm YBCO and LCMO grown on $SrTiO_3$), so again we have to compare slightly different systems here. On the other hand, Chakhalian´s results were recorded by a surface sensitive technique so only the uppermost bilayer was investigated, consisting of

LCMO on top of YBCO as for the samples used in this study. Results should thus be rather comparable.

The bigger dichroic signal (more than twice as big) at the Cu L edge is therefore most likely related to a stronger coupling between Mn and Cu across the interface. A covalent bond with stronger participation of the Cu $d_{3z^2-r^2}$ leads to an increased XMCD signal [**187**]. It also leads to a wider induced nonsuperconducting layer between the manganite and the cuprate and could nicely explain the less pronounced T_C suppression found in chapter 8.3 because SC and FM are decoupled by this interfacial layer.

The appearance of a magnetic moment on copper, induced by a nearby ferromagnet can indeed be understood by a covalent bonding scenario. At the interface, Mn $d_{3z^2-r^2}$ can couple to Cu $d_{3z^2-r^2}$ via an oxygen orbital at the interface, O_{BaO} p_z, to be precise. This assumes that the interface is formed by a BaO layer of YBCO and a MnO_2 layer of LCMO, which was found by HR-TEM measurements on sputtered (Santamaria) and PLD grown (Habermeier) samples by [**194**] and [**195**], respectively. The coupling of the spin-polarized Mn orbital to the Cu orbital leads to exchange splitting on copper and the difference of the density of spin-up and spin-down Cu $d_{3z^2-r^2}$ states results in a magnetic circular dichroic signal at the Cu $L_{2,3}$ edge. The different DOS is indeed a result of the proposed redistribution of electrons over the newly formed Mn-O-Cu molecular orbital [**186**]. However, a tiny amount of holes in low-lying Cu $d_{3z^2-r^2}$ is sufficient to yield strong and robust XMCD.

Because of the energy scales of interactions, the magnetic moment on copper is likely due to spin canting in a way that is schematically displayed in figure 8-3. The exchange splitting in the FM is biggest (3 eV), the superexchange in the SC is smaller (100 meV) and the antiferromagnetic coupling between Mn and Cu was estimated to be between 20 and 40 meV [**177**].

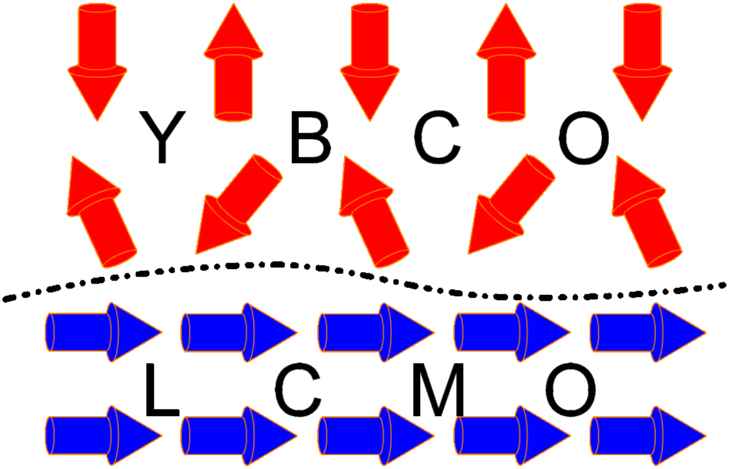

Figure 8-3: Sketch showing FM in LCMO, AFM in YBCO and induced magnetism via spin canting in YBCO at a cuprate / manganite interface.

It depicts the superexchange order in the cuprate (red arrows that point towards each other), the ferromagnetic order in the manganite (blue arrows aligned parallel) and the antiferromagnetic coupling between Mn and Cu across the interface (each blue arrow points antiparallel to the adjacent red arrow).

8.5 Spectroscopic results II: XLD on Cu

Having observed a different transport behavior of the bilayers and a stronger XMCD signal from interfacial copper, the proposed explanation by [**186**] seems unlikely to be at work for the samples in this study. From a comparison of bulk and surface sensitive linear dichroism datasets of the Cu L edge, the authors derived massive orbital reconstruction on the copper sites. Covalency establishes a bonding and an antibonding Cu-O-Mn orbital, which are filled with electrons in a way that creates holes in a very deep lying copper d orbital, namely Cu $d_{3z^2-r^2}$. Equal occupation of in-plane and out-of-plane copper orbitals was deduced from the absence of an XLD signal.

In the normal case for the cuprates, however, the out-of-plane orbital lies well below E_F and is completely filled, while the in-plane orbital in the superconducting copper planes is partially empty. Accordingly, a large linear dichroism must result and is indeed found in our samples. XLD data at the Cu L edge for different temperatures and different sampling depth is compared in figure 8-4.

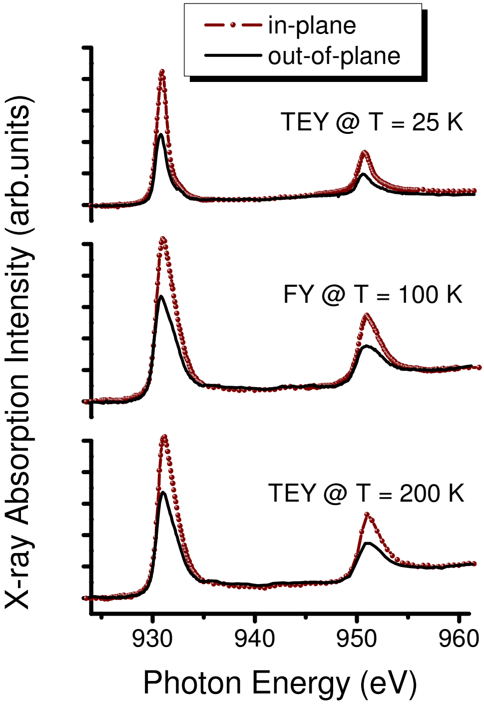

Figure 8-4: Comparison of the Cu L edge XA spectra recorded with light polarized in-plane or out-of-plane (with respect to the sample surface). Data at 25 K (TEY, top), 200 K (TEY, middle) and 100 K (FY, bottom) is basically identical.

The presence of more than 40% dichroism at T = 25 K (top) and T = 200 K (bottom) in interface sensitive TEY mode proves that the effect is not temperature dependent. There is no change in orbital occupation on copper as the manganite enters the ferromagnetic state below 200 K and the cuprate enters the superconducting state below 80 K. Furthermore, the comparison between TEY data and bulk sensitive FY mode shows the same occupation difference between in-plane and out-of-plane orbitals at the interface and in bulk. This suggests that orbital reconstruction is not a necessary prerequisite for finding an induced magnetic moment on copper atoms as proposed by [**186**].

This finding is also in excellent agreement with the work by Yang [**187**]. DFT calculations also suggest a covalent bond between Mn and Cu and consequently a redistribution of electrons over the newly created molecular orbital. The amount of holes created in this way in the out-of-plane orbitals is, however, tiny and does not amount to equal occupation of Cu $d_{3z^2-r^2}$ and Cu $d_{x^2-y^2}$. A large XLD signal is thus expected from theoretical considerations as well.

Uncertainties in the exact energy position of the edge prevented us from studying the charge transfer that accompanies the formation of the Cu-O-Mn bond. It is expected, however, that this charge transfer takes place and that hole density shifts from the SC to the FM at the interface. In other words, electrons are doped into the superconductor, as expected from a junction between two materials with different chemical potentials [**196**].

8.6 Spectroscopic results III: XLD on Mn

Preferential occupation of Mn $d_{x^2-y^2}$ was discussed as well [**177**] to explain the antiferromagnetic coupling between Mn and Cu via interfacial O_{BaO}. For this purpose the linear dichroism at the Mn L edge was obtained and is presented in figure 8-5.

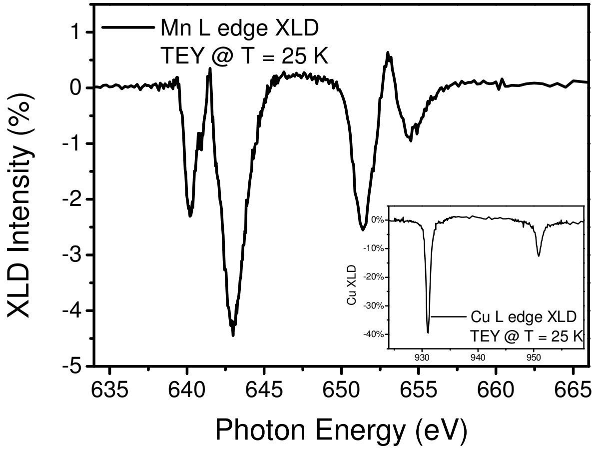

Figure 8-5: X-ray linear dichroic signal at the Mn L edge of a bilayer sample in TEY detection mode at T = 25 K and the corresponding XLD signal at the Cu L edge (inset).

Negative dichroism means that the intensity of the in-plane XAS is higher than the intensity of the out-of-plane XAS. This means that the out-of-plane $d_{3z^2-r^2}$ orbital is preferentially occupied. This is expected for the cuprates as well as for the manganites from theory [**187**] and from experiment [**197**]. It is also observed in our experiments. The size of the negative LD at the Mn L edge is in accordance with literature as well [**198**] and is a sign of enhanced magnetotransport properties along the c-axis and in-plane antiferromagnetic interactions between neighboring Mn atoms [**35**].

As a summary of the linear dichroism data, neither equal occupation of Cu $d_{3z^2-r^2}$ and Cu $d_{x^2-y^2}$ nor the preferential occupation of Mn $d_{x^2-y^2}$ could be observed experimentally. A more general summary and an outlook is given in the next segment.

8.7 Discussion

The study of bilayers comprised of two materials with antagonistic properties, ferromagnetism and superconductivity, brought about several insights. On the one hand, transport properties of these bilayers were different from previous studies; on the other hand the magnetic signature was the same. As a result of the proximity between YBCO and ferromagnetically ordered spin moments in LCMO, a magnetic moment is induced on interfacial copper atoms. The magnetic moments in the superconductor are antiferromagnetically coupled to the ones in the ferromagnet.

Among the proposed explanations for this coupling are a preferential occupation of the Mn $d_{x^2-y^2}$ orbitals and equal occupation of Cu $d_{3z^2-r^2}$ and Cu $d_{x^2-y^2}$. Neither could be confirmed in this work, most likely another mechanism for the induced copper moment is responsible which is a result of a different interfacial structure.

A direct comparison is difficult because the XLD and XMCD study in literature was performed on multilayers and the transport measurements were performed on bilayers with a different stacking sequence.

In the end, it is again the termination that may be crucial to explaining the differences between the results in literature and the findings described in chapter 8. While sputter-deposited and PLD grown samples were shown to have a BaO – MnO_2 interface [**194**], [**195**], the exact structure is still a matter of debate. Unfortunately, our bilayer was destroyed during ion milling for HR-TEM measurements.

While Varela [**194**] found LaO – MnO | BaO – CuO – Y for sputter-deposited samples, Zhang [**195**] found LaO – MnO | BaO – CuO – BaO – CuO_2 – Y for PLD samples. This is interesting because Zhang measured actual samples by Habermeier in 2009, while Chakhalian assumed that his samples had Varela's stacking sequence in 2006. Varela further notes, that counterintuitively both interfaces of the cuprate (manganite) have a BaO (MnO_2) termination [**199**], [**200**]. They mention that the sputter process at high temperatures / high pressure is more close to the thermodynamic equilibrium compared to the PLD process. Indeed, sputter-deposited superlattices are symmetric [**200**] while PLD-deposited superlattices are not [**201**]. The important difference was that in the sputtered samples the CuO chain layer at the interface was missing which was relevant for the proposed electronic structure. Zhang later measured Habermeier samples, grown by PLD, and found that this CuO chain layer was in fact present. Thus, the proposed model was based on the wrong assumptions.

Zhang closes with the warning that the interfacial stacking is very sensitive to the growth conditions which is the most likely cause for the differences between the presented findings and literature. A second group has since measured XMCD on YBCO / LCMO bilayers [**188**] but again results are at variance. A T_C suppression in YBCO due to the presence of the FM was only observed for $d_Y < 10$ nm, which is in agreement with the findings presented in this work. On the other hand, no induced copper moment was found for $d_Y > 12$ unit cells (14 nm) which contradicts our observation of canted spins in a 20 nm YBCO film in proximity to a LCMO layer. The bilayers in this latest study were grown by sputter deposition and are thus not fully comparable. More studies with well-defined interfaces (roughness, termination, etc.) are necessary to identify the actual configuration at the interface between the CMR half-metal LCMO and the high-temperature superconductor YBCO.

In the end, a stronger hybridization between Cu and Mn most probably leads to a wider induced nonsuperconducting region between FM and SC. This FM-I-SC junction has a much reduced transparency for Cooper pairs and thus explains the absence of T_C suppression for YBCO thicknesses above 10 nm [**191**], [**46**], [**47**].

As a summary of the work on the bilayers, the transport properties and the linear dichroism are different from previous studies while the induced magnetic moment on interfacial copper could be reproduced.

9 SUMMARY CONCLUSIONS AND OUTLOOK

The aim of the underlying work was the study of several interrelated aspects of the perovskite oxides. Apart from the structural aspects, it is the charge, spin and orbital degrees of freedom that make the class of perovskite manganites such an active field of research.

In this work and the related articles the effects of strain and film thickness on thin film properties, the effects of differently charged and differently sized doping atoms, the effects of surface termination, the effects of varying oxygen contents and the effects induced by an overlayer were studied. All experiments dealt with structure / effect relationships of abovementioned degrees of freedom. Three main x-ray based analysis methods were used, XPS, XAS and XPD to investigate the electronic, magnetic and crystalline structure.

The occupied (XPS) and the unoccupied densities of states of LCeMO were presented in chapter 5. The focus was on the interdependent valences of the main B-site element Mn and the A-site doping atom Ce in an ABO_3 perovskite. The nature of doping, electrons or holes, in the LCeMO system is discussed controversially. The underlying problem is in the one-sided angle of view of each single technique that has been used. In this work, transport measurements were correlated to manganese AND cerium valences obtained in surface-sensitive AND bulk-sensitive detection modes. The results give a consistent picture, showing a discrepancy between superficial and bulk valences. Also it could be shown that the proposed valences of Mn (mixed 2+/3+) and Ce (4+), i.e. electron doping, can well be created but that these samples do not show the desired properties, i.e. magnetism and a CMR effect. In turn, samples with the desired properties were found to have mixed $Mn^{2+/3+/4+}$ and $Ce^{3+/4+}$ valences and are hole-doped.

The possibility exists that Ce does not occupy the octahedral interstices as expected. Then of course doping would not have the desired effect either. Other experimental methods are however needed to study this assumption. The structure and the termination of film surfaces were thus examined by means of x-ray photoelectron diffraction. The possibility to examine only the uppermost few nanometers distinguishes this method from most other structure determination techniques.

However, only after establishing a new approach for the description of electron backgrounds in XPD angular scans was it possible to compare data from differently treated or differently doped samples to each other. This also yielded the possibility to achieve excellent agreement with theoretical data from multiple scattering cluster calculations. The high level of computational effort, the unconventional background subtraction technique and the sharp experimental diffraction patterns were combined to learn not only about the termination of the samples in dependence of preparation steps for STO single crystals but also about the occupation of octahedral interstices in LXMO thin films.

It could be shown that STO samples after crystal growth and / or after chemical etching with a NH_4F-buffered solution of hydrofluoric acid are TiO_2-terminated, while an Ar^+ ion sputtering process and subsequent recrystallization in an oxygen atmosphere leads to SrO-terminated single crystals. An additional finding was that contrary to widespread belief, chemically etched samples are not necessarily purely TiO_2-terminated, but may well contain some admixture of SrO-termination.

X-ray photoelectron diffraction results on four different lanthanum manganites, the parent compound $LaMnO_3$ and its doped derivatives $La_{0.7}Ca_{0.3}MnO_3$, $La_{0.7}Sr_{0.3}MnO_3$ and $La_{0.7}Ce_{0.3}MnO_3$, i.e. in dependence of doping atom were presented as well. The samples were found to be most likely terminated by a MnO_2 layer in agreement with literature. The building blocks, corner-sharing MnO_6 octahedra, form a rigid network that is robust with regard to the chemical pressure from the different doping atoms as far as XPD is concerned. They determine the crystalline, the magnetic and the electronic properties of the manganites and were expected to show a stronger doping dependence.

What was found instead is that the similar behavior of the doped manganites is reflected in similar crystalline structures. The octahedral interstices on the other hand showed identical diffraction patterns for Ca2p and Sr3d compared to La4d in LCMO and LSMO, respectively. These benchmark CMR manganites show clear A-site order while the scattering of Ce3d photoelectrons from within LCeMO thin films was diffuse.

Combined with abovementioned results and the finding of nm-sized CeO_2 inclusions, this result strongly suggests that Ce does in fact not occupy the A-sites in the ABO_3 structure. This does not only explain the missing diffraction pattern but also the valences investigated in chapter 6. If cation vacancies are formed by the absence of Ce in the octahedral voids, a self-doping mechanism leads to hole- instead of electron doping. Transport and magnetic measurements are then in agreement with the valences because the generally accepted double exchange mechanism between Mn^{3+} and Mn^{4+} accounts for the observed properties.

The approach takes XPD to a level where it can possibly be used as a valuable tool for the study of octahedral tilts or rotations at the very interface towards vacuum or towards overlayers, where the samples are contacted or where they form junctions with other materials. This is a new field that only just opens up in the manganite area, the design and realization of novel materials properties by strain engineering, proximity towards other compounds or the fabrication of short-period superlattices. It would be a highly interesting experiment to compare XPD data on LXMO films grown under different strain, e.g. tensile strain imposed on thin LSMO by growth on STO compared to LSMO under compressive strain grown on LAO.

Finally, work on bilayers of ferromagnetic LCMO and superconducting YBCO was conducted in chapter 8 with a focus on the electronic and magnetic structure of the interface between these “enemies”. Interestingly, while the transport properties and the orbital occupation were found to be different, the magnetic properties were identical to previous studies. The explanation is most likely found in the different interface structure, i.e. whether or not the samples are single side terminated and whether or not the interfacial YBCO unit cell is complete. More carefully conducted studies are necessary to resolve the described discrepancies.

As a summary of this thesis, the complexity of the investigated problems was continually increased from the single crystalline STO substrate via the doped lanthanum manganite thin films to a LCMO / YBCO interface. Each stage offered interesting findings on the electronic, the magnetic or the crystalline structure of the perovskite oxides. All experimental structure / effect relationships presented in chapters 5 to 8 prove that the complex nature of this materials class presents scientists with a multitude of questions and opportunities at the same time. We are still a long way from understanding and even further away from controlling the interrelated degrees of freedom in these compounds but hopefully the underlying work can offer a small stepstone on this way.

10 LIST OF FIGURES

11 REFERENCES

1 Hüfner, S. *Photoelectron spectroscopy: Principles and applications*. Springer Berlin, 1995.

2 Egelhoff, W. F. X-Ray photoelectron and auger electron forward scattering: A new tool for surface crystallography. *Critical Reviews in Solid State and Materials Sciences*, 16, 3 (1990), 213-235.

3 Stöhr, J. *NEXAFS Spectroscopy*. Springer Verlag Berlin, 1992.

4 Stöhr, J. Exploring the microscopic origin of magnetic anisotropies with X-ray magnetic circular dichroism (XMCD) spectroscopy. *Journal of Magnetism and Magnetic Materials*, 200, 1–3 (1999), 470-497.

5 Hertz, H. Ueber einen Einfluss des ultravioletten Lichtes auf die electrische Entladung. *Annalen der Physik*, 267, 8 (1887), 983-1000.

6 Hallwachs, W. Ueber die Electrisirung von Metallplatten durch Bestrahlung mit electrischem Licht. *Annalen der Physik*, 270, 8A (1888), 731-734.

7 Einstein, A. Über einen die Erzeugung und Verwandlung des Lichtes betreffenden heuristischen Gesichtspunkt. *Annalen der Physik*, 322, 6 (1905), 132-148.

8 Siegbahn, K., Nordling, C., Fahlman, A. et al. Atomic, molecular and solid-state structure studied by means of electron spectroscopy. *Nova Acta Regiae Soc. Sci. Ups.*, 20 (1967), 1-282.

9 Chambers, S. A. Epitaxial growth and properties of thin film oxides. *Surface Science Reports*, 39, 5–6 (2000), 105-180.

10 Westphal, C. The study of the local atomic structure by means of X-ray photoelectron diffraction. *Surface Science Reports*, 50, 1–3 (2003), 1-106.

11 Woodruff, D.P. Adsorbate structure determination using photoelectron diffraction: Methods and applications. *Surface Science Reports*, 62, 1 (2007), 1-38.

12 Fadley, C.S. X-ray photoelectron spectroscopy: Progress and perspectives. *Journal of Electron Spectroscopy and Related Phenomena*, 178–179 (2010), 2-32.

13 Krause, M. O. Atomic radiative and radiationless yields for K and L shells. *Journal of Physical and Chemical Reference Data*, 8, 2 (1979), 307-327.

14 Garcia de Abajo, F. J., van Hove, M. A., and Fadley, C. S. Multiple scattering of electrons in solids and molecules: A cluster-model approach. *Phys. Rev. B*, 63 (2001), 075404.

15 Haydock, R. Convergent method for calculating the properties of many interacting electrons. *Phys. Rev. B*, 61 (2000), 7953-7964.

16 Chassé, A. Theoretical photoelectron diffraction simulations for K/Si(001)2 × 1. *Surface Science*, 269–270 (1992), 22-27.

17 Chrisey, D.B. and Hubler, G.K. *Pulsed Laser Deposition of Thin Films*. Wiley VCH, 2003.

18 Janiak, C., Meyer, H.-J., Gudat, D., and Alsfasser, R. *Riedel - Moderne Anorganische Chemie*. de Gruyter Berlin, Boston, 2012.

19 Moussa, F., Hennion, M., Rodriguez-Carvajal, J., Moudden, H., Pinsard, L., and Revcolevschi, A. Spin waves in the antiferromagnet perovskite $LaMnO_3$: A neutron-scattering study. *Phys. Rev. B*, 54 (1996), 15149-15155.

20 Jahn, H. A. and Teller, E. Stability of Polyatomic Molecules in Degenerate Electronic States. I. Orbital Degeneracy. *Proceedings of the Royal Society of*

London. Series A - Mathematical and Physical Sciences, 161, 905 (1937), 220-235.

21 Sanchez, M. C., Subias, G., Garcia, J., and Blasco, J. Cooperative Jahn-Teller Phase Transition in $LaMnO_3$ Studied by X-Ray Absorption Spectroscopy. *Phys. Rev. Lett.*, 90 (2003), 045503.

22 Wollan, E. O. and Koehler, W. C. Neutron Diffraction Study of the Magnetic Properties of the Series of Perovskite-Type Compounds La1-xCaxMnO3. *Phys. Rev.*, 100 (1955), 545-563.

23 Coey, J. M. D., Viret, M., and von Molnar, S. Mixed-valence manganites. *Advances in Physics*, 48, 2 (1999), 167-293.

24 Tokura, Y. Critical features of colossal magnetoresistive manganites. *Reports on Progress in Physics*, 69, 3 (2006), 797.

25 Jonker, G.H. and van Santen, J.H. Ferromagnetic compounds of manganese with perovskite structure. *Physica*, 16, 3 (1950), 337-349.

26 van Santen, J.H. and Jonker, G.H. Electrical conductivity of ferromagnetic compounds of manganese with perovskite structure. *Physica*, 16, 7–8 (1950), 599-600.

27 Schiffer, P., Ramirez, A. P., Bao, W., and Cheong, S-W. Low Temperature Magnetoresistance and the Magnetic Phase Diagram of $La_{1-x}Ca_xMnO_3$. *Phys. Rev. Lett.*, 75 (1995), 3336-3339.

28 Tokura, Y., Tomioka, Y., Kuwahara, H., Asamitsu, A., Moritomo, Y., and Kasai, M. Origins of colossal magnetoresistance in perovskite-type manganese oxides (invited). *Journal of Applied Physics*, 79, 8 (1996), 5288-5291.

29 Millis, A. J. Lattice effects in magnetoresistive manganese perovskites. *Nature*, 392, 6672 (1998), 147-150.

30 Zener, C. Interaction between the d-Shells in the Transition Metals. II.

Ferromagnetic Compounds of Manganese with Perovskite Structure. *Phys. Rev.*, 82 (1951), 403-405.

31 Kramers, H.A. L'interaction Entre les Atomes Magnétogènes dans un Cristal Paramagnétique. *Physica*, 1, 1–6 (1934), 182-192.

32 Anderson, P. W. Antiferromagnetism. Theory of Superexchange Interaction. *Phys. Rev.*, 79 (1950), 350-356.

33 Anderson, P. W. and Hasegawa, H. Considerations on Double Exchange. *Phys. Rev.*, 100 (1955), 675-681.

34 de Gennes, P. G. Effects of Double Exchange in Magnetic Crystals. *Phys. Rev.*, 118 (1960), 141-154.

35 Goodenough, J. B. Theory of the Role of Covalence in the Perovskite-Type Manganites [La, M(II)]MnO_3. *Phys. Rev.*, 100 (1955), 564-573.

36 Kanamori, J. Superexchange interaction and symmetry properties of electron orbitals. *Journal of Physics and Chemistry of Solids*, 10, 2–3 (1959), 87-98.

37 Anderson, P. W. New Approach to the Theory of Superexchange Interactions. *Phys. Rev.*, 115 (1959), 2-13.

38 Volger, J. Further experimental investigations on some ferromagnetic oxidic compounds of manganese with perovskite structure. *Physica*, 20, 1–6 (1954), 49-66.

39 Kusters, R.M., Singleton, J., Keen, D.A., McGreevy, R., and Hayes, W. Magnetoresistance measurements on the magnetic semiconductor $Nd_{0.5}Pb_{0.5}MnO_3$. *Physica B: Condensed Matter*, 155, 1–3 (1989), 362-365.

40 von Helmolt, R., Wecker, J., Holzapfel, B., Schultz, L., and Samwer, K. Giant negative magnetoresistance in perovskitelike $La_{2/3}Ba_{1/3}MnO_x$ ferromagnetic films. *Phys. Rev. Lett.*, 71 (1993), 2331-2333.

41 Jin, S., Tiefel, T. H., McCormack, M., Fastnacht, R. A., Ramesh, R., and Chen, L. H. Thousandfold Change in Resistivity in Magnetoresistive La-Ca-Mn-O Films. *Science*, 264, 5157 (1994), 413-415.

42 Bednorz, J. G. and Müller, K. A. Possible high T_C superconductivity in the BaLaCuO system. *Zeitschrift für Physik B Condensed Matter*, 64 (1986), 189-193.

43 Zhao, G., Conder, K., Keller, H., and Muller, K. A. Giant oxygen isotope shift in the magnetoresistive perovskite $La_{1-x}Ca_xMnO_{3+y}$. *Nature*, 381, 6584 (1996), 676-678.

44 Kilian, R. and Khaliullin, G. Orbital polarons in the metal-insulator transition of manganites. *Phys. Rev. B*, 60 (1999), 13458-13469.

45 Dagotto, E., Hotta, T., and Moreo, A. Colossal magnetoresistant materials: the key role of phase separation. *Physics Reports*, 344, 1–3 (2001), 1-153.

46 Buzdin, A. I. Proximity effects in superconductor-ferromagnet heterostructures. *Rev. Mod. Phys.*, 77 (2005), 935-976.

47 Bergeret, F. S., Volkov, A. F., and Efetov, K. B. Odd triplet superconductivity and related phenomena in superconductor-ferromagnet structures. *Rev. Mod. Phys.*, 77 (2005), 1321-1373.

48 Ginzburg, V.L. Ferromagnetic Superconductors. *Journal of Experimental and Theoretical Physics*, 4 (1957), 153-161.

49 Anderson, P. W. and Suhl, H. Spin Alignment in the Superconducting State. *Phys. Rev.*, 116 (1959), 898-900.

50 Saint-James, D., Sarma, G., and Thomas, E. J. *Type II superconductivity*. Oxford, Pergamon Press, 1969.

51 Matthias, B. T., Suhl, H., and Corenzwit, E. Ferromagnetic Superconductors. *Phys. Rev. Lett.*, 1 (1958), 449-450.

52 Mandal, P. and Das, S. Transport properties of Ce-doped RMO3 (R=La, Pr, and Nd) manganites. *Phys. Rev. B*, 56 (1997), 15073-15080.

53 Goldschmidt, V. M. Die Gesetze der Krystallochemie. *Naturwissenschaften*, 14 (1926), 477-485. 10.1007/BF01507527.

54 Shannon, R. D. Revised effective ionic radii and systematic studies of interatomic distances in halides and chalcogenides. *Acta Crystallographica Section A*, 32, 5 (1976), 751-767.

55 Gross, R. and Marx, A. *Vorlesungsskript Spintronic SS2004*.

56 Hwang, H. Y., Cheong, S-W., Radaelli, P. G., Marezio, M., and Batlogg, B. Lattice Effects on the Magnetoresistance in Doped $LaMnO_3$. *Phys. Rev. Lett.*, 75 (1995), 914-917.

57 Sawatzky, G.A., Geertsma, W., and Haas, C. Magnetic interactions and covalency effects in mainly ionic compounds. *Journal of Magnetism and Magnetic Materials*, 3, 1–2 (1976), 37-45.

58 Treves, D., Eibschütz, M., and Coppens, P. Dependence of superexchange interaction on Fe^{3+}-O^{2-}-Fe^{3+} linkage angle. *Physics Letters*, 18, 3 (1965), 216-217.

59 Rodriguez-Martinez, L. M. and Attfield, J. P. Cation disorder and size effects in magnetoresistive manganese oxide perovskites. *Phys. Rev. B*, 54 (1996), R15622-R15625.

60 Rodriguez-Martinez, L. M. and Attfield, J. P. Cation disorder and the metal-insulator transition temperature in manganese oxide perovskites. *Phys. Rev. B*, 58 (1998), 2426-2429.

61 Tokura, Y. and Nagaosa, N. Orbital Physics in Transition-Metal Oxides. *Science*, 288, 5465 (2000), 462-468.

62 Werner, R., Raisch, C., Leca, V. et al. Transport, magnetic, and structural

properties of $La_{0.7}Ce_{0.3}MnO_3$ thin films: Evidence for hole-doping. *Phys. Rev. B*, 79 (2009), 054416.

63 Werner, R., Raisch, C., Ruosi, A. et al. $YBa_2Cu_3O_7$ / $La_{0.7}Ca_{0.3}MnO_3$ bilayers: Interface coupling and electric transport properties. *Phys. Rev. B*, 82 (2010), 224509.

64 Hesse, R., Chassé, T., Streubel, P., and Szargan, R. Error estimation in peak-shape analysis of XPS core-level spectra using UNIFIT 2003: how significant are the results of peak fits? *Surface and Interface Analysis*, 36, 10 (2004), 1373-1383.

65 KIT2010. *ANKA Instrumentation Handbook 2010*.

66 Panaccione, G., Vobornik, I., Fujii, J. et al. Advanced photoelectric effect experiment beamline at Elettra: A surface science laboratory coupled with Synchrotron Radiation. *Review of Scientific Instruments*, 80, 4 (2009), 043105.

67 Kawasaki, M., Takahashi, K., Maeda, T. et al. Atomic Control of the $SrTiO_3$ Crystal Surface. *Science*, 266, 5190 (1994), 1540-1542.

68 Koster, G., Kropman, B. L., Rijnders, G. J. H. M., Blank, D. H. A., and Rogalla, H. Quasi-ideal strontium titanate crystal surfaces through formation of strontium hydroxide. *Applied Physics Letters*, 73, 20 (1998), 2920-2922.

69 Bickel, N., Schmidt, G., Heinz, K., and Müller, K. Ferroelectric relaxation of the $SrTiO_3$(100) surface. *Phys. Rev. Lett.*, 62 (1989), 2009-2011.

70 Yoshimoto, M., Ohkubo, H., Kanda, N., and Koinuma, H. Two-Dimensional Epitaxial Growth of $SrTiO_3$ Films on Carbon-Free Clean Surface of Nb-Doped $SrTiO_3$ Substrate by Laser Molecular Beam Epitaxy. *Japanese Journal of Applied Physics*, 31, Part 1, No. 11 (1992), 3664-3666.

71 Berlich, A., Strauss, H., Langheinrich, C., Chassé, A., and Morgner, H. Surface termination of $BaTiO_3$ (001) single crystals: A combined electron spectroscopic and theoretical study. *Surface Science*, 605, 1–2 (2011), 158-165.

72 Beyreuther, E., Grafström, S., Eng, L. M., Thiele, C., and Dörr, K. XPS investigation of Mn valence in lanthanum manganite thin films under variation of oxygen content. *Phys. Rev. B*, 73 (2006), 155425.

73 Hüfner, S., Osterwalder, J., Greber, T., and Schlapbach, L. Interpretation of substrate photoelectron diffraction. *Phys. Rev. B*, 42 (1990), 7350-7357.

74 Raisch, C., Chassé, A., Langheinrich, C., and Chassé, T. Preparation and investigation of the A-site and B-site terminated $SrTiO_3$(001) surface: A combined experimental and theoretical x-ray photoelectron diffraction study. *Applied Physics Letters*, 112, 7 (2012), 141101.

75 Potapov, P.L and Schryvers, D. Measuring the absolute position of EELS ionisation edges in a TEM. *Ultramicroscopy*, 99, 1 (2004), 73-85.

76 Thole, B. T., Carra, P., Sette, F., and van der Laan, G. X-ray circular dichroism as a probe of orbital magnetization. *Phys. Rev. Lett.*, 68 (1992), 1943-1946.

77 Carra, P., Thole, B. T., Altarelli, M., and Wang, X. X-ray circular dichroism and local magnetic fields. *Phys. Rev. Lett.*, 70 (1993), 694-697.

78 Chen, C. T., Idzerda, Y. U., Lin, H.-J. et al. Experimental Confirmation of the X-Ray Magnetic Circular Dichroism Sum Rules for Iron and Cobalt. *Phys. Rev. Lett.*, 75 (1995), 152-155.

79 Scherz, A., Wende, H., Baberschke, K., Minar, J., Benea, D., and Ebert, H. Relation between $L_{2,3}$ XMCD and the magnetic ground-state properties for the early 3d element V. *Phys. Rev. B*, 66 (2002), 184401.

80 Ledbetter, H., Lei, M., and Kim, S. Elastic constants, debye temperatures, and electron-phonon parameters of superconducting cuprates and related oxides. *Phase Transitions*, 23, 1 (1990), 61-70.

81 Powell, C.J, Jablonski, A, Tilinin, I.S, Tanuma, S, and Penn, D.R. Surface sensitivity of Auger-electron spectroscopy and X-ray photoelectron spectroscopy. *Journal*

of Electron Spectroscopy and Related Phenomena, 98–99 (1999), 1-15.

82 Despont, L., Naumovic, D., Clerc, F. et al. X-ray photoelectron diffraction study of Cu(111): Multiple scattering investigation. *Surface Science*, 600, 2 (2006), 380-385.

83 Ohtomo, A. and Hwang, H. Y. A high-mobility electron gas at the $LaAlO_3$ / $SrTiO_3$ heterointerface. *Nature*, 427, 6973 (2004), 423-426.

84 Brinkman, A., Huijben, M., van Zalk, M. et al. Magnetic effects at the interface between non-magnetic oxides. *Nat Mater*, 6, 7 (2007), 493-496.

85 Reyren, N., Thiel, S., Caviglia, A. D. et al. Superconducting Interfaces Between Insulating Oxides. *Science*, 317, 5842 (2007), 1196-1199.

86 Huijbregtse, J.M, Rector, J.H, and Dam, B. Effect of the two SrTiO3 substrate terminations on the nucleation and growth of $YBa_2Cu_3O_7$ thin films. *Physica C: Superconductivity*, 351, 3 (2001), 183-199.

87 Matijasevic, V. C., Ilge, B., Stäuble-Pümpin, B., Rietveld, G., Tuinstra, F., and Mooij, J. E. Nucleation of a Complex Oxide during Epitaxial Film Growth: $SmBa_2Cu_3O_y$ on $SrTiO_3$. *Phys. Rev. Lett.*, 76 (1996), 4765-4768.

88 Haage, T., Zegenhagen, J., Habermeier, H.-U., and Cardona, M. Nucleation Mechanism of $YBa_2Cu_3O_{7-d}$ on $SrTiO_3$(001). *Phys. Rev. Lett.*, 80 (1998), 4225-4228.

89 Bals, S., Rijnders, G., Blank, D.H.A., and van Tendeloo, G. TEM of ultra-thin $DyBa_2Cu_3O_{7-x}$ films deposited on TiO_2 terminated $SrTiO_3$. *Physica C: Superconductivity*, 355, 3–4 (2001), 225-230.

90 Rijnders, G., Curas, S., Huijben, M., Blank, D. H. A., and Rogalla, H. Influence of substrate--film interface engineering on the superconducting properties of $YBa_2Cu_3O_{7-d}$. *Applied Physics Letters*, 84, 7 (2004), 1150-1152.

91 Vonk, V., Driessen, K. J. I., Huijben, M. et al. Initial Structure and Growth Dynamics of $YBa_2Cu_3O_{7-d}$ during Pulsed Laser Deposition. *Phys. Rev. Lett.*, 99 (2007), 196106.

92 Huijben, M., Koster, G., Blank, D. H.A., and Rijnders, G. Interface engineering and strain in $YBa_2Cu_3O_7$ thin films. *Phase Transitions*, 81, 7-8 (2008), 703-716.

93 Kawasaki, M., Ohtomo, A., Arakane, T., Takahashi, K., Yoshimoto, M., and Koinuma, H. Atomic control of $SrTiO_3$ surface for perfect epitaxy of perovskite oxides. *Applied Surface Science*, 107 (1996), 102-106.

94 Chambers, S.A., Droubay, T.C., Capan, C., and Sun, G.Y. Unintentional F doping of $SrTiO_3$(001) etched in HF acid-structure and electronic properties. *Surface Science*, 606, 3–4 (2012), 554-558.

95 Henrich, V. E. and Cox, P. A. *The Surface Science of Metal Oxides*. Cambridge University Press, 1996.

96 Gandy, H. W. Optical Transmission of Heat-Treated Strontium Titanate. *Phys. Rev.*, 113 (1959), 795-800.

97 Frederikse, H. P. R. and Hosler, W. R. Hall Mobility in $SrTiO_3$. *Phys. Rev.*, 161 (1967), 822-827.

98 Perez-Casero, R., Perriere, J., Gutierrez-Llorente, A., Defourneau, D., Millon, E., Seiler, W., and Soriano, L. Thin films of oxygen-deficient perovskite phases by pulsed-laser ablation of strontium titanate. *Phys. Rev. B*, 75 (2007), 165317.

99 Herman, G.S., Gao, Y., Tran, T.T., and Osterwalder, J. X-ray photoelectron diffraction study of an anatase thin film: TiO_2(001). *Surface Science*, 447, 1–3 (2000), 201-211.

100 Despont, L., Koitzsch, C., Clerc, F. et al. Direct evidence for ferroelectric polar distortion in ultrathin lead titanate perovskite films. *Phys. Rev. B*, 73 (2006), 094110.

101 Despont, L., Lichtensteiger, C., Clerc, F. et al. X-ray photoelectron diffraction study of ultrathin $PbTiO_3$ films. *The European Physical Journal B - Condensed Matter and Complex Systems*, 49 (2006), 141-146. 10.1140/epjb/e2006-00050-0.

102 Zhan, R. R., Vesselli, E., Baraldi, A., Lizzit, S., and Comelli, G. The Rh oxide ultrathin film on Rh(100): An x-ray photoelectron diffraction study. *The Journal of Chemical Physics*, 133, 21 (2010), 214701.

103 Tejeda, A., Wimmer, E., Soukiassian, P., Dunham, D., Rotenberg, E., Denlinger, J. D., and Michel, E. G. Atomic structure determination of the 3C-SiC(001) c(4x2) surface reconstruction: Experiment and theory. *Phys. Rev. B*, 75 (2007), 195315.

104 Poon, H. C. and Tong, S. Y. Focusing and diffraction effects in angle-resolved x-ray photoelectron spectroscopy. *Phys. Rev. B*, 30 (1984), 6211-6213.

105 Chassé, A. and Rennert, P. Determination of Absorbate Geometries from Angle-Resolved X-Ray Photoelectron Spectra. Nitrogen on Fe(111). *physica status solidi (b)*, 138, 1 (1986), 53-64.

106 Chassé, A., Niebergall, L., Rennert, P., Uhlig, I., and Chassé, T. Breakdown of the forward scattering model in MgO(001). *Surface Review and Letters*, 6 (1999), 1207.

107 Chassé, A., Langheinrich, C., Nagel, M., and Chassé, T. Photoelectron diffraction studies of Ag(001), MnO(001) and epitaxial MnO films. *Surface Science*, 605, 3–4 (2011), 272-281.

108 Holloway, P. H. and Nelson, G. C. Preferential sputtering of Ta_2O_5 by argon ions. *Journal of Vacuum Science and Technology*, 16, 2 (1979), 793-796.

109 Koster, G., Rijnders, G., Blank, D. H.A., and Rogalla, H. Surface morphology determined by (001) single-crystal $SrTiO_3$ termination. *Physica C: Superconductivity*, 339, 4 (2000), 215-230.

110 Ohnishi, T., Shibuya, K., Lippmaa, M., Kobayashi, D., Kumigashira, H., Oshima, M.,

and Koinuma, H. Preparation of thermally stable TiO_2-terminated $SrTiO_3$(100) substrate surfaces. *Applied Physics Letters*, 85, 2 (2004), 272-274.

111 Nishimura, T, Ikeda, A, Namba, H, Morishita, T, and Kido, Y. Structure change of TiO2-terminated $SrTiO_3$(001) surfaces by annealing in O_2 atmosphere and ultrahigh vacuum. *Surface Science*, 421, 3 (1999), 273-278.

112 Fragneto, A., De Luca, G. M., Di Capua, R. et al. Ti- and Sr-rich surfaces of $SrTiO_3$ studied by grazing incidence x-ray diffraction. *Applied Physics Letters*, 91, 10 (2007), 101910.

113 Kido, Y, Nishimura, T, Hoshino, Y, and Namba, H. Surface structures of $SrTiO_3$ and Ni/$SrTiO_3$ studied by medium-energy ion scattering and SR-photoelectron spectroscopy. *Nuclear Instruments and Methods in Physics Research Section B: Beam Interactions with Materials and Atoms*, 161–163 (2000), 371-376.

114 Biswas, A., Rossen, P. B., Yang, C.-H. et al. Universal Ti-rich termination of atomically flat $SrTiO_3$ (001), (110), and (111) surfaces. *Applied Physics Letters*, 98, 5 (2011), 051904.

115 Pancotti, A., Barrett, N., Zagonel, L. F., and Vanacore, G. M. Multiple scattering x-ray photoelectron diffraction study of the $SrTiO_3$(100) surface. *Journal of Applied Physics*, 106, 3 (2009), 034104.

116 Khomskii, D.I. and Sawatzky, G.A. Interplay between spin, charge and orbital degrees of freedom in magnetic oxides. *Solid State Communications*, 102, 2–3 (1997), 87-99.

117 Ganguly, R., Gopalakrishnan, I. K., and Yakhmi, J. V. Does the $LaMnO_3$ phase accept Ce-doping? *Journal of Physics: Condensed Matter*, 12, 47 (2000), L719.

118 Mitra, C., Raychaudhuri, P., John, J., Dhar, S. K., Nigam, A. K., and Pinto, R. Growth of epitaxial and polycrystalline thin films of the electron doped system $La_{0.7}Ce_{0.3}MnO_3$ through pulsed laser deposition. *Journal of Applied Physics*, 89, 1 (2001), 524-530.

119 Raychaudhuri, P., Mitra, C., Mann, P. D. A., and Wirth, S. Phase diagram and Hall effect of the electron doped manganite $La_{1-x}Ce_xMnO_3$. *Journal of Applied Physics*, 93, 10 (2003), 8328-8330.

120 Mitra, C., Hu, Z., Raychaudhuri, P. et al. Direct observation of electron doping in $La_{0.7}Ce_{0.3}MnO_3$ using x-ray absorption spectroscopy. *Phys. Rev. B*, 67 (2003), 092404.

121 Mitra, C., Raychaudhuri, P., Köbernik, G., Dörr, K., Müller, K.-H., Schultz, L., and Pinto, R. p-n diode with hole- and electron-doped lanthanum manganites. *Applied Physics Letters*, 79, 15 (2001), 2408-2410.

122 Mitra, C., Raychaudhuri, P., Dörr, K., Möller, K.-H., Schultz, L., Oppeneer, P. M., and Wirth, S. Observation of Minority Spin Character of the New Electron Doped Manganite $La_{0.7}Ce_{0.3}MnO_3$ from Tunneling Magnetoresistance. *Phys. Rev. Lett.*, 90 (2003), 017202.

123 Philip, J. and Kutty, T. R. N. Effect of valence fluctuations in A sites on the transport properties of LRMO (R = Ce, Pr). *Journal of Physics: Condensed Matter*, 11, 43 (1999), 8537.

124 Zhao, Y.G, Srivastava, R.C, Fournier, P et al. Transport and magnetic properties of $La_{0.8}Ce_{0.2}MnO_3$ thin films grown by pulsed laser deposition. *Journal of Magnetism and Magnetic Materials*, 220, 2–3 (2000), 161-166.

125 Yanagida, T., Kanki, T., Vilquin, B., Tanaka, H., and Kawai, T. Metal-insulator transition and ferromagnetism phenomena in $La_{0.7}Ce_{0.3}MnO_3$ thin films: Formation of Ce-rich nanoclusters. *Phys. Rev. B*, 70 (2004), 184437.

126 Chang, W. J., Tsai, J. Y., Jeng, H.-T. et al. Electronic structure and transport properties of $La_{0.7}Ce_{0.3}MnO_3$. *Phys. Rev. B*, 72 (2005), 132410.

127 Wang, D. J., Sun, J. R., Zhang, S. Y., Liu, G. J., Shen, B. G., Tian, H. F., and Li, J. Q. Hall effect in $La_{0.7}Ce_{0.3}MnO_{3+d}$ films with variable oxygen content. *Phys. Rev. B*, 73 (2006), 144403.

128 Fierro, J.L.G., Tascon, J.M.D., and Tejuca, L.G. Physicochemical properties of $LaMnO_3$: Reducibility and kinetics of O_2 adsorption. *Journal of Catalysis*, 89, 2 (1984), 209-216.

129 Tejuca, L. G., Fierro, J. L. G., and Tascon, J. M. D. Structure and Reactivity of Perovskite-Type Oxides (1989), 237-328.

130 Parmigiani, F. and Sangaletti, L. Fine structures in the X-ray photoemission spectra of MnO, FeO, CoO, and NiO single crystals. *Journal of Electron Spectroscopy and Related Phenomena*, 98–99, 0 (1999), 287-302.

131 Kotani, A., Jo, T., and Parlebas, J.C. Many-body effects in core-level spectroscopy of rare-earth compounds. *Advances in Physics*, 37, 1 (1988), 37-85.

132 Pfau, A. and Schierbaum, K.D. The electronic structure of stoichiometric and reduced CeO_2 surfaces: an XPS, UPS and HREELS study. *Surface Science*, 321, 1–2 (1994), 71-80.

133 Yates, K. and West, R. H. Monochromatized Ag L_α X-rays as a source for higher energy XPS. *Surface and Interface Analysis*, 5, 4 (1983), 133-138.

134 specs2008. *High Energy XPS Using a Ag L_α Source*.

135 Galakhov, V. R., Demeter, M., Bartkowski, S. et al. Mn 3s exchange splitting in mixed-valence manganites. *Phys. Rev. B*, 65 (2002), 113102.

136 Abbate, M., de Groot, F. M. F., Fuggle, J. C. et al. Controlled-valence properties of $La_{1-x}Sr_xFeO_3$ and $La_{1-x}Sr_xMnO_3$ studied by soft-x-ray absorption spectroscopy. *Phys. Rev. B*, 46 (1992), 4511-4519.

137 de Groot, F. Multiplet effects in X-ray spectroscopy. *Coordination Chemistry Reviews*, 249, 1–2 (2005), 31-63. Synchrotron Radiation in Inorganic and Bioinorganic Chemistry.

138 Nagel, M., Biswas, I., Nagel, P., Pellegrin, E., Schuppler, S., Peisert, H., and

Chassé, T. Ultrathin transition-metal oxide films: Thickness dependence of the electronic structure and local geometry in MnO. *Phys. Rev. B*, 75 (2007), 195426.

139 Merz, M., Reutler, P., Büchner, B. et al. O1s and Mn2p NEXAFS on single-layered $La_{1-x}Sr_{1+x}MnO_4$: crystal field effect versus orbital coupling mechanism. *The European Physical Journal B - Condensed Matter and Complex Systems*, 51 (2006), 315-319.

140 Gilbert, B., Frazer, B. H., Belz, A. et al. Multiple Scattering Calculations of Bonding and X-ray Absorption Spectroscopy of Manganese Oxides. *The Journal of Physical Chemistry A*, 107, 16 (2003), 2839-2847.

141 Kittel, C. *Einführung in die Festkörperphysik*. Oldenbourg Wissenschaftsverlag, 2005.

142 Piamonteze, C., Miedema, P., and de Groot, F. M. F. Accuracy of the spin sum rule in XMCD for the transition-metal L edges from manganese to copper. *Phys. Rev. B*, 80 (2009), 184410.

143 Aruta, C., Ghiringhelli, G., Bisogni, V., Braicovich, L., Brookes, N. B., Tebano, A., and Balestrino, G. Orbital occupation, atomic moments, and magnetic ordering at interfaces of manganite thin films. *Phys. Rev. B*, 80 (2009), 014431.

144 Edmonds, K. W., Farley, N. R. S., Johal, T. K., van der Laan, G., Campion, R. P., Gallagher, B. L., and Foxon, C. T. Ferromagnetic moment and antiferromagnetic coupling in (Ga,Mn)As thin films. *Phys. Rev. B*, 71 (2005), 064418.

145 Yanagida, T., Saitoh, Y., Takeda, Y., Fujimori, A., Tanaka, H., and Kawai, T. X-ray absorption magnetic circular dichroism of (La,Ce)MnO_3 thin films. *Phys. Rev. B*, 79 (2009), 132405.

146 Goering, E. X-ray magnetic circular dichroism sum rule correction for the light transition metals. *Philosophical Magazine*, 85, 25 (2005), 2895-2911.

147 Koelling, D.D., Boring, A.M., and Wood, J.H. The electronic structure of CeO_2 and

PrO_2. *Solid State Communications*, 47, 4 (1983), 227-232.

148 Murugavel, P., Lee, J. H., Yoon, Jong-Gul, Noh, T. W., Chung, J.-S., Heu, M., and Yoon, S. Origin of metal-insulator transition temperature enhancement in underdoped lanthanum manganite films. *Applied Physics Letters*, 82, 12 (2003), 1908-1910.

149 Orgiani, P., Aruta, C., Ciancio, R., Galdi, A., and Maritato, L. Enhanced transport properties in $LaxMnO_{3-d}$ thin films epitaxially grown on $SrTiO_3$ substrates: The profound impact of the oxygen content. *Applied Physics Letters*, 95, 1 (2009), 013510.

150 Koo, T. Y., Park, S. H., Lee, K.-B., and Jeong, Y. H. Anisotropic strains and magnetoresistance of $La_{0.7}Ca_{0.3}MnO_3$. *Applied Physics Letters*, 71, 7 (1997), 977-979.

151 Song, J.-H., Kim, K.K., Oh, Y.J., Jung, H.-J., Song, J.H., Choi, D.-K., and Choi, W.K. Twinned $LaAlO_3$ substrate effect on epitaxially grown La–Ca–Mn–O thin film crystalline structure. *Journal of Crystal Growth*, 223, 1–2 (2001), 129-134.

152 Orgiani, P., Petrov, A. Y., Ciancio, R., Galdi, A., Maritato, L., and Davidson, B. A. Evidence of direct correlation between out-of-plane lattice parameter and metal-insulator transition temperature in oxygen-depleted manganite thin films. *Applied Physics Letters*, 100, 4 (2012), 042404.

153 Ranno, L., Llobet, A., Tiron, R., and Favre-Nicolin, E. Strain-induced magnetic anisotropy in epitaxial manganite films. *Applied Surface Science*, 188, 1–2 (2002), 170-175.

154 Evarestov, R. A., Kotomin, E. A., Mastrikov, Yu. A., Gryaznov, D., Heifets, E., and Maier, J. Comparative density-functional LCAO and plane-wave calculations of $LaMnO_3$ surfaces. *Phys. Rev. B*, 72 (2005), 214411.

155 Piskunov, S., Heifets, E., Jacob, T., Kotomin, E. A., Ellis, D. E., and Spohr, E. Electronic structure and thermodynamic stability of $LaMnO_3$ and $La_{1-x}Sr_xMnO_3$

(001) surfaces: Ab initio calculations. *Phys. Rev. B*, 78 (2008), 121406.

156 Tang, F.L., Huang, M., Lu, W.J., and Yu, W.Y. Structural relaxation and Jahn–Teller distortion of $LaMnO_3$ surface. *Surface Science*, 603, 6 (2009), 949-954.

157 Kumigashira, H., Horiba, K., Ohguchi, H. et al. In situ photoemission characterization of terminating-layer-controlled $La_{0.6}Sr_{0.4}MnO_3$ thin films. *Applied Physics Letters*, 82, 20 (2003), 3430-3432.

158 Kumigashira, H, Horiba, K, Ohguchi, H et al. Surface electronic structures of terminating-layer-controlled $La_{0.6}Sr_{0.4}MnO_3$ thin films studied by in situ synchrotron-radiation photoemission spectroscopy. *Journal of Magnetism and Magnetic Materials*, 272–276, Part 2, 0 (2004), 1120-1121.

159 Borca, C.N, Xu, B, Komesu, T, Jeong, H.-K, Liu, M.T, Liou, S.H, and Dowben, P.A. The surface phases of the $La_{0.65}Pb_{0.35}MnO_3$ manganese perovskite surface. *Surface Science*, 512, 1–2 (2002), L346 - L352.

160 Borca, C. N., Ristoiu, Delia, Xu, Q. L., Liou, S.-H., Adenwalla, S., and Dowben, P. A. The surface terminal layer and composition of the colossal magnetoresistance perovskite: $La_{0.65}Pb_{0.35}MnO_3$. *Journal of Applied Physics*, 87, 9 (2000), 6104-6106.

161 Choi, J., Zhang, J., Liou, S.-H., Dowben, P. A., and Plummer, E. W. Surfaces of the perovskite manganites $La_{1-x}Ca_xMnO_3$. *Phys. Rev. B*, 59 (1999), 13453-13459.

162 Choi, J., Dulli, H., Liou, S.-H., Dowben, P. A., and Langell, M. A. The Influence of Surface Terminal Layer and Surface Defects on the Electronic Structure of CMR Perovskites: $La_{0.65}A_{0.35}MnO_3$ (A = Ca, Sr, Ba). *physica status solidi (b)*, 214, 1 (1999), 45-57.

163 Izumi, M., Konishi, Y., Nishihara, T., Hayashi, S., Shinohara, M., Kawasaki, M., and Tokura, Y. Atomically defined epitaxy and physical properties of strained $La_{0.6}Sr_{0.4}MnO_3$ films. *Applied Physics Letters*, 73, 17 (1998), 2497-2499.

164 Kotomin, E. A., Evarestov, R. A., Mastrikov, Yu. A., and Maier, J. DFT plane wave

calculations of the atomic and electronic structure of $LaMnO_3$ (001) surface. *Phys. Chem. Chem. Phys.*, 7 (2005), 2346-2350.

165 Joseph Joly, V.L., Joy, P.A., and Date, S.K. Studies on the effect of substitution of tetravalent ions for La^{3+} in $LaMnO_3$. *Journal of Magnetism and Magnetic Materials*, 247, 3 (2002), 316-323.

166 Stingl, C., Moshnyaga, V., Luo, Y., Damaschke, B., Samwer, K., and Seibt, M. Nanostructure of chemically phase separated La-Ce-Mn-O thin films. *Applied Physics Letters*, 91, 13 (2007), 132508.

167 Alifanti, M., Kirchnerova, J., and Delmon, B. Effect of substitution by cerium on the activity of $LaMnO_3$ perovskite in methane combustion. *Applied Catalysis A: General*, 245, 2 (2003), 231-244.

168 Chakhalian, J., Millis, A. J., and Rondinelli, J. Whither the oxide interface. *Nat Mater*, 11, 2 (2012), 92-94.

169 Hwang, H. Y., Iwasa, Y., Kawasaki, M., Keimer, B., Nagaosa, N., and Tokura, Y. Emergent phenomena at oxide interfaces. *Nat Mater*, 11, 2 (2012), 103-113.

170 Millis, A. J. Oxide interfaces: Moment of magnetism. *Nat Phys*, 7, 10 (2011), 749-750.

171 Cheong, S.-W. Transition metal oxides: The exciting world of orbitals. *Nat Mater*, 6, 12 (2007), 927-928.

172 Santamaria, J. Complex oxides: Interfaces on stage. *Nat Phys*, 2, 4 (2006), 229-230.

173 Takagai, H. Complex oxides: A tale of two enemies. *Nat Mater*, 8, 4 (2009), 251-252.

174 Bert, J. A., Kalisky, B., Bell, C., Kim, M., Hikita, Y., Hwang, H. Y., and Moler, K. A. Direct imaging of the coexistence of ferromagnetism and superconductivity at

the $LaAlO_3/SrTiO_3$ interface. *Nat Phys*, 7, 10 (2011), 767-771.

175 Li, Lu, Richter, C., Mannhart, J., and Ashoori, R. C. Coexistence of magnetic order and two-dimensional superconductivity at $LaAlO_3/SrTiO_3$ interfaces. *Nat Phys*, 7, 10 (2011), 762-766.

176 Hoppler, J., Stahn, J., Niedermayer, C. et al. Giant superconductivity-induced modulation of the ferromagnetic magnetization in a cuprate-manganite superlattice. *Nat Mater*, 8, 4 (2009), 315-319.

177 Chakhalian, J., Freeland, J. W., Srajer, G. et al. Magnetism at the interface between ferromagnetic and superconducting oxides. *Nat Phys*, 2, 4 (2006), 244-248.

178 de Gennes, P.G. and Guyon, E. Superconductivity in “normal” metals. *Physics Letters*, 3, 4 (1963), 168-169.

179 Habermeier, H.-U., Cristiani, G., Kremer, R.K., Lebedev, O., and van Tendeloo, G. Cuprate/manganite superlattices: A model system for a bulk ferromagnetic superconductor. *Physica C: Superconductivity*, 364–365 (2001), 298-304.

180 Holden, T., Habermeier, H.-U., Cristiani, G. et al. Proximity induced metal-insulator transition in$YBa_2Cu_3O_7$ / $La_{2/3}Ca_{1/3}MnO_3$ superlattices. *Phys. Rev. B*, 69 (2004), 064505.

181 Stahn, J., Chakhalian, J., Niedermayer, C. et al. Magnetic proximity effect in perovskite superconductor / ferromagnet multilayers. *Phys. Rev. B*, 71 (2005), 140509.

182 Soltan, S., Albrecht, J., and Habermeier, H.-U. Ferromagnetic/superconducting bilayer structure: A model system for spin diffusion length estimation. *Phys. Rev. B*, 70 (2004), 144517.

183 Prieto, P., Vivas, P., Campillo, G. et al. Magnetism and superconductivity in $La_{0.7}Ca_{0.3}MnO_3$ / $YBa_2Cu_3O_{7-d}$ superlattices. *Journal of Applied Physics*, 89, 12

(2001), 8026-8029.

184 Sefrioui, Z., Arias, D., Pena, V. et al. Ferromagnetic/superconducting proximity effect in $La_{0.7}Ca_{0.3}MnO_3$ / $YBa_2Cu_3O_{7-d}$ superlattices. *Phys. Rev. B*, 67 (2003), 214511.

185 Pena, V., Sefrioui, Z., Arias, D. et al. Coupling of superconductors through a half-metallic ferromagnet: Evidence for a long-range proximity effect. *Phys. Rev. B*, 69 (2004), 224502.

186 Chakhalian, J., Freeland, J. W., Habermeier, H.-U., Cristiani, G., Khaliullin, G., van Veenendaal, M., and Keimer, B. Orbital Reconstruction and Covalent Bonding at an Oxide Interface. *Science*, 318, 5853 (2007), 1114-1117.

187 Yang, X., Varesko, A. N., Antonov, V. N., and Andersen, O. K. Electronic structure and x-ray magnetic circular dichroism of $YBa_2Cu_3O_7$ / $LaMnO_3$ superlattices from first-principles calculations. *ArXiv e-prints* (2009).

188 Giblin, S. R., Taylor, J. W., Duffy, J. A. et al. Measurement of Magnetic Exchange in Ferromagnet-Superconductor $La_{2/3}Ca_{1/3}MnO_3$ / $YBa_2Cu_3O_7$ Bilayers. *Phys. Rev. Lett.*, 109 (2012), 137005.

189 Triscone, J.-M., Fischer, O., Brunner, O., Antognazza, L., Kent, A. D., and Karkut, M. G. $YBa_2Cu_3O_7$ / $PrBa_2Cu_3O_7$ superlattices: Properties of Ultrathin superconducting layers separated by insulating layers. *Phys. Rev. Lett.*, 64 (1990), 804-807.

190 Yang, Z. Q., Hendrikx, R., Aarts, J., Qin, Y., and Zandbergen, H. W. Strain release of (La,Ca)MnO_3 thin films by $YBa_2Cu_3O_{7-d}$. *Phys. Rev. B*, 67 (2003), 024408.

191 Aarts, J., Geers, J. M. E., Brück, E., Golubov, A. A., and Coehoorn, R. Interface transparency of superconductor/ferromagnetic multilayers. *Phys. Rev. B*, 56 (1997), 2779-2787.

192 Pellegrin, E, Tjeng, L.H, de Groot, F.M.F, Hesper, R, Sawatzky, G.A, Moritomo, Y,

and Tokura, Y. Soft X-ray magnetic circular dichroism study of the colossal magnetoresistance compound $La_{1-x}Sr_xMnO_3$. *Journal of Electron Spectroscopy and Related Phenomena*, 86, 1–3 (1997), 115-118.

193 Richter, M.C., Padova, P. De, Quaresima, C. et al. Resonant photoemission and XMCD on Mn-based systems. *Journal of Alloys and Compounds*, 362, 1–2 (2004), 41-47.

194 Varela, M., Lupini, A. R., Pennycook, S. J., Sefrioui, Z., and Santamaria, J. Nanoscale analysis of $YBa_2Cu_3O_{7-x}$ / $La_{0.67}Ca_{0.33}MnO_3$ interfaces. *Solid-State Electronics*, 47, 12 (2003), 2245-2248.

195 Zhang, Z. L., Kaiser, U., Soltan, S., Habermeier, H.-U., and Keimer, B. Magnetic properties and atomic structure of $La_{2/3}Ca_{1/3}MnO_3$ - $YBa_2Cu_3O_7$ heterointerfaces. *Applied Physics Letters*, 95, 24 (2009), 242505.

196 Yunoki, S., Moreo, A., Dagotto, E., Okamoto, S., Kancharla, S. S., and Fujimori, A. Electron doping of cuprates via interfaces with manganites. *Phys. Rev. B*, 76 (2007), 064532.

197 Tebano, A., Aruta, C., Sanna, S. et al. Evidence of Orbital Reconstruction at Interfaces in Ultrathin $La_{0.67}Sr_{0.33}MnO_3$ Films. *Phys. Rev. Lett.*, 100 (2008), 137401.

198 Tebano, A., Aruta, C., Medaglia, P. G. et al. Strain-induced phase separation in $La_{0.7}Sr_{0.3}MnO_3$ thin films. *Phys. Rev. B*, 74 (2006), 245116.

199 Tsymbal, E.Y. et al., eds. *Multifunctional Oxide Heterostructures*. Oxford University Press, 2012.

200 Visani, C., Tornos, J., Nemes, N. M. et al. Symmetrical interfacial reconstruction and magnetism in $La_{0.7}Ca_{0.3}MnO_3$ / $YBa_2Cu_3O_7$ / $La_{0.7}Ca_{0.3}MnO_3$ heterostructures. *Phys. Rev. B*, 84 (2011), 060405.

201 Satapathy, D. K., Uribe-Laverde, M. A., Marozau, I. et al. Magnetic Proximity

Effect in $YBa_2Cu_3O_7$ / $La_{2/3}Ca_{1/3}MnO_3$ and $YBa_2Cu_3O_7$ / $LaMnO_{3+d}$ Superlattices. *Phys. Rev. Lett.*, 108 (2012), 197201.

12 LIST OF ABBREVIATIONS

Φ	Work function
ϕ	Azimuthal (rotation) angle
θ	Polar (tilt) angle
λ	Wavelength, inelastic mean free path (IMFP)
χ	Anisotropy function, $(I - I_0) / I_0$
μ_l	Orbital magnetic moment
μ_s	Spin magnetic moment
Å	Angström, 10^{-10} m
ABO_3, ABX_3	Perovskites
ADC	Angular distribution curve
AFI, AI	Antiferromagnetic insulator
AFM	Atomic force microscopy, antiferromagnet(ic)
Ag L_a	Silver x-ray emission line
Al K_α	Aluminum x-ray emission line
ANKA	Angstroemquelle Karlsruhe
AO	One of two layers of the ABO3 perovskites
BO_2	One of two layers of the ABO3 perovskites
CAF	Canted antiferromagnet
CMR	Colossal magnetoresistance

CN	Coordination number
CO	Charge order
COI	Charge ordered insulator
DE	Double exchange
DFT	Density functional theory
d_L	LCMO film thickness
DOS	Density of states
d_Y	YBCO film thickness
E_F	Fermi level
E_{kin}	Kinetic energy
EELS	Electron energy loss spectroscopy
ELETTRA	Italian research center, Trieste
FM, F	Ferromagnet(ic)
FMI, FI	Ferromagnetic insulator
FMM	Ferromagnetic metal
FY	Fluorescence yield
HR-TEM	High resolution transmission electron microscopy
I	Insulator, insulating
IMFP	Inelastic mean free path
JT	Jahn-Teller (distortion / effect)
K edge	1s x-ray absorption edge
L edge	2p x-ray absorption edge

l_{max}	maximal angular moment in MSC calculations
LAO	$LaAlO_3$, lanthanum aluminate
LBMO	$La_{1-x}Ba_xMnO_3$, lanthanum barium manganite
LCMO	$La_{1-x}Ca_xMnO_3$, lanthanum calcium manganite
LCeMO	$La_{1-x}Ce_xMnO_3$, lanthanum cerium manganite
LMO	$LaMnO_3$, lanthanum manganite
LSMO	$La_{1-x}Sr_xMnO_3$, lanthanum strontium manganite
LXMO	$La_{1-y}X_yMnO_3$, doped lanthanum manganite
M	Metal(lic)
MBE	Molecular beam epitaxy
M edge	3d x-ray absorption edge
Mg K_α	Magnesium x-ray emission line
MSC	Multiple scattering cluster
NEXAFS	Near edge x-ray absorption fine structure
OO	Orbital order
PED	Photoelectron diffraction
PI	Paramagnetic insulator
PLD	Pulsed laser deposition
PM(M)	Paramagnet(ic) metal
$<r_A>$	Mean A-site ionic radius in the ABO_3 structure
R(T), ρ(T)	Temperature-dependent resistivity
R_{max}	maximal cluster size in EDAC MSC calculations

SC, S	Superconductor, superconducting
SE	Super exchange
SO	Spin order
SQUID	Superconducting quantum interference device
STO	$SrTiO_3$, strontium titanate
t	Hopping integral
T_C	Critical temperature of a superconductor
T_{Curie}	Curie temperature of a ferromagnet
T_{MI}	Metal-to-insulator transition temperature
$T_{Néel}$	Néel temperature of an antiferromagnet
TEY	Total electron yield
TMO	Transition metal oxide
TPP-2M	Tanuma-Powell-Penn formula for IMFP prediction
UHV	Ultra high vacuum
XAS	X-ray absorption spectroscopy
XLD	X-ray linear dichroism
XMCD	X-ray magnetic circular dichroism
XPD	X-ray photoelectron diffraction
XPS	X-ray photoemission spectroscopy
XRD	X-ray diffraction
YBCO	$YBa_2Cu_3O_7$, yttrium barium cuprate
Z	Atomic number

Unrefereed publications:

C. Raisch, R. Werner, P. Nagel, M. Merz, S. Schuppler, T. Chassé – Proximity effects at cuprate / manganite interfaces, *ANKA Synchrotron Radiation Facility Annual Report* 2011, S. 178.

C. Raisch, M. Glaser, R. Werner, A. Ruosi, P. Nagel, M. Merz, S. Schuppler, D. Koelle, R. Kleiner, T. Chassé – Interface coupling in $YBa_2Cu_3O_7$ / $La_{0.7}Ca_{0.3}MnO_3$ bilayers, *ANKA Synchrotron Radiation Facility Annual Report* 2010, S. 34.

H. Hintz, H. Peisert, C. Raisch, P. Nagel, M. Merz, S. Schuppler, T. Chassé – New low band gap materials for organic solar cells: Interface properties and electronic structure, *ANKA Synchrotron Radiation Facility Annual Report* 2009, S. 79.

C. Raisch, M. Nagel, H. Peisert, R. Werner, D. Koelle, R. Kleiner, T. Chassé, M. Merz, P. Nagel, S. Schuppler – Electronic structure of $La_{0.7}Ce_{0.3}MnO_3$ thin films, *ANKA Synchrotron Radiation Facility Annual Report* 2008, S. 85.

Conference contributions - talks:

C. Raisch, R. Werner, A. Ruosi, B. Davidson, M. Glaser, R. Kleiner, D. Koelle, T. Chassé - $YBa_2Cu_3O_7$ / $La_{0.7}Ca_{0.3}MnO_3$ bilayers: Interface coupling and electric transport properties, *Frühjahrstagung der DPG*, Dresden, 14.-18. März 2011.

C. Raisch, H. Peisert, T. Chassé - Thickness-dependent structural investigation of thin GaN films by Photoelectron Diffraction, *Frühjahrstagung der DPG*, Berlin, 25.-29. Februar 2008.

Conference contributions – poster presentations:

C. Raisch, Ch. Langheinrich, M. Glaser, R. Werner, D. Koelle, R. Kleiner, A. Chassé, T. Chassé – X-Ray Photoelectron Diffraction Studies of Structure and Surface Termination of $SrTiO_3$(001) Surfaces and Epitaxial $La_{0.7}X_{0.3}MnO_3$ (X=La, Sr, Ca, Ce) Films, *ICESS-12,* Saint-Malo (FRA), 16.-21. September 2012

C. Raisch, R. Werner, A. Ruosi, B. Davidson, M. Glaser, R. Kleiner, D. Koelle, T. Chassé - Interface coupling in $YBa_2Cu_3O_7$ / $La_{0.7}Ca_{0.3}MnO_3$ bilayers, *ANKA/KNMF Nutzertreffen,* Karlsruhe, 08. Oktober 2010

A. Ruosi, R. Werner, C. Raisch, B.A. Davidson, P. Nagel, M. Merz, S. Schuppler, M. Glaser, J. Fujii, A. Verna, T. Chassé, R. Kleiner, D. Koelle - Interface coupling in $YBa_2Cu_3O_7$ / $La_{0.7}Ca_{0.3}MnO_3$ bilayers: XMCD / LD study of the proximity effect, *Superconductivity and Magnetism 2010*, Paestum (ITA), 5.-11. September 2010.

R. Werner, A. Ruosi, C. Raisch, B. A. Davidson, R. Kleiner, D. Koelle - Interface effects and suppression of T_C in $YBa_2Cu_3O_7$ / $La_{0.7}Ca_{0.3}MnO_3$ bilayers, *Applied Superconductivity Conference*, Washington, D.C. (USA), 1.-6. August 2010.

M. Glaser, C. Raisch, T. Chassé - X-ray Photoelectron Diffraction of Perovskite Oxides, *Frühjahrstagung der DPG*, Regensburg, 21. – 26. März 2010

C.Raisch, R.Werner, H. Peisert, R. Kleiner, D. Koelle T. Chassé - Electronic and structural properties of $La_{0.7}Ce_{0.3}MnO_3$ thin films: Evidence for hole doping, *ANKA/KNMF Nutzertreffen*, Karlsruhe, 08. Oktober 2009

C.Raisch, R.Werner, H. Peisert, R. Kleiner, D. Koelle, T. Chassé - Surface Electronic Structure Of Perowskite Oxides, *Frühjahrstagung der DPG*, Dresden, 23.-27. März 2009.

C. Raisch, R. Werner, M. Nagel, H. Peisert, R. Kleiner, D. Koelle, T. Chassé - XAS on $La_{0.7}Ce_{0.3}MnO_3$ films: a critical view on valencies, *THIOX "Thin Films For Novel Oxide Devices" Final Meeting*, Sestri Levante (ITA), 9.-11. April 2008.

R. Werner, V. Leca, Ch. Back, C. Raisch, T. Chassé, R. Kleiner, D. Koelle, - Magnetic and transport properties of $La_{0.7}Ce_{0.3}MnO_3$ thin films grown by pulsed laser deposition, *THIOX "Thin Films For Novel Oxide Devices" Final Meeting*, Sestri Levante (ITA), 9.-11. April 2008.

C. Raisch, R. Werner, M. Nagel, H. Peisert, R. Kleiner, D. Koelle, T. Chassé - XAS on $La_{0.7}Ce_{0.3}MnO_3$ films: a critical view on valencies, *Frühjahrstagung der DPG*, Berlin, 25.-29. Februar 2008.

A. Sidorenko, C. Raisch, H. Peisert, T. Chassé - Substrate-dependent wetting layer formation during IBA-MBE growth of GaN: Impact on structure and morphology, *VUV XV. Konferenz*, Berlin, 29. Juli - 03. August 2007.

My academic teachers were:

K. Albert, T. Chassé, M.B. Casu, D. Christen, H. Eckstein, G. Gauglitz, M. Hanack, G. Häfelinger, D. Hoffmann, V. Hoffmann, W. Jäger, D. Koelle, R. Kleiner, D. Krug, N. Kuhn, E. Lindner, H.G. Mack, H.A. Mayer, M.E. Maier, H.-J. Meyer, U. Nagel, K. Nickel, H. Oberhammer, C. Ochsenfeld, D. Oelkrug, H. Pauschmann, J. Pietruschka, H. Peisert, E. Plies, H. Pommer G. Reinhardt, V. Schurig, M. Schwarz, E. Schweda, J. Strähle, U. Weimar, L. Wesemann, D. Wharam, K.-P. Zeller, T. Ziegler